CrossMark

LSST: From Science Drivers to Reference Design and Anticipated Data Products

Željko Ivezić[1,85], Steven M. Kahn[2,3], J. Anthony Tyson[4], Bob Abel[5], Emily Acosta[2], Robyn Allsman[2], David Alonso[6], Yusra AlSayyad[7], Scott F. Anderson[1], John Andrew[2], James Roger P. Angel[8], George Z. Angeli[9], Reza Ansari[10], Pierre Antilogus[11], Constanza Araujo[2], Robert Armstrong[7], Kirk T. Arndt[6], Pierre Astier[11], Éric Aubourg[12], Nicole Auza[2], Tim S. Axelrod[8], Deborah J. Bard[13], Jeff D. Barr[2], Aurelian Barrau[14], James G. Bartlett[12], Amanda E. Bauer[2], Brian J. Bauman[15], Sylvain Baumont[11,16], Ellen Bechtol[2], Keith Bechtol[2,17], Andrew C. Becker[1], Jacek Becla[13], Cristina Beldica[18], Steve Bellavia[19], Federica B. Bianco[20,21], Rahul Biswas[22], Guillaume Blanc[10,23], Jonathan Blazek[24,25], Roger D. Blandford[3], Josh S. Bloom[26], Joanne Bogart[3], Tim W. Bond[13], Michael T. Booth[2], Anders W. Borgland[13], Kirk Borne[27], James F. Bosch[7], Dominique Boutigny[28], Craig A. Brackett[13], Andrew Bradshaw[4], William Nielsen Brandt[29], Michael E. Brown[30], James S. Bullock[31], Patricia Burchat[3], David L. Burke[3], Gianpietro Cagnoli[32], Daniel Calabrese[2], Shawn Callahan[2], Alice L. Callen[13], Jeffrey L. Carlin[2], Erin L. Carlson[2], Srinivasan Chandrasekharan[33], Glenaver Charles-Emerson[2], Steve Chesley[34], Elliott C. Cheu[35], Hsin-Fang Chiang[18], James Chiang[3], Carol Chirino[2], Derek Chow[13], David R. Ciardi[36], Charles F. Claver[2], Johann Cohen-Tanugi[37], Joseph J. Cockrum[2], Rebecca Coles[24], Andrew J. Connolly[1], Kem H. Cook[38], Asantha Cooray[31], Kevin R. Covey[39], Chris Cribbs[18], Wei Cui[40], Roc Cutri[36], Philip N. Daly[41], Scott F. Daniel[1], Felipe Daruich[2], Guillaume Daubard[11], Greg Daues[18], William Dawson[15], Francisco Delgado[2], Alfred Dellapenna[19], Robert de Peyster[13], Miguel de Val-Borro[7], Seth W. Digel[13], Peter Doherty[42], Richard Dubois[13], Gregory P. Dubois-Felsmann[36], Josef Durech[43], Frossie Economou[2], Tim Eifler[8], Michael Eracleous[29], Benjamin L. Emmons[2], Angelo Fausti Neto[2], Henry Ferguson[44], Enrique Figueroa[2], Merlin Fisher-Levine[7], Warren Focke[13], Michael D. Foss[13], James Frank[19], Michael D. Freemon[18], Emmanuel Gangler[45], Eric Gawiser[46], John C. Geary[47], Perry Gee[4], Marla Geha[48], Charles J. B. Gessner[2], Robert R. Gibson[1], D. Kirk Gilmore[3], Thomas Glanzman[13], William Glick[18], Tatiana Goldina[36], Daniel A. Goldstein[26,49], Iain Goodenow[2], Melissa L. Graham[1], William J. Gressler[2], Philippe Gris[45], Leanne P. Guy[2], Augustin Guyonnet[42], Gunther Haller[13], Ron Harris[50], Patrick A. Hascall[13], Justine Haupt[19], Fabio Hernandez[51], Sven Herrmann[13], Edward Hileman[2], Joshua Hoblitt[2], John A. Hodgson[13], Craig Hogan[52], James D. Howard[2], Dajun Huang[19], Michael E. Huffer[3], Patrick Ingraham[2], Walter R. Innes[3], Suzanne H. Jacoby[2], Bhuvnesh Jain[53], Fabrice Jammes[45], M. James Jee[54,4], Tim Jenness[2], Garrett Jernigan[55], Darko Jevremović[56], Kenneth Johns[35], Anthony S. Johnson[13], Margaret W. G. Johnson[18], R. Lynne Jones[1], Claire Juramy-Gilles[11], Mario Jurić[1], Jason S. Kalirai[44], Nitya J. Kallivayalil[57], Bryce Kalmbach[1], Jeffrey P. Kantor[2], Pierre Karst[58], Mansi M. Kasliwal[59], Heather Kelly[13], Richard Kessler[52], Veronica Kinnison[2], David Kirkby[60], Lloyd Knox[4], Ivan V. Kotov[19], Victor L. Krabbendam[2], K. Simon Krughoff[2], Petr Kubánek[61], John Kuczewski[19], Shri Kulkarni[59], John Ku[13], Nadine R. Kurita[13], Craig S. Lage[4], Ron Lambert[2,62], Travis Lange[13], J. Brian Langton[13], Laurent Le Guillou[11,16], Deborah Levine[36], Ming Liang[2], Kian-Tat Lim[13], Chris J. Lintott[6], Kevin E. Long[63], Margaux Lopez[13], Paul J. Lotz[2], Robert H. Lupton[7], Nate B. Lust[7], Lauren A. MacArthur[7], Ashish Mahabal[59], Rachel Mandelbaum[64], Thomas W. Markiewicz[13], Darren S. Marsh[13], Philip J. Marshall[3], Stuart Marshall[3], Morgan May[19], Robert McKercher[2], Michelle McQueen[19], Joshua Meyers[7], Myriam Migliore[14], Michelle Miller[50], David J. Mills[2], Connor Miraval[19], Joachim Moeyens[1], Fred E. Moolekamp[7,65], David G. Monet[66], Marc Moniez[10], Serge Monkewitz[36], Christopher Montgomery[2], Christopher B. Morrison[1], Fritz Mueller[13], Gary P. Muller[2], Freddy Muñoz Arancibia[2], Douglas R. Neill[2], Scott P. Newbry[13], Jean-Yves Nief[51], Andrei Nomerotski[19], Martin Nordby[13], Paul O'Connor[19], John Oliver[42,67], Scot S. Olivier[15], Knut Olsen[50], William O'Mullane[2], Sandra Ortiz[2], Shawn Osier[13], Russell E. Owen[1], Reynald Pain[11], Paul E. Palecek[19], John K. Parejko[1], James B. Parsons[18], Nathan M. Pease[13], J. Matt Peterson[2], John R. Peterson[40], Donald L. Petravick[18], M. E. Libby Petrick[2], Cathy E. Petry[2], Francesco Pierfederici[68], Stephen Pietrowicz[18], Rob Pike[69], Philip A. Pinto[8], Raymond Plante[18], Stephen Plate[19], Joel P. Plutchak[18], Paul A. Price[7], Michael Prouza[61], Veljko Radeka[19], Jayadev Rajagopal[50], Andrew P. Rasmussen[40], Nicolas Regnault[11], Kevin A. Reil[13], David J. Reiss[1], Michael A. Reuter[2], Stephen T. Ridgway[50], Vincent J. Riot[15], Steve Ritz[70], Sean Robinson[19], William Roby[36], Aaron Roodman[13], Wayne Rosing[71], Cecille Roucelle[12], Matthew R. Rumore[19], Stefano Russo[13], Abhijit Saha[50], Benoit Sassolas[32], Terry L. Schalk[70], Pim Schellart[7,72], Rafe H. Schindler[3], Samuel Schmidt[4], Donald P. Schneider[29], Michael D. Schneider[15], William Schoening[2], German Schumacher[2,62], Megan E. Schwamb[73], Jacques Sebag[2], Brian Selvy[2], Glenn H. Sembroski[40], Lynn G. Seppala[15], Andrew Serio[2], Eduardo Serrano[2], Richard A. Shaw[44], Ian Shipsey[6], Jonathan Sick[2], Nicole Silvestri[1], Colin T. Slater[1], J. Allyn Smith[74], R. Chris Smith[62], Shahram Sobhani[75], Christine Soldahl[13], Lisa Storrie-Lombardi[36], Edward Stover[2], Michael A. Strauss[7], Rachel A. Street[71], Christopher W. Stubbs[42,67], Ian S. Sullivan[1], Donald Sweeney[2], John D. Swinbank[1,7], Alexander Szalay[76], Peter Takacs[19], Stephen A. Tether[13], Jon J. Thaler[77], John Gregg Thayer[13], Sandrine Thomas[2], Adam J. Thornton[2], Vaikunth Thukral[13], Jeffrey Tice[13], David E. Trilling[78], Max Turri[13], Richard Van Berg[13,53], Daniel Vanden Berk[79], Kurt Vetter[19], Francoise Virieux[12], Tomislav Vucina[2], William Wahl[19], Lucianne Walkowicz[80,81], Brian Walsh[19], Christopher W. Walter[82], Daniel L. Wang[13], Shin-Yawn Wang[36], Michael Warner[62], Oliver Wiecha[2], Beth Willman[2,8], Scott E. Winters[15], David Wittman[4], Sidney C. Wolff[2], W. Michael Wood-Vasey[83], Xiuqin Wu[36], Bo Xin[2], Peter Yoachim[1], and Hu Zhan[84]

[1] University of Washington, Dept. of Astronomy, Box 351580, Seattle, WA 98195, USA
[2] LSST Project Office, 950 N. Cherry Avenue, Tucson, AZ 85719, USA

[3] Kavli Institute for Particle Astrophysics and Cosmology, SLAC National Accelerator Laboratory, Stanford University, Stanford, CA 94025, USA

[4] Physics Department, University of California, One Shields Avenue, Davis, CA 95616, USA

[5] Olympic College, 1600 Chester Ave., Bremerton, WA 98337-1699, USA

[6] Department of Physics, University of Oxford, Denys Wilkinson Building, Keble Road, Oxford, OX1 3RH, UK

[7] Department of Astrophysical Sciences, Princeton University, Princeton, NJ 08544, USA

[8] Steward Observatory, The University of Arizona, 933 N. Cherry Ave., Tucson, AZ 85721, USA

[9] Giant Magellan Telescope Organization (GMTO), 465 N. Halstead Street, Suite 250, Pasadena, CA 91107, USA

[10] Laboratoire de l'Accélérateur Linéaire, CNRS/IN2P3, Université de Paris-Sud, B.P. 34, F-91898 Orsay Cedex, France

[11] Laboratoire de Physique Nucléaire et des Hautes Energies, Université Pierre et Marie Curie, Université Paris Diderot, CNRS/IN2P3, 4 place Jussieu, F-75005 Paris, France

[12] AstroParticule et Cosmologie, Université Paris Diderot, CNRS/IN2P3, CEA/lrfu, Observatoire de Paris, Sorbonne Paris Cité, 10, rue Alice Domon et Léonie Duquet, Paris Cedex 13, France

[13] SLAC National Accelerator Laboratory, 2575 Sand Hill Rd., Menlo Park, CA 94025, USA

[14] Laboratoire de Physique Subatomique et de Cosmologie, Université Grenoble-Alpes, CNRS/IN2P3, 53 av. des Martyrs, F-38026 Grenoble cedex, France

[15] Lawrence Livermore National Laboratory, 7000 East Avenue, Livermore, CA 94550, USA

[16] Sorbonne Universités, UPMC Univ Paris 06, UMR 7585, LPNHE, F-75005, Paris, France

[17] Department of Physics, University of Wisconsin-Madison, Madison, WI 53706, USA

[18] NCSA, University of Illinois at Urbana-Champaign, 1205 W. Clark St., Urbana, IL 61801, USA

[19] Brookhaven National Laboratory, Upton, NY 11973, USA

[20] Center for Urban Science & Progress, New York University, Brooklyn, NY 11021, USA

[21] Center for Cosmology & Particle Physics, New York University, NY 10012, USA

[22] Oskar Klein Centre, Department of Physics, Stockholm University, SE 106 91 Stockholm, Sweden

[23] Université Paris Diderot, Sorbonne Paris Cité, F-75013 Paris, France

[24] Center for Cosmology and Astro-Particle Physics, The Ohio State University, Columbus, OH 43210, USA

[25] Institute of Physics, Laboratory of Astrophysics, École Polytechnique Fedèrale de Lausanne (EPFL), Observatoire de Sauverny, 1290 Versoix, Switzerland

[26] Astronomy Department, University of California, 601 Campbell Hall, Berkeley, CA 94720, USA

[27] School of Physics, Astronomy and Computational Sciences, George Mason University, 4400 University Drive, Fairfax, VA 22030, USA

[28] Université Grenoble-Alpes, Université Savoie Mont Blanc, CNRS/IN2P3 Laboratoire d'Annecy-le-Vieux de Physique des Particules, 9 Chemin de Bellevue—BP 110, F-74940 Annecy-le-Vieux Cedex, France

[29] Department of Astronomy and Astrophysics, The Pennsylvania State University, 525 Davey Lab, University Park, PA 16802, USA

[30] Division of Geological and Planetary Sciences, California Institute of Technology, Pasadena, CA 91125, USA

[31] Center for Cosmology, University of California, Irvine, CA 92697, USA

[32] Laboratoire des Materiaux Avances (LMA), CNRS/IN2P3, Université de Lyon, F-69622 Villeurbanne, Lyon, France

[33] Department of Computer Science, University of Arizona, 1040 E. 4th St., Tucson, AZ 85719, USA

[34] Jet Propulsion Laboratory, California Institute of Technology, Pasadena, CA 91109, USA

[35] Department of Physics, University of Arizona, 1118 E. Fourth Street, Tucson, AZ 85721, USA

[36] IPAC, California Institute of Technology, MS 100-22, Pasadena, CA 91125, USA

[37] Laboratoire Univers et Particules de Montpellier (LUPM), Université de Montpellier, CNRS/IN2P3, Place Eugène Bataillon, F-34095 Montpellier, France

[38] Cook Astronomical Consulting, 220 Duxbury Ct., San Ramon, CA 94583, USA

[39] Western Washington University, 516 High Street, Bellingham, WA 98225, USA

[40] Department of Physics and Astronomy, Purdue University, 525 Northwestern Ave., West Lafayette, IN 47907, USA

[41] University of Arizona, Tucson, AZ 85721, USA

[42] Department of Physics, Harvard University, 17 Oxford St., Cambridge MA 02138, USA

[43] Astronomical Institute, Charles University, Praha, Czech Republic

[44] Space Telescope Science Institute, 3700 San Martin Drive, Baltimore, MD 21218, USA

[45] Université Clermont Auvergne, CNRS, Laboratoire de Physique de Clermont, F-63000 Clermont-Ferrand, France

[46] Department of Physics and Astronomy, Rutgers University, 136 Frelinghuysen Rd., Piscataway, NJ 08854, USA

[47] Smithsonian Astrophysical Observatory, 60 Garden St., Cambridge MA 02138, USA

[48] Astronomy Department, Yale University, New Haven, CT 06520, USA

[49] Lawrence Berkeley National Laboratory, 1 Cyclotron Road, Berkeley, CA 94720, USA

[50] National Optical Astronomy Observatory, 950 N. Cherry Ave., Tucson, AZ 85719, USA

[51] CNRS, CC-IN2P3, 21 avenue Pierre de Coubertin, CS70202, F-69627 Villeurbanne cedex, France

[52] Department of Astronomy and Astrophysics, University of Chicago, 5640 South Ellis Avenue, Chicago, IL 60637, USA

[53] Department of Physics & Astronomy, University of Pennsylvania, 209 South 33rd Street, Philadelphia, PA 19104-6396, USA

[54] Department of Astronomy, Yonsei University, 50 Yonsei-ro, Seoul 03722, Republic of Korea

[55] Space Sciences Lab, University of California, 7 Gauss Way, Berkeley, CA 94720-7450, USA

[56] Astronomical Observatory, Volgina 7, P.O. Box 74, 11060 Belgrade, Serbia

[57] Department of Astronomy, University of Virginia, Charlottesville, VA 22904, USA

[58] Aix Marseille Univ, CNRS/IN2P3, CPPM, Marseille, France

[59] Astronomy Department, California Institute of Technology, 1200 East California Blvd., Pasadena CA 91125, USA

[60] Department of Physics and Astronomy, University of California, 4129 Frederick Reines Hall, Irvine, CA 92697, USA

[61] Institute of Physics, Academy of Sciences of the Czech Republic, Na Slovance 2, 182 21 Praha 8, Czech Republic

[62] Cerro Tololo Inter-American Observatory, La Serena, Chile

[63] Longhorn Industries, Ellensburg, WA 98926, USA

[64] McWilliams Center for Cosmology, Department of Physics, Carnegie Mellon University, Pittsburgh, PA 15213, USA

[65] Department of Chemistry, Biochemistry, and Physics, Rider University, Lawrenceville, NJ 08648, USA

[66] US Naval Observatory Flagstaff Station, 10391 Naval Observatory Road, Flagstaff, AZ 86001, USA

[67] Department of Astronomy, Center for Astrophysics, Harvard University, 60 Garden St., Cambridge, MA 02138, USA

[68] Instituto de Radioastronomía Milimétrica, Av. Divina Pastora 7, Núcleo Central, E-18012 Granada, Spain

[69] Google Inc., 1600 Amphitheatre Parkway, Mountain View, CA 94043, USA

[70] Santa Cruz Institute for Particle Physics and Physics Department, University of California–Santa Cruz, 1156 High St., Santa Cruz, CA 95064, USA

[71] Las Cumbres Observatory, 6740 Cortona Dr., Suite 102, Santa Barbara, CA 93117, USA

[72] Department of Astrophysics/IMAPP, Radboud University Nijmegen, P.O. Box 9010, 6500 GL Nijmegen, The Netherlands

[73] Gemini Observatory, Northern Operations Center, 670 North A'ohoku Place, Hilo, HI 96720, USA

[74] Austin Peay State University, Clarksville, TN 37044, USA

[75] Belldex IT Consulting, Tucson, AZ 85742, USA

2

[76] Department of Physics and Astronomy, John Hopkins University, 3701 San Martin Drive, Baltimore, MD 21218, USA
[77] University of Illinois, Physics and Astronomy Departments, 1110 W. Green St., Urbana, IL 61801, USA
[78] Department of Physics and Astronomy, Northern Arizona University, P.O. Box 6010, Flagstaff, AZ 86011, USA
[79] Saint Vincent College, Department of Physics, 300 Fraser Purchase Road, Latrobe, PA 15650, USA
[80] Library of Congress, 101 Independence Ave. SE, Washington, DC 20540, USA
[81] The Adler Planetarium, 1300 South Lakeshore Ave., Chicago, IL 60605, USA
[82] Department of Physics, Duke University, Durham, NC 27708, USA
[83] Department of Physics and Astronomy, University of Pittsburgh, 3941 O'Hara Street, Pittsburgh, PA 15260, USA
[84] Key Laboratory of Optical Astronomy, National Astronomical Observatories, Chinese Academy of Sciences, 20A Datun Road, Chaoyang District, Beijing 100012, People's Republic of China

Abstract

We describe here the most ambitious survey currently planned in the optical, the Large Synoptic Survey Telescope (LSST). The LSST design is driven by four main science themes: probing dark energy and dark matter, taking an inventory of the solar system, exploring the transient optical sky, and mapping the Milky Way. LSST will be a large, wide-field ground-based system designed to obtain repeated images covering the sky visible from Cerro Pachón in northern Chile. The telescope will have an 8.4 m (6.5 m effective) primary mirror, a 9.6 deg^2 field of view, a 3.2-gigapixel camera, and six filters (*ugrizy*) covering the wavelength range 320–1050 nm. The project is in the construction phase and will begin regular survey operations by 2022. About 90% of the observing time will be devoted to a deep-wide-fast survey mode that will uniformly observe a 18,000 deg^2 region about 800 times (summed over all six bands) during the anticipated 10 yr of operations and will yield a co-added map to $r \sim 27.5$. These data will result in databases including about 32 trillion observations of 20 billion galaxies and a similar number of stars, and they will serve the majority of the primary science programs. The remaining 10% of the observing time will be allocated to special projects such as Very Deep and Very Fast time domain surveys, whose details are currently under discussion. We illustrate how the LSST science drivers led to these choices of system parameters, and we describe the expected data products and their characteristics.

Key words: astrometry – cosmology: observations – Galaxy: general – methods: observational – stars: general – surveys

1. Introduction

Major advances in our understanding of the universe have historically arisen from dramatic improvements in our ability to "see." We have developed progressively larger telescopes over the past century, allowing us to peer further into space, and further back in time. With the development of advanced instrumentation—imagers, spectrographs, and polarimeters—we have been able to parse radiation detected from distant sources over the full electromagnetic spectrum in increasingly subtle ways. These data have provided the detailed information needed to construct physical models of planets, stars, galaxies, quasars, and larger structures and to probe the new physics of dark matter and dark energy.

Until recently, most astronomical investigations have focused on small samples of cosmic sources or individual objects. This is because our largest telescope facilities typically had rather small fields of view, and those with large fields of view could not detect very faint sources. With all of our existing telescope facilities, we have still surveyed only a small fraction of the observable universe (except when considering the most luminous quasars).

Over the past two decades, however, advances in technology have made it possible to move beyond the traditional observational paradigm and to undertake large-scale sky surveys. As vividly demonstrated by surveys such as the Sloan Digital Sky Survey (SDSS; York et al. 2000), the Two Micron All Sky Survey (2MASS; Skrutskie et al. 2006), the *Galaxy Evolution Explorer* (*GALEX*; Martin et al. 2005), and *Gaia* (Gaia Collaboration et al. 2016) to name but a few, sensitive and accurate multicolor surveys over a large fraction of the sky enable

an extremely broad range of new scientific investigations. These projects, based on a synergy of advances in telescope construction, detectors, and, above all, information technology, have dramatically impacted nearly all fields of astronomy—and several areas of fundamental physics. In addition, the worldwide attention received by Sky in Google Earth[86] (Scranton et al. 2007), the World Wide Telescope,[87] and the hundreds of thousands of volunteers classifying galaxies in the Galaxy Zoo project (Lintott et al. 2011) and its extensions demonstrate that the impact of sky surveys extends far beyond fundamental science progress and reaches all of society.

Motivated by the evident scientific progress enabled by large sky surveys, three nationally endorsed reports by the US National Academy of Sciences (National Research Council 2001, 2003a, 2003b) concluded that a dedicated ground-based wide-field imaging telescope with an effective aperture of 6–8 m "is a high priority for planetary science, astronomy, and physics over the next decade." The Large Synoptic Survey Telescope (LSST) described here is such a system. Located on Cerro Pachón in northern Chile, the LSST will be a large, wide-field, ground-based telescope designed to obtain multiband images over a substantial fraction of the sky every few nights. The survey will yield contiguous overlapping imaging of over half the sky in six optical bands, with each sky location visited close to 1000 times over 10 yr. The 2010 report "New Worlds, New Horizons in Astronomy and Astrophysics" by the NRC Committee for a Decadal Survey of Astronomy and Astrophysics (National Research Council 2010) ranked LSST as its top priority for large ground-based projects, and in 2014 May the National Science Board approved the project

---

[85] Corresponding author.

[86] https://www.google.com/sky/
[87] http://worldwidetelescope.org/home

for construction. As of this writing, the LSST construction phase is close to the peak of activity. After initial tests with a commissioning camera and full commissioning with the main camera, the 10 yr sky survey is projected to begin in 2022.

The purpose of this paper is to provide an overall summary of the main LSST science drivers and how they led to the current system design parameters (Section 2), to describe the anticipated data products (Section 3), and to provide a few examples of the science programs that LSST will enable (Section 4). The community involvement is discussed in Section 5, and broad educational and societal impacts of the project are discussed in Section 6. Concluding remarks are presented in Section 7.

2. From Science Drivers to Reference Design

The most important characteristic that determines the speed at which a system can survey a given sky area to a given flux limit (i.e., its depth) is its étendue (or grasp), the product of its primary mirror area and the angular area of its field of view (for a given set of observing conditions, such as seeing and sky brightness). The effective étendue for LSST will be greater than $300~\mathrm{m}^2~\mathrm{deg}^2$, which is more than an order of magnitude larger than that of any existing facility. For example, the SDSS, with its 2.5 m telescope (Gunn et al. 2006) and a camera with 30 imaging CCDs (Gunn et al. 1998), has an effective étendue of only $5.9~\mathrm{m}^2~\mathrm{deg}^2$.

The range of scientific investigations that will be enabled by such a dramatic improvement in survey capability is extremely broad. Guided by the community-wide input assembled in the report of the Science Working Group of the LSST in 2004 (Science Working Group of the LSST & Strauss 2004), the LSST is designed to achieve goals set by four main science themes:

1. Probing dark energy and dark matter.
2. Taking an inventory of the solar system.
3. Exploring the transient optical sky.
4. Mapping the Milky Way.

Each of these four themes itself encompasses a variety of analyses, with varying sensitivity to instrumental and system parameters. These themes fully exercise the technical capabilities of the system, such as photometric and astrometric accuracy and image quality. About 90% of the observing time will be devoted to a deep-wide-fast (main) survey mode. The working paradigm is that all scientific investigations will utilize a common database constructed from an optimized observing program (the main survey mode), such as that discussed in Section 3.1. Here we briefly describe these science goals and the most challenging requirements for the telescope and instrument that are derived from those goals, which will inform the overall system design decisions discussed below. For a more detailed discussion, we refer the reader to the LSST Science Requirements Document (SRD; Ivezić & The LSST Science Collaboration 2011), the LSST Science Book (LSST Science Collaboration et al. 2009, hereafter SciBook), and links to technical papers and presentations at https://www.lsst.org/scientists.

2.1. The Main Science Drivers

The main science drivers are used to optimize various system parameters. Ultimately, in this high-dimensional parameter space, there is a manifold defined by the total project cost. The

science drivers must both justify this cost and provide guidance on how to optimize various parameters while staying within the cost envelope.

Here we summarize the dozen or so most important interlocking constraints on data and system properties placed by the four main science themes:

1. The depth of a single visit to a given field.
2. Image quality.
3. Photometric accuracy.
4. Astrometric accuracy.
5. Optimal exposure time.
6. The filter complement.
7. The distribution of revisit times (i.e., the cadence of observations), including the survey lifetime.
8. The total number of visits to a given area of sky.
9. The co-added survey depth.
10. The distribution of visits on the sky, and the total sky coverage.
11. The distribution of visits per filter.
12. Parameters characterizing data processing and data access (such as the maximum time allowed after each exposure to report transient sources, and the maximum allowed software contribution to measurement errors).

We present a detailed discussion of how these science-driven data properties are transformed to system parameters below.

2.1.1. Probing Dark Energy and Dark Matter

Current models of cosmology require the existence of both dark matter and dark energy to match observational constraints (Riess et al. 2007; Komatsu et al. 2009; Percival et al. 2010; LSST Dark Energy Science Collaboration 2012; Weinberg et al. 2015, and references therein). Dark energy affects the cosmic history of both the Hubble expansion and mass clustering. Distinguishing competing models for the physical nature of dark energy, or alternative explanations involving modifications of the general theory of relativity, will require percent-level measurements of both the cosmic expansion and the growth of dark matter structure as a function of redshift. Any given cosmological probe is sensitive to, and thus constrains degenerate combinations of, several cosmological and astrophysical/systematic parameters. Therefore, the most robust cosmological constraints are the result of using interlocking combinations of probes. The most powerful probes include weak gravitational lens cosmic shear (weak lensing (WL)), galaxy clustering and baryon acoustic oscillations (large-scale structure, LSS), the mass function and clustering of clusters of galaxies, time delays in lensed quasar and supernova (SN) systems, and photometry of Type Ia SNe—all as functions of redshift. Using the cosmic microwave background (CMB) fluctuations as the normalization, the combination of these probes can yield the needed precision to distinguish among models of dark energy (see, e.g., Zhan 2006, and references therein). The challenge is to turn this available precision into accuracy, by careful modeling and marginalization over a variety of systematic effects (see, e.g., Krause & Eifler 2017).

Meanwhile, there are a number of astrophysical probes of the fundamental properties of dark matter worth exploring, including, for example, weak- and strong-lensing observations of the mass distribution in galaxies and isolated and merging clusters, in conjunction with dynamical and X-ray observations

(see, e.g., Dawson et al. 2012; Newman et al. 2013; Rocha et al. 2013), the numbers and gamma-ray emission from dwarf satellite galaxies (see, e.g., Hargis et al. 2014; Drlica-Wagner et al. 2015), the subtle perturbations of stellar streams in the Milky Way halo by dark matter substructure (Belokurov & Koposov 2016), and massive compact halo object microlensing (Alcock et al. 2001).

Three of the primary dark energy probes, WL, LSS, and SN, provide unique and independent constraints on the LSST system design (SciBook, Chaps. 11–15).

WL techniques can be used to map the distribution of mass as a function of redshift and thereby trace the history of both the expansion of the universe and the growth of structure (e.g., Hu & Tegmark 1999; for recent reviews see Kilbinger 2015; Mandelbaum 2018). Measurements of cosmic shear as a function of redshift allow determination of angular distances versus cosmic time, providing multiple independent constraints on the nature of dark energy. These investigations require deep wide-area multicolor imaging with stringent requirements on shear systematics in at least two bands, and excellent photometry in at least five bands to measure photometric redshifts (a requirement shared with LSS, and indeed all extragalactic science drivers). The strongest constraints on the LSST image quality arise from this science program. In order to control systematic errors in shear measurement, the desired depth must be achieved with many short exposures (allowing for systematics in the measurement of galaxy shapes related to the point-spread functions [PSFs] and telescope pointing to be diagnosed and removed). Detailed simulations of WL techniques show that imaging over $\sim$20,000 deg^2 to a 5σ point-source depth of $r_{AB} \sim 27.5$ gives adequate signal to measure shapes for of order 2 billion galaxies for WL. These numbers are adequate to reach Stage IV goals for dark energy, as defined by the Dark Energy Task Force (Albrecht et al. 2006). This depth, as well as the corresponding deep surface brightness limit, optimizes the number of galaxies with measured shapes in ground-based seeing and allows their detection in significant numbers to beyond a redshift of two. Analyzing these data will require sophisticated data processing techniques. For example, rather than simply co-adding all images in a given region of sky, the individual exposures, each with their own PSF and noise characteristics, should be analyzed simultaneously to optimally measure the shapes of galaxies (Tyson et al. 2008; Jee & Tyson 2011).

SNe Ia provided the first robust evidence that the expansion of the universe is accelerating (Riess et al. 1998; Perlmutter et al. 1999). To fully exploit the SN science potential, light curves sampled in multiple bands every few days over the course of a few months are required. This is essential to search for systematic differences in SN populations (e.g., due to differing progenitor channels), which may masquerade as cosmological effects, as well as to determine photometric redshifts from the SNe themselves. Unlike other cosmological probes, even a single object gives information on the relationship between redshift and distance. Thus, a large number of SNe across the sky allows one to search for any dependence of dark energy properties on direction, which would be an indicator of new physics. The results from this method can be compared with similar measures of anisotropy from the combination of WL and LSS (Zhan et al. 2009). Given the expected SN flux distribution at the redshifts where dark energy is important, the single-visit depth should be at least $r \sim 24$.

Good image quality is required to separate SN photometrically from their host galaxies. Observations in at least five photometric bands will allow proper K-corrected light curves to be measured over a range of redshift. Carrying out these K-corrections requires that the calibration of the relative offsets in photometric zero-points between filters and the system response functions, especially near the edges of bandpasses, be accurate to about 1% (Wood-Vasey et al. 2007), similar to the requirements from photometric redshifts of galaxies. Deeper data ($r > 26$) for small areas of the sky can extend the discovery of SNe to a mean redshift of 0.7 (from $\sim$0.5 for the main survey), with some objects beyond $z \sim 1$ (Garnavich et al. 2004; Pinto et al. 2004; SciBook, Chap. 11). The added statistical leverage on the "pre-acceleration" era ($z \gtrsim 1$) would improve constraints on the properties of dark energy as a function of redshift.

Finally, there will be powerful cross-checks and complementarities with other planned or proposed surveys, such as *Euclid* (Laureijs et al. 2011) and *WFIRST* (Spergel et al. 2015), which will provide wide-field optical–IR imaging from space; DESI (Levi et al. 2013) and PFS (Takada et al. 2014), which will measure spectroscopic baryon acoustic oscillations (BAOs) with millions of galaxies; and SKA[88] (radio). Large survey volumes are key to probing dynamical dark energy models (with subhorizon dark energy clustering or anisotropic stresses). The cross-correlation of the three-dimensional mass distribution—as probed by neutral hydrogen in CHIME (Newburgh et al. 2014), HIRAX (Newburgh et al. 2016), or SKA, or galaxies in DESI and PFS—with the gravitational growth probed by tomographic shear in LSST will be a complementary way to constrain dark energy properties beyond simply characterizing its equation of state and to test the underlying theory of gravity. Current and future ground-based CMB experiments, such as Advanced ACT (De Bernardis et al. 2016), SPT-3G (Benson et al. 2014), Simons Observatory, and CMB Stage-4 (Abazajian et al. 2016), will also offer invaluable opportunities for cross-correlations with secondary CMB anisotropies.

2.1.2. Taking an Inventory of the Solar System

The small-body populations in the solar system, such as asteroids, trans-Neptunian objects (TNOs), and comets, are remnants of its early assembly. The history of accretion, collisional grinding, and perturbation by existing and vanished giant planets is preserved in the orbital elements and size distributions of those objects. Cataloging the orbital parameters, size distributions, colors, and light curves of these small-body populations requires a large number of observations in multiple filters and will lead to insights into planetary formation and evolution by providing the basis and constraints for new theoretical models. In addition, collisions in the main asteroid belt between Mars and Jupiter still occur and occasionally eject objects on orbits that may place them on a collision course with Earth. Studying the properties of main belt asteroids at subkilometer sizes is important for linking the near-Earth object (NEO) population with its source in the main belt. About 20% of NEOs, the potentially hazardous asteroids (PHAs), are in orbits that pass sufficiently close to Earth's orbit, to within 0.05 au, that perturbations on timescales of a century can lead to the possibility of collision. In 2005

---

[88] https://www.skatelescope.org

December, the US Congress directed[89] NASA to implement a survey that would catalog 90% of NEOs with diameters larger than 140 m by 2020.

Discovering and linking objects in the solar system moving with a wide range of apparent velocities (from several degrees per day for NEOs to a few arcseconds per day for the most distant TNOs) places strong constraints on the cadence of observations, requiring closely spaced pairs of observations (two or preferably three times per lunation) in order to link detections unambiguously and derive orbits (SciBook, Chap. 5). Individual exposures should be shorter than about 30 s to minimize the effects of trailing for the majority of moving objects. The images must be well sampled to enable accurate astrometry, with absolute accuracy of at least $0\rlap{.}''1$ in order to measure orbital parameters of TNOs with enough precision to constrain theoretical models and enable prediction of occultations. The photometric calibration should be better than 1%–2% to measure asteroids' colors and thus determine their types. If possible, the different filters should be observed over a short time span to reduce apparent variations in color due to changes in observing geometry, but they should be repeated over many lunations in order to determine phase curves and allow shape modeling.

The congressional mandate can be fulfilled with a 10 m class telescope equipped with a multi-gigapixel camera and a sophisticated and robust data processing system (Ivezić et al. 2007b). The images should reach a depth of at least 24.5 (5σ for point sources) in the r band to reach high completeness down to the 140 m mandate for NEOs. Such an instrument would probe the $\sim$100 m size range at main belt distances and discover rare distant TNOs such as Sedna (Brown et al. 2004) and 2012 VP113 (Trujillo & Sheppard 2014).

2.1.3. Exploring the Transient Optical Sky

Recent surveys have shown the power of measuring variability of celestial sources for studying gravitational lensing, searching for SNe, determining the physical properties of gamma-ray burst sources, discovering gravitational wave counterparts, probing the structure of active galactic nuclei (AGNs), studying variable star populations, discovering exoplanets, and many other subjects at the forefront of astrophysics (SciBook, Chap. 8; Law et al. 2009; Djorgovski et al. 2012; Rowe et al. 2014).

Time domain science has diverse requirements for transient and variable phenomena that are physically and phenomenologically heterogeneous. It requires large-area coverage to enhance the probability of detecting rare events; good image quality to enable differencing of images, especially in crowded fields; good time sampling, necessary to distinguish different types of variables and to infer their properties (e.g., determining the intrinsic peak luminosity of SNe Ia requires measuring their light-curve shape); accurate color information to classify variable objects; long-term persistent observations to characterize slow-evolving transients (e.g., tidal disruption events, superluminous SNe at high redshift, and luminous blue variables [LBVs]); and rapid data reduction, classification, and reporting to the community to allow immediate follow-up with spectroscopy, further optical photometry, and imaging in other wavebands.

Wide-area, dense temporal coverage to deep limiting magnitudes will enable the discovery and analysis of rare and exotic objects such as neutron stars and black hole binaries, novae and stellar flares, gamma-ray bursts and X-ray flashes, AGNs, stellar disruptions by black holes (Bloom et al. 2011; Gezari et al. 2012), and possibly new classes of transients, such as binary mergers of supermassive black holes (Shields & Bonning 2008), chaotic eruptions on stellar surfaces (Arnett & Meakin 2011), and, further yet, completely unexpected phenomena.

Such a survey would likely detect microlensing by stars and compact objects in the Milky Way, but also in the Local Group and perhaps beyond (de Jong et al. 2008). Given the duration of the LSST, it will also be possible to detect the parallax microlensing signal of intermediate-mass black holes and measure their masses (Gould 1992). This would open the possibility of discovering populations of binaries and planets via transits (e.g., Beaulieu et al. 2006; Drake et al. 2010; Choi et al. 2013; Batista et al. 2014), as well as obtaining spectra of lensed stars in distant galaxies.

A deep and persistent survey will discover precursors of explosive and eruptive transients and generate large samples of transients whose study has thus far been limited by small sample size (e.g., different subtypes of core-collapse SNe; Bianco et al. 2014).

Time series ranging between 1-minute and 10 yr cadence should be probed over a significant fraction of the sky. The survey's cadence will be sufficient, combined with the large coverage, to serendipitously catch very short-lived events, such as eclipses in ultracompact double-degenerate binary systems (Anderson et al. 2005); to constrain the properties of fast faint transients (such as optical flashes associated with gamma-ray bursts; Bloom et al. 2008); to detect electromagnetic counterparts to gravitational wave sources (Nissanke et al. 2013; Scolnic et al. 2018); and to further constrain the properties of new classes of transients discovered by programs such as the Deep Lens Survey (Becker et al. 2004), the Catalina Real-time Transient Survey (Drake et al. 2009), the Palomar Transient Factory (Law et al. 2009), and the Zwicky Transient Factory (Bellm 2014). Observations over a decade will enable the study of long-period variables, intermediate-mass black holes, and quasars (Kaspi et al. 2007; MacLeod et al. 2010; Graham et al. 2014; Chapline & Frampton 2016).

The next frontier in this field will require measuring the colors of fast transients and probing variability at faint magnitudes. Classification of transients in close-to-real time will require access to the full photometric history of the objects, both before and after the transient event (e.g., Mahabal et al. 2011).

2.1.4. Mapping the Milky Way

A major challenge in extragalactic cosmology today concerns the formation of structure on subgalactic scales, where baryon physics becomes important, and the nature of dark matter may manifest itself in observable ways (e.g., Weinberg et al. 2015). The Milky Way and its environment provide a unique data set for understanding the detailed processes that shape galaxy formation and for testing the small-scale predictions of our standard cosmological model. New insights into the nature and evolution of the Milky Way will require wide-field surveys to constrain its structure and accretion history. Further insights into the stellar populations

---

[89] For details see http://neo.jpl.nasa.gov/neo/report2007.html.

that make up the Milky Way can be gained with a comprehensive census of the stars within a few hundred parsecs of the Sun.

Mapping the Galaxy requires large-area coverage; excellent image quality to maximize photometric and astrometric accuracy, especially in crowded fields; photometric precision of at least 1% to separate main-sequence and giant stars (e.g., Helmi et al. 2003), as well as to identify variable stars such as RR Lyrae (Sesar et al. 2010; Sharma et al. 2011); and systematic astrometric errors not exceeding about 10 mas per observation to enable parallax and proper-motion measurements (SciBook, Chaps. 6 and 7). In order to probe the halo out to its presumed edge at $\sim$100 kpc (Ivezić et al. 2004) with main-sequence stars, the total co-added depth must reach $r > 27$, with a similar depth in the g band. The metallicity distribution of stars can be studied photometrically in the Sgr tidal stream (see, e.g., Majewski et al. 2003; Chou et al. 2007) and other halo substructures ($\sim$30 kpc; Carollo et al. 2007), yielding new insights into how they formed. Our ability to measure these metallicities is limited by the co-added depth in the u band; to probe the outer parts of the stellar halo, one must reach $u \sim 24.5$. To detect RR Lyrae stars beyond the Galaxy's tidal radius at $\sim$300 kpc, the single-visit depth must be $r \sim 24.5$.

In order to measure the tangential velocity of stars at a distance of 10 kpc, where the halo dominates over the disk, to within $10\,\mathrm{km\,s^{-1}}$ (comparable to the accuracy of large-scale radial velocity surveys), the proper-motion accuracy should be $0.2\,\mathrm{mas\,yr^{-1}}$ or better. This value was also chosen to approximately match the accuracy anticipated for the *Gaia* mission[90] (Perryman et al. 2001; de Bruijne 2012) at its faint limit ($r \sim 20$). Recent results from *Gaia* Data Release 2 (DR2) demonstrate that these early predictions of the mission performance were robust (Gaia Collaboration et al. 2018; Lindegren et al. 2018).

In order to measure distances to solar neighborhood stars out to a distance of 300 pc (the thin-disk scale height), with geometric distance accuracy of at least 30%, trigonometric parallax measurements accurate to 1 mas (1σ) are required over 10 yr. To achieve the required proper-motion and parallax accuracy with an assumed astrometric accuracy of 10 mas per observation per coordinate, approximately 1000 separate observations are required. This requirement for a large number of observations is similar to that from minimizing systematics in WL observations (Section 2.1.1).

2.1.5. A Summary and Synthesis of Science-driven Constraints on Data Properties

The goals of all the science programs discussed above (and many more, of course) can be accomplished by satisfying the minimal constraints listed below. For a more elaborate listing of various constraints, including detailed specification of various probability density distribution functions, please see the LSST SRD (Ivezić & The LSST Science Collaboration 2011) and the LSST Science Book (LSST Science Collaboration et al. 2009).

1. *The single-visit depth* should reach $r \sim 24.5$. This limit is primarily driven by the search for NEOs and variable sources (e.g., SNe, RR Lyrae stars) and by proper-motion

and trigonometric parallax measurements for stars. Indirectly, it is also driven by the requirements on the co-added survey depth and the minimum number of exposures required by WL science. We plan to split a single visit into two exposures of equal length to identify and remove cosmic rays.

2. *Image quality* should maintain the limit set by the atmosphere (the median free-air seeing is 0″65 in the r band at the chosen site; see Figure 1) and not be degraded appreciably by the hardware. In addition to stringent constraints from WL, good image quality is driven by the required survey depth for point sources and by image differencing techniques.

3. *Photometric repeatability* should achieve 5 mmag precision at the bright end, with zero-point stability across the sky of 10 mmag and band-to-band calibration errors not larger than 5 mmag. These requirements are driven by the need for high photometric redshift accuracy, the separation of stellar populations, detection of low-amplitude variable objects (such as eclipsing planetary systems), and the search for systematic effects in SN Ia light curves.

4. *Astrometric precision* should maintain the systematic limit set by the atmosphere, of about 10 mas per visit at the bright end (on scales below 20 arcmin). This precision is driven by the desire to achieve a proper-motion accuracy of $0.2\,\mathrm{mas\,yr^{-1}}$ and parallax accuracy of 1.0 mas over the course of a 10 yr survey (see Section 3.2.3).

5. *The single-visit exposure time* should be less than about a minute to prevent trailing of fast-moving objects and to aid control of various systematic effects induced by the atmosphere. It should be longer than $\sim$20 s to avoid significant efficiency losses due to finite readout, slew time, and read noise. As described above, we are planning to split each visit into two exposures.

6. *The filter complement* should include at least six filters in the wavelength range limited by atmospheric absorption and silicon detection efficiency (320–1050 nm), with roughly rectangular filters and no large gaps in the coverage, in order to enable robust and accurate photometric redshifts and stellar typing. An SDSS-like u band (Fukugita et al. 1996) is extremely important for separating low-redshift quasars from hot stars and for estimating the metallicities of F/G main-sequence stars. A bandpass with an effective wavelength of about 1 μm would enable studies of substellar objects, high-redshift quasars (to redshifts of $\sim$7.5), and regions of the Galaxy that are obscured by interstellar dust.

7. *The revisit time distribution* should enable determination of orbits of solar system objects and sample SN light curves every few days, while accommodating constraints set by proper-motion and trigonometric parallax measurements.

8. *The total number of visits* of any given area of sky, when accounting for all filters, should be of the order of 1000, as mandated by WL science, the search for NEOs, and proper-motion and trigonometric parallax measurements. Studies of transient sources also benefit from a large number of visits.

9. *The co-added survey depth* should reach $r \sim 27.5$, with sufficient signal-to-noise ratio (S/N) in other bands to address both extragalactic and Galactic science drivers.
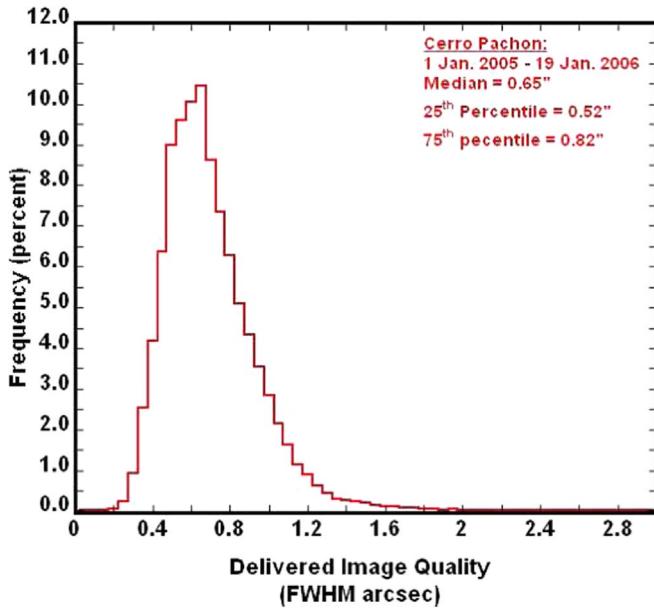
Figure 1. Image quality distribution measured at the Cerro Pachón site using a differential image motion monitor (DIMM) at $\lambda = 500$ nm, and corrected using an outer scale parameter of 30 m over an 8.4 m aperture. For details about the outer scale correction see Tokovinin (2002). The observed distribution is well described by a lognormal distribution, with the parameters shown in the figure.

10. *The distribution of visits per filter* should enable accurate photometric redshifts, separation of stellar populations, and sufficient depth to enable detection of faint extremely red sources (e.g., brown dwarfs and high-redshift quasars). Detailed simulations of photometric redshift uncertainties suggest a roughly similar number of visits among bandpasses (but because the system throughput and atmospheric properties are wavelength dependent, the achieved depths are different in different bands). The adopted time allocation (see Table 1) includes a slight preference to the *r* and *i* bands because of their dominant role in star/galaxy separation and WL measurements.

11. *The distribution of visits on the sky* should extend over at least ~18,000 deg² to obtain the required number of galaxies for WL studies, with attention paid to include "special" regions such as the ecliptic and Galactic planes, and the Large and Small Magellanic Clouds (if in the Southern Hemisphere). For comparison, the full area that can be observed at air mass less than 2.0 from any midlatitude site is about 30,000 deg².

12. *Data processing, data products, and data access* should result in data products that approach the statistical uncertainties in the raw data, i.e., the processing must be close to optimal. To enable fast and efficient response to transient sources, the processing latency for variable sources should be less than a minute, with a robust and accurate preliminary characterization of all reported variables.

Remarkably, even with these joint requirements, none of the individual science programs are severely overdesigned, i.e., despite their significant scientific diversity, these programs are highly compatible in terms of desired data characteristics. Indeed, any one of the four main science drivers could be removed, and the remaining three would still yield very similar requirements for most system parameters. As a result, the LSST

Table 1
The LSST Baseline Design and Survey Parameters

Quantity	Baseline Design Specification
Optical config.	Three-mirror modified Paul-Baker
Mount config.	Alt-azimuth
Final *f*-ratio, aperture	$f/1.234$, 8.4 m
Field of view, étendue	9.6 deg², 319 m²deg²
Plate scale	50.9 μm/arcsec (0.″2 pix)
Pixel count	3.2 gigapixels
Wavelength coverage	320–1050 nm, *ugrizy*
Single-visit depths, design[a]	23.9, 25.0, 24.7, 24.0, 23.3, 22.1
Single-visit depths, min.[b]	23.4, 24.6, 24.3, 23.6, 22.9, 21.7
Mean number of visits[c]	56, 80, 184, 184, 160, 160
Final (co-added) depths[d]	26.1, 27.4, 27.5, 26.8, 26.1, 24.9

Notes.
[a] Design specification from the Science Requirements Document (SRD; Ivezić & The LSST Science Collaboration 2011) for 5σ depths for point sources in the *ugrizy* bands, respectively. The listed values are expressed on the AB magnitude scale and correspond to point sources and fiducial zenith observations (about 0.2 mag loss of depth is expected for realistic air-mass distributions; see Table 2 for more details).
[b] Minimum specification from the Science Requirements Document for 5σ depths.
[c] An illustration of the distribution of the number of visits as a function of bandpass, taken from Table 24 in the SRD.
[d] Idealized depth of co-added images, based on design specification for 5σ depth and the number of visits in the penultimate row (taken from Table 24 in the SRD).

system can adopt a highly efficient survey strategy in which *a single data set serves most science programs* (instead of science-specific surveys executed in series). One can view this project as *massively parallel astrophysics*. The vast majority (about 90%) of the observing time will be devoted to a deep-wide-fast survey mode of the sort we have just described, with the remaining 10% allocated to special programs that will also address multiple science goals. Before describing these surveys in detail, we discuss the main system parameters.

2.2. The Main System Design Parameters

Given the minimum science-driven constraints on the data properties listed in the previous section, we now discuss how they are translated into constraints on the main system design parameters: the aperture size, the survey lifetime, the optimal exposure time, and the filter complement.

2.2.1. The Aperture Size

The product of the system's étendue and the survey lifetime, for given observing conditions, determines the sky area that can be surveyed to a given depth. The LSST field-of-view area is maximized to its practical limit, ~10 deg², determined by the requirement that the delivered image quality be dominated by atmospheric seeing at the chosen site (Cerro Pachón in northern Chile). A larger field of view would lead to unacceptable deterioration of the image quality. This constraint leaves the primary mirror diameter and survey lifetime as free parameters. The adopted survey lifetime of 10 yr is a compromise between a shorter time, which leads to an excessively large and expensive mirror (15 m for a 3 yr survey and 12 m for a 5 yr survey) and not as effective proper-motion measurements, and a smaller telescope, which would require more time to
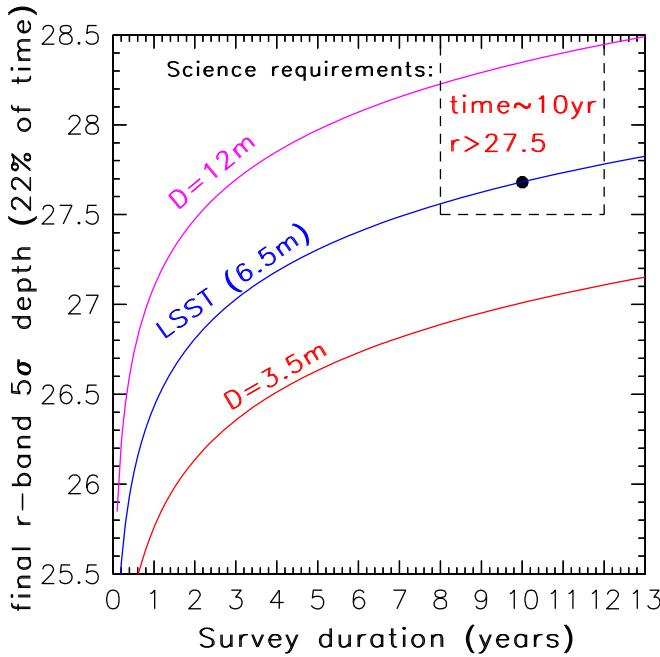
Figure 2. Co-added depth in the r band (AB magnitudes) vs. the effective aperture and the survey lifetime. It is assumed that 22% of the total observing time (corrected for weather and other losses) is allocated for the r band and that the ratio of the surveyed sky area to the field-of-view area is 2000.

complete the survey, with the associated increase in operations cost.

The primary mirror size is a function of the required survey depth and the desired sky coverage. By and large, the anticipated science outcome scales with the number of detected sources. For practically all astronomical source populations, in order to maximize the number of detected sources, it is more advantageous to maximize first the area and then the detection depth.[91] For this reason, the sky area for the main survey is maximized to its practical limit, 18,000 deg^2, determined by the requirement to avoid air masses less than 1.5, which would substantially deteriorate the image quality and the survey depth (see Equation (6)).

With the adopted field-of-view area, the sky coverage, and the survey lifetime fixed, the primary mirror diameter is fully driven by the required survey depth. There are two depth requirements: the final (co-added) survey depth, $r \sim 27.5$, and the depth of a single visit, $r \sim 24.5$. The two requirements are compatible if the number of visits is several hundred per band, which is in good agreement with independent science-driven requirements on the latter.

The required co-added survey depth provides a direct constraint, independent of the details of survey execution such as the exposure time per visit, on the minimum effective primary mirror diameter of 6.4 m, as illustrated in Figure 2.

---

[91] If the total exposure time is doubled and used to double the survey area, the number of sources increases by a factor of two. If the survey area is kept fixed, the increased exposure time will result in ~0.4 mag deeper data (see Equation (6)). For cumulative source counts described by $\log(N) = C + k * m$, the number of sources will increase by more than a factor of two only if $k > 0.75$. Apart from $z < 2$ quasars, practically all populations have k at most 0.6 (the Euclidean value), and faint stars and galaxies have $k < 0.5$. For more details, please see Nemiroff (2003).

2.2.2. The Optimal Exposure Time

The single-visit depth depends on both the primary mirror diameter and the chosen exposure time, t_{vis}. In turn, the exposure time determines the time interval to revisit a given sky position and the total number of visits, and each of these quantities has its own science drivers. We summarize these simultaneous constraints in terms of the single-visit exposure time:

1. The single-visit exposure time should not be longer than about a minute to prevent trailing of fast solar system moving objects and to enable efficient control of atmospheric systematics.
2. The mean revisit time (assuming uniform cadence) for a given position on the sky, n, scales as

$$n = \left(\frac{t_{\mathrm{vis}}}{10 \text{ s}}\right)\left(\frac{A_{\mathrm{sky}}}{10{,}000 \text{ deg}^2}\right)\left(\frac{10 \text{ deg}^2}{A_{\mathrm{FOV}}}\right) \text{days}, \qquad (1)$$

where two visits per night are assumed (required for efficient detection of solar system objects; see below) and the losses for realistic observing conditions have been taken into account (with the aid of the Operations Simulator described below). Science drivers such as SN light curves and moving objects in the solar system require that $n < 4$ days, or equivalently $t_{\mathrm{vis}} < 40$ s for the nominal values of A_{sky} and A_{FOV}.
3. The number of visits to a given position on the sky, N_{visit}, with losses for realistic observing conditions taken into account, is given by

$$N_{\mathrm{visit}} = \left(\frac{3000}{n}\right)\left(\frac{T}{10 \text{ yr}}\right). \qquad (2)$$

The requirement $N_{\mathrm{visit}} > 800$ again implies that $n < 4$ and $t_{\mathrm{vis}} < 40$ s if the survey lifetime, T, is about 10 yr.
4. These three requirements place a firm upper limit on the optimal visit exposure time of $t_{\mathrm{vis}} < 40$ s. Surveying efficiency (the ratio of open-shutter time to the total time spent per visit) considerations place a lower limit on t_{vis}, due to finite detector readout and telescope slew time (the longest acceptable readout time is set to 2 s, the shutter open-and-close time is 2 s, and the slew-and-settle time is set to 5 s, including the readout time for the second exposure in a visit):

$$\epsilon = \left(\frac{t_{\mathrm{vis}}}{t_{\mathrm{vis}} + 9 \text{ s}}\right). \qquad (3)$$

To maintain efficiency losses below ~30% (i.e., at least below the limit set by the weather patterns), and to minimize the read noise impact, $t_{\mathrm{vis}} > 20$ s is required.

Taking these constraints simultaneously into account, as summarized in Figure 3, yielded the following reference design:

1. A primary mirror effective diameter of ~6.5 m. With the adopted optical design, described below, this effective diameter corresponds to a geometrical diameter of ~8 m. Motivated by characteristics of the existing equipment at the Steward Mirror Laboratory, which fabricated the primary mirror, the adopted geometrical diameter is set to 8.4 m.
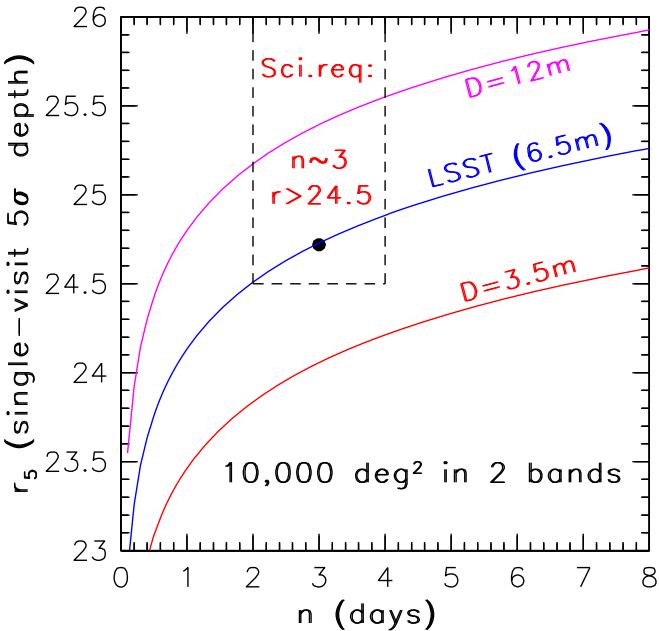
Figure 3. Single-visit depth in the r band (5σ detection for point sources, AB magnitudes) vs. revisit time, n (days), as a function of the effective aperture size. With a coverage of 10,000 deg^2 in two bands, the revisit time directly constrains the visit exposure time, $t_{vis} = 10n$ s. In addition to direct constraints on optimal exposure time, t_{vis} is also driven by requirements on the revisit time, n, the total number of visits per sky position over the survey lifetime, N_{visit}, and the survey efficiency, ϵ (see Equations (1)–(3)). Note that these constraints result in a fairly narrow range of allowed t_{vis} for the main deep-wide-fast survey.

2. A visit exposure time of 30 s (using two 15 s exposures to efficiently reject cosmic rays; the possibility of a single exposure per visit, to improve observing efficiency, will be investigated during the commissioning phase), yielding $\epsilon = 77\%$.

3. A revisit time of 3 days on average for 10,000 deg^2 of sky, with two visits per night.

To summarize, the chosen primary mirror diameter is the *minimum* diameter that simultaneously satisfies the depth ($r \sim 24.5$ for single visit and $r \sim 27.5$ for co-added depth) and cadence (revisit time of 3–4 days, with 30 s per visit) constraints described above.

2.3. System Design Trade-offs

We note that the Pan-STARRS project (Kaiser et al. 2002, 2010), with similar science goals to LSST, envisions a distributed aperture design, where the total system étendue is a sum of étendue values for an array of small 1.8 m telescopes.[92] Similarly, the LSST system could perhaps be made as two smaller copies with 6 m mirrors, or four copies with 4 m mirrors, or 16 copies with 2 m mirrors. Each of these clones would have to have its own 3-gigapixel camera (see below), and given the added risk and complexity (e.g., maintenance, data processing), the monolithic design seems advantageous for a system with such a large étendue as LSST.

It is informative to consider the trade-offs that would be required for a system with a smaller aperture, if the science requirements were to be maintained. For this comparison, we consider a four-telescope version of the Pan-STARRS survey (PS4). With an étendue about 6 times smaller than that of LSST (effective diameters of 6.4 and 3.0 m, and a field-of-view area of 9.6 deg^2 vs. 7.2 deg^2), and all observing conditions being equal, the PS4 system could in principle use a cadence identical to that of LSST. The main difference in the data sets would be a faint limit shallower by about 1 mag in a given survey lifetime. As a result, for Euclidean populations the sample sizes would go down by a factor of 4, while for populations of objects with a shallower slope of the number–magnitude relation (e.g., galaxies around a redshift of 1) the samples would be smaller by a factor of 2–3. The distance limits for nearby sources, such as Milky Way stars, would drop to 60% of their corresponding LSST values, and the NEO completeness level mandated by the US Congress would not be reached.

If instead the survey co-added depth were to be maintained, then the survey sky area would have to be 6 times smaller ($\sim$3500 deg^2). If the survey single-visit depth were to be maintained, then the exposure time would have to be about 6 times longer (ignoring the slight difference in the field-of-view area and simply scaling by the étendue ratio), resulting in non-negligible trailing losses for solar system objects and either (i) a factor of six smaller sky area observed within $n = 3$ days or (ii) the same sky area revisited every $n = 18$ days. Given these conflicts, one solution would be to split the observing time and allocate it to individual specialized programs (e.g., large sky area vs. deep co-added data vs. deep single-visit data vs. small-n data, etc.), as is being done by the PS1 Consortium.[93]

In summary, given the science requirements as stated here, there is a minimum étendue of $\sim$300 deg^2 m^2, which enables our seemingly disparate science goals to be addressed with a single data set. A system with a smaller étendue would require separate specialized surveys to address the science goals, which results in a loss of surveying efficiency.[94] The LSST is designed to reach this minimum étendue for the science goals stated in its SRD.

2.4. The Filter Complement

The LSST filter complement (*ugrizy*; see Figure 4) is modeled after the SDSS system (Fukugita et al. 1996) because of its demonstrated success in a wide variety of applications, including photometric redshifts of galaxies (Budavári et al. 2003), separation of stellar populations (Lenz et al. 1998; Helmi et al. 2003), and photometric selection of quasars (Richards et al. 2002; Ross et al. 2012). The extension of the SDSS system to longer wavelengths (the *y* band at $\sim$1 μm) is driven by the increased effective redshift range achievable with the LSST, due to deeper imaging; the desire to study substellar objects, high-redshift quasars, and regions of the Galaxy that are obscured by interstellar dust; and the scientific opportunity enabled by modern CCDs with high quantum efficiency in the near-infrared (NIR).

The chosen filter complement corresponds to a design "sweet spot." We have investigated the possibility of replacing the *ugrizy* system with a filter complement that includes only five filters. For example, each filter width could be increased by 20% over the same wavelength range (neither a shorter

---

[92] The first of these telescopes, PS1, has been operational for some time (Chambers et al. 2016) and has an étendue 1/24 that of LSST.

[93] More information about Pan-STARRS is available from http://pswww.ifa.hawaii.edu/pswww/.

[94] The converse is also true: for every étendue there is a set of optimal science goals that such a system can address with a high efficiency.
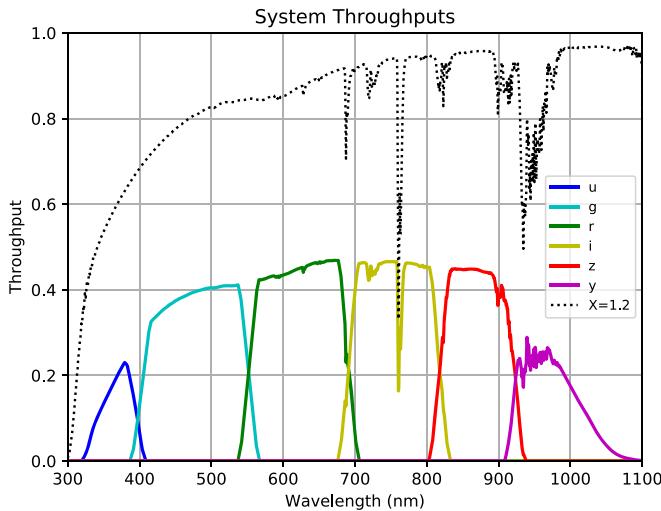
Figure 4. LSST bandpasses. The vertical axis shows the total throughput. The computation includes the atmospheric transmission (assuming an air mass of 1.2; dotted line), optics, and the detector sensitivity.
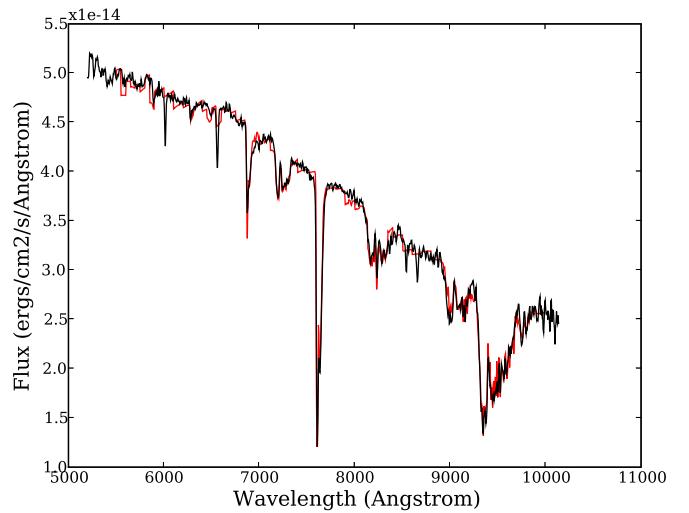

Figure 5. Example of determination of the atmospheric opacity by simultaneously fitting a three-parameter stellar model SED (Kurucz 1979) and six physical parameters of a sophisticated atmospheric model (MOD-TRAN; Anderson et al. 1999) to an observed F-type stellar spectrum (F_λ). The black line is the observed spectrum, and the red line is the best fit. Note that the atmospheric water feature around 0.9–1.0 μm is exquisitely well fit. The components of the best-fit atmospheric opacity are shown in Figure 6. Adapted from Burke et al. (2010).

wavelength range nor gaps in the wavelength coverage are desirable options), but this option is not satisfactory. Placing the red edge of the u band blueward of the Balmer break allows optimal separation of stars and quasars, and the telluric water absorption feature at 9500 Å effectively defines the blue edge of the y band. Of the remaining four filters (*griz*), the g band is already quite wide. As a last option, the *riz* bands could be redesigned as two wider bands. However, this option is also undesirable because the r and i bands are the primary bands for WL studies and for star/galaxy separation, and atmospheric dispersion would worsen the PSF for a wider bandpass (e.g., at air mass of 1.3, the typical dispersion in the u, g, and r bands is 0″55, 0″46, and 0″19, respectively; if the bandpass width increased by 50%, the dispersion would increase by a similar factor). The effects of atmospheric dispersion on WL studies are mitigated by modeling the PSF as a function of the color of the object (for more details, see Meyers & Burchat 2015; Carlsten et al. 2018).

2.5. The Calibration Methods

Precise determination of the PSF across each image, accurate photometric and astrometric calibration, and continuous monitoring of system performance and observing conditions will be needed to reach the full potential of the LSST mission. Extensive precursor data including the SDSS data set and our own data obtained using telescopes close to the LSST site of Cerro Pachón (e.g., the SOAR and Gemini South telescopes), as well as telescopes of similar aperture (e.g., Subaru), indicate that the photometric and astrometric accuracy will be limited not by our instrumentation or software, but rather by atmospheric effects.

The overall photometric calibration philosophy (Stubbs & Tonry 2006) is to measure explicitly, at 1 nm resolution, the instrumental sensitivity as a function of wavelength using light from a monochromatic source injected into the telescope pupil. The dose of delivered photons is measured using a calibration photodiode whose quantum efficiency is known to high accuracy. In addition, the LSST system will explicitly measure the atmospheric transmission spectrum associated with each image acquired. A dedicated 1.2 m auxiliary calibration telescope will obtain spectra of standard stars in LSST fields,
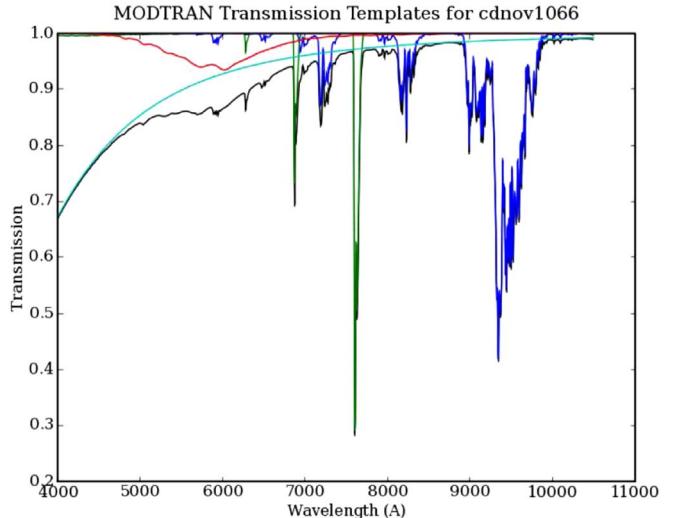

Figure 6. Components of the best-fit atmospheric opacity used to model the observed stellar spectrum shown in Figure 5. The atmosphere model (MODTRAN; Anderson et al. 1999) includes six components: water vapor (blue), oxygen and other trace molecules (green), ozone (red), Rayleigh scattering (cyan), a gray term with a transmission of 0.989 (not shown), and an aerosol contribution proportional to λ^{-1} and extinction of 1.3% at $\lambda = 0.675$ μm (not shown). The black line shows all six components combined. Adapted from Burke et al. (2010).

calibrating the atmospheric throughput as a function of wavelength (Stubbs et al. 2007; see Figures 5 and 6). The LSST auxiliary telescope will take data at lower spectral resolution ($R \sim 150$) but wider spectral coverage (340 nm–1.05 μm) than shown in these figures, using a slitless spectrograph and an LSST corner-raft CCD. Celestial spectro-photometric standard stars can be used as a separate means of photometric calibration, albeit only through the comparison of band-integrated fluxes with synthetic photometry calculations.
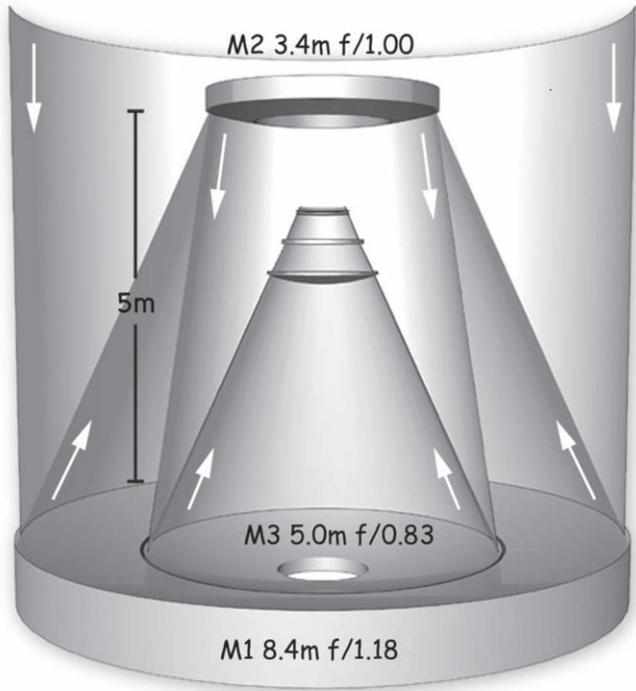
Figure 7. LSST baseline optical design (modified three-mirror Paul-Baker) with its unique monolithic mirror: the primary and tertiary mirrors are positioned such that they form a continuous compound surface, allowing them to be polished from a single substrate.
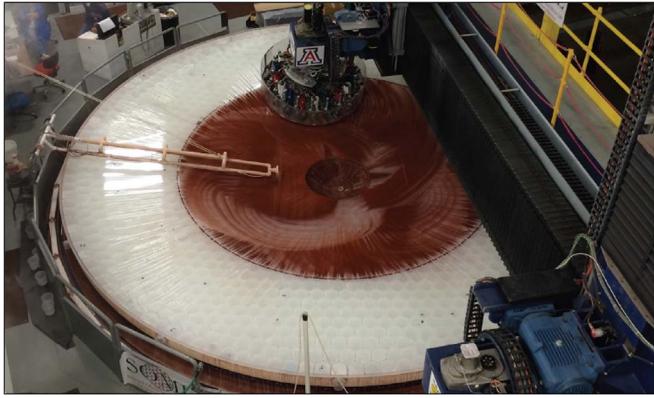

Figure 8. The polishing of the primary–tertiary mirror pair at the Richard F. Caris Mirror Lab at the University of Arizona in Tucson.

Figure 9. Top: artist's rendering of the dome enclosure with the attached summit support building on Cerro Pachón. The LSST auxiliary calibration telescope is shown on an adjacent rise to the right. Bottom: photograph of the LSST Observatory as of summer 2017. Note the different perspective from the artist's rendering. The main LSST telescope building is on the right, waiting for the dome to be installed. The auxiliary telescope building is on the left, with its dome being installed.
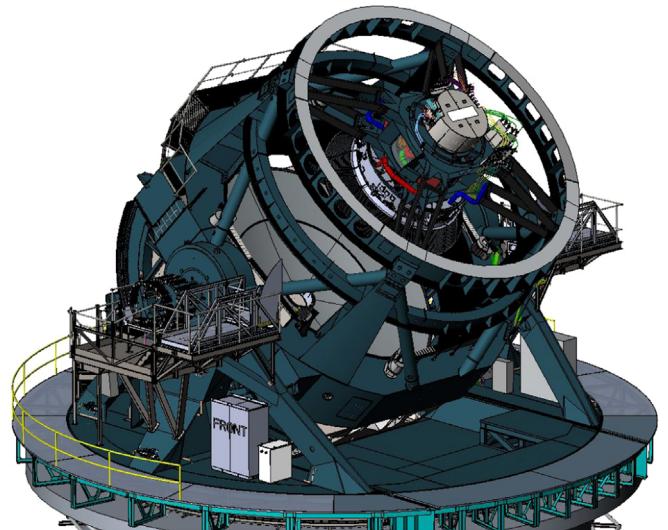
Figure 10. Baseline design for the LSST telescope. The small focal ratio allows for a very squat telescope, and thus a very stiff structure.

A similar calibration process has been undertaken by the Dark Energy Survey (DES) team, which has been approaching a calibration precision of 5 mmag (Burke et al. 2018).

SDSS, PS1, and DES data taken in good photometric conditions have approached the LSST requirement of 1% photometric calibration (Padmanabhan et al. 2008; Schlafly et al. 2012; Burke et al. 2018), although measurements with ground-based telescopes typically produce data with errors a factor of two or so larger. Analysis of repeated SDSS scans obtained in varying observing conditions demonstrates that data obtained in nonphotometric conditions can also be calibrated with sufficient accuracy (Ivezić et al. 2007a), as long as high-quality photometric data also exist in the region. The LSST calibration plan builds on this experience gained from SDSS and other surveys.

The planned calibration process decouples the establishment of a stable and uniform internal relative calibration from the task of assigning absolute optical flux to celestial objects.
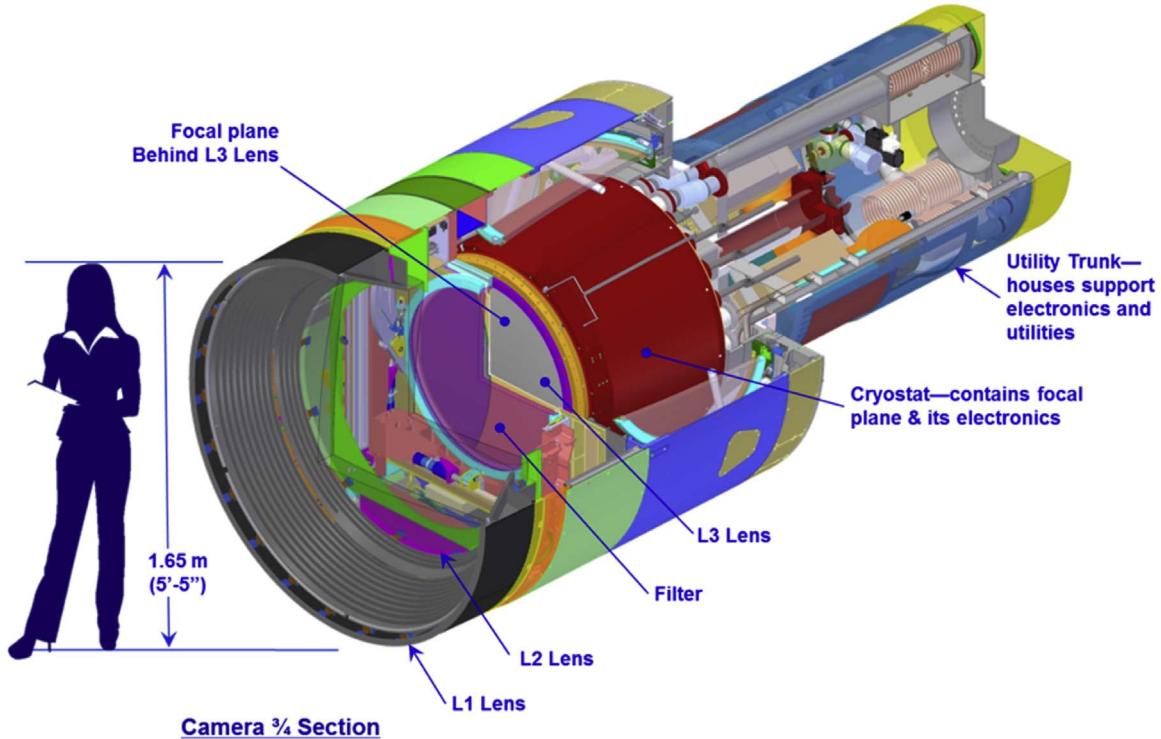
Figure 11. Cutaway view of LSST camera. Not shown are the shutter, which is positioned between the filter and lens L3, and the filter exchange system.

Celestial sources will be used to refine the internal photometric system and to monitor stability and uniformity of the photometric data. We expect to use Gaia Collaboration et al. (2016) photometry, utilizing the *BP* and *RP* photometric measurements, as well as the *G* magnitudes; for a subset of stars (e.g., F subdwarfs) we expect to be able to transfer this rigid photometric system above the atmosphere to objects observed by LSST. There will be >100 main-sequence stars with $17 < r < 20$ per detector (14×14 arcmin^2) even at high Galactic latitudes. Standardization of photometric scales will be achieved through direct observation of stars with well-understood spectral energy distributions (SEDs), in conjunction with the in-dome calibration system and the atmospheric transmission spectra.

Astrometric calibration will be based on the results from the *Gaia* mission (Lindegren et al. 2018), which will provide numerous high-accuracy astrometric standards in every LSST field.

2.6. The LSST Reference Design

We briefly describe the reference design for the main LSST system components. Detailed discussion of the flow-down from science requirements to system design parameters and extensive system engineering analysis can be found in the LSST Science Book (Chaps. 2–3).
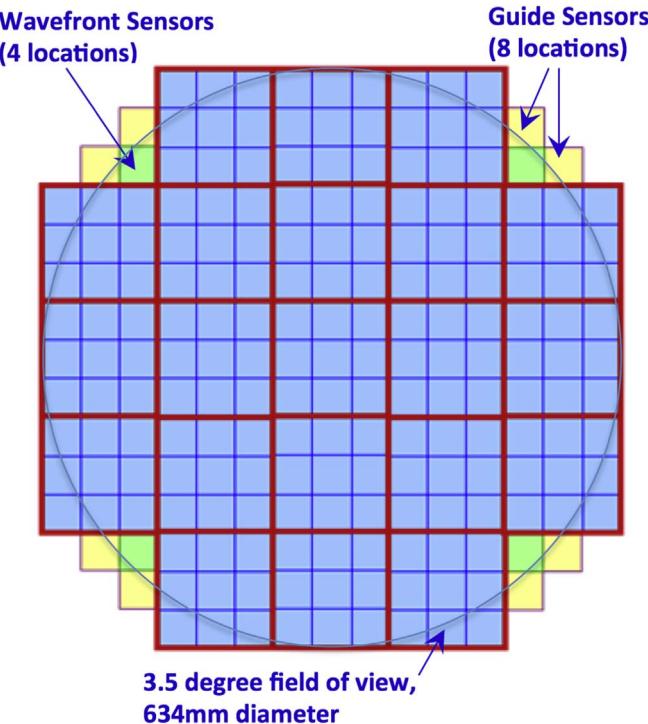
2.6.1. Telescope and Site

The large LSST étendue is achieved in a novel three-mirror design (modified Paul-Baker Mersenne-Schmidt system; Angel et al. 2000) with a very fast $f/1.234$ beam. The optical design has been optimized to yield a large field of view (9.6 deg^2), with seeing-limited image quality, across a wide wavelength band (320–1050 nm). Incident light is collected by an annular primary mirror, having an outer diameter of 8.4 m and inner diameter of 5.0 m, creating an effective filled aperture of ~6.4 m in diameter once vignetting is taken into account. The collected light is reflected to a 3.4 m convex secondary, then onto a 5 m concave tertiary, and finally into the three refractive lenses of the camera (see Figure 7). In broad terms, the primary–secondary mirror pair acts as a beam condenser, while the aspheric portion of the secondary and tertiary mirror acts as a Schmidt camera. The three-element refractive optics of the camera correct for the chromatic aberrations induced by the necessity of a thick Dewar window and flatten the focal surface. During design optimization, the primary and tertiary mirror surfaces were placed such that the primary's inner diameter coincides with the tertiary's outer diameter, thus making it possible to fabricate the mirror pair from a single monolithic blank using spin-cast borosilicate technology (see Figure 8). The secondary mirror is fabricated from a thin 100 mm thick meniscus substrate, made from Corning's ultra-low-expansion material. All three mirrors will be actively supported to control wavefront distortions introduced by gravity and environmental stresses on the telescope. The primary–tertiary mirror was cast and polished by the Richard F. Caris Mirror Lab at the University of Arizona in Tucson before being inspected and accepted by LSST in 2015 April (Araujo-Hauck et al. 2016). The primary–tertiary mirror cell was fabricated by CAID in Tucson and is undergoing acceptance tests. The integration of the actuators and final tests with the mirror is scheduled for early 2018.

The LSST Observing Facility (Figure 9), consisting of the telescope enclosure and summit support building, is being constructed atop Cerro Pachón in northern Chile, sharing the ridge with the Gemini South and SOAR telescopes[95] (the

---

[95] Coordinates listed in older versions of this paper were incorrect. We thank E. Mamajek for pointing out this error to us.

Figure 12. LSST Camera focal plane array. Each cyan square represents one 4K × 4K pixel sensor. Nine sensors are assembled into a raft; the 21 rafts are outlined in red. There are 189 science sensors, for a total of 3.2 gigapixels. Also shown are the four corner rafts, where the guide sensors and wavefront sensors are located.

center of the telescope pier is located at latitude S 30°14′40″68, longitude W 70°44′57″90, elevation 2652 m; Mamajek 2012). The telescope enclosure houses a compact, stiff telescope structure (see Figure 10) atop a 15 m high concrete pier with a fundamental frequency of 8 Hz, which is crucial for achieving the required fast slew-and-settle times. The height of the pier was set to place the telescope above the degrading effects of the turbulent ground layer. Capping the telescope enclosure is a 30 m diameter dome with extensive ventilation to reduce dome seeing and to maintain a uniform thermal environment over the course of the night. Furthermore, the summit support building has been oriented with respect to the prevailing winds to shed its turbulence away from the telescope enclosure. The summit support building includes a coating chamber for recoating the three LSST mirrors and clean room facilities for maintaining and servicing the camera.

2.6.2. Camera

The LSST camera provides a 3.2-gigapixel flat focal plane array, tiled by 189 4K × 4K CCD science sensors with 10 μm pixels (see Figures 11 and 12). This pixel count is a direct consequence of sampling the 9.6 deg^2 field of view (0.64 m diameter) with 0.2 × 0.2 arcsec^2 pixels (Nyquist sampling in the best expected seeing of ∼0″4). The sensors are deep depleted high-resistivity silicon back-illuminated devices with a highly segmented architecture that enables the entire array to be read in 2 s. The detectors are grouped into 3 × 3 rafts (see Figure 13); each contains its own dedicated electronics. The rafts are mounted on a silicon carbide grid inside a vacuum cryostat, with a custom thermal control system that maintains the CCDs at an operating temperature of around 173 K. The
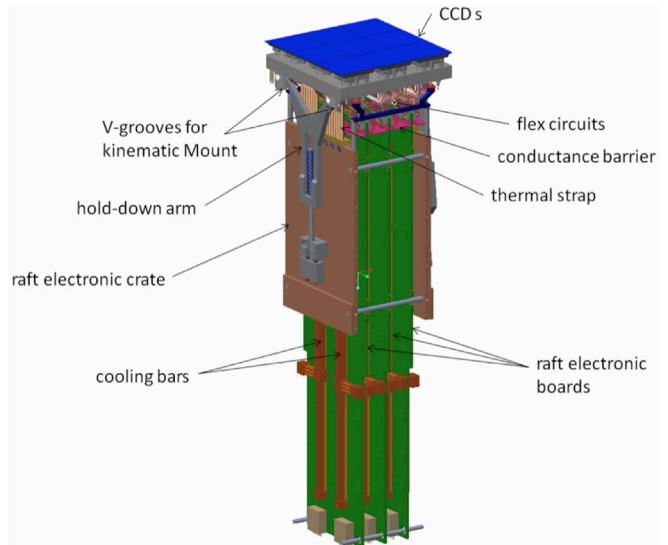
Figure 13. LSST Camera raft module, corresponding to the red squares in Figure 12, with nine sensors, integrated electronics, and thermal connections. Raft modules are designed to be replaceable.

entrance window to the cryostat is the third (L3) of the three refractive lenses in the camera. The other two lenses (L1 and L2) are mounted in an optics structure at the front of the camera body, which also contains a mechanical shutter and a carousel assembly that holds five large optical filters. The five filters in the camera can be changed in 90–120 s, depending on the initial camera rotator position. The sixth optical filter can replace any of the five via a procedure accomplished during daylight hours.

Each of the 21 rafts will host three front-end electronic boards (REB) operating in the cryostat (at −10°C) that read in parallel a total of 9 × 16 segments per CCD (144 video channels reading 1 million pixels each). This very high parallelization is the key to allowing for a fast readout (2 s) of the entire focal plane. To reach this performance with a reasonably sized board, a special low-noise (<3 electrons), low-cross-talk-between-channels (<0.02%), and low-power-dissipation (25 mW/channel) Analog Signal Processing Integrated Circuit, hosting eight channels per chip, has been developed, which is able to read the CCDs with a linearity better than 0.1% (Antilogus et al. 2017).

2.6.3. Data Management

The rapid cadence and scale of the LSST observing program will produce approximately 15 TB per night of raw imaging data[96] (about 20 TB with calibration exposures). As with all large modern surveys, the large data volume, the real-time aspects, and the complexity of processing involved require that the survey itself take on the task of fully reducing the data. The data collected by the LSST system will be automatically reduced to scientifically useful catalogs and images by the LSST Data Management (DM; Jurić et al. 2017a) system.

The detailed outputs of the LSST Data Management system are described in Section 3.3. The principal functions of the system are the following:

---

[96] For comparison, the volume of all imaging data collected over a decade by the SDSS-I/II projects and published in SDSS DR 7 (Abazajian et al. 2009) is approximately 16 TB.

Figure 14. LSST data flow from the mountain facilities in Chile to the data access center and processing center in the US and the satellite processing center in France.

1. Process, in real time, the incoming stream of images generated by the camera system during observing by archiving raw images, generating alerts to new sources or sources whose properties have changed, and updating the relevant catalogs (Prompt products; Section 3.3).

2. Process each night's data during the day and determine or refine orbits for all asteroids found in the imaging.

3. Periodically process the accumulated survey data to provide a uniform photometric and astrometric calibration, measure the properties of all detected objects, and characterize objects based on their time-dependent behavior. The results of such a processing run form a DR, which is a static, self-consistent data set suitable for use in performing scientific analyses of LSST data and publication of the results (the DR products; Section 3.3). We are planning two DRs covering the first year of full operations, and annual DRs thereafter.

4. Facilitate the creation of data products generated by the science community, by providing suitable software, application programming interfaces (APIs), and computing infrastructure at the LSST data access centers.

5. Make all LSST data available through an interface that utilizes community-based standards to the maximum possible extent. Provide enough processing, storage, and network bandwidth to enable user analyses of the data without the need for petabyte-scale data transfers.

Over the 10 yr of LSST operations and 11 DRs, this processing will result in a cumulative *processed* data size approaching 500 petabytes (PB) for imaging, and over 50 PB for the catalog databases. The final DR catalog database alone is expected to be approximately 15 PB in size.

The DM system will span four key facilities on three continents: the Summit Facility on Cerro Pachón in Chile (where the initial detector cross-talk correction will be performed); the Base Facility in La Serena, Chile (which will serve as a retransmission for data uploads to North America, as well as the Data Access Center for the Chilean community); the Data Processing and Archiving Facility at the National Center for Supercomputing Applications (NCSA) in Champaign-Urbana, IL; and the Satellite Processing Facility at CC-IN2P3 in Lyon, France. All real-time data processing and half the DR product processing will take place at the Data Processing and Archiving Facility, which will also serve as the Data Access Center for the US community. The other half of the DR processing will be done at CC-IN2P3, which will also have the role of "long-term storage" facility.

The data will be transported between the centers over existing and new high-speed optical fiber links from South America to the US (see Figure 14). The data processing center demands stable, well-tested technology to ensure smooth operations. Hence, while LSST is making a novel use of advances in information technology, it is not pushing the expected technology to the limit, reducing the overall risk to the project.

2.6.4. The LSST Software Stack

The *LSST Software Stack* is the data processing and analysis system developed by the LSST Project to enable LSST survey data reduction and delivery. It comprises all science pipelines needed to accomplish LSST data processing tasks (e.g., calibration, single-frame processing, co-addition, image differencing, multi-epoch measurement, and asteroid orbit determination; see Bosch et al. 2019 for an overview), the necessary data access (e.g., Jenness et al. 2019) and orchestration middleware, and the database and user interface components.
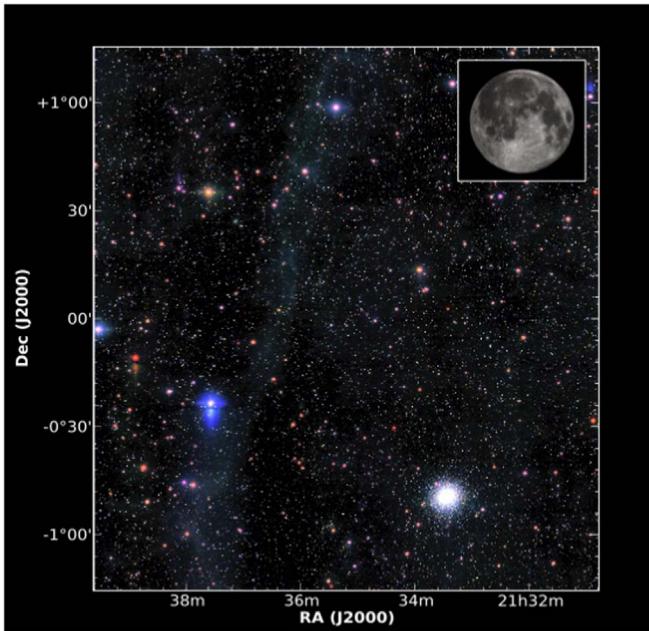
Figure 15. Small region in the vicinity of globular cluster M2, taken from a co-add of SDSS Stripe 82 data produced with LSST software stack prototypes. The co-addition employs a novel "background matching" technique that improves background estimation and preserves the diffuse structures in the resulting co-add.

Algorithm development for the LSST software builds on the expertise and experience of prior large astronomical surveys (including SDSS, Pan-STARRS, DES, SuperMACHO, ESSENCE, DLS, CFHTLS, and UKIDSS). The pipelines written for these surveys have demonstrated that it is possible to carry out largely autonomous data reduction of large data sets, automated detection of sources and objects, and the extraction of scientifically useful characteristics of those objects. While firmly footed in this prior history, the LSST software stack has largely been written anew, for reasons of performance, extendability, and maintainability. All LSST codes have been designed and implemented following software engineering best practices, including modularity, clear definition of interfaces, continuous integration, utilization of unit testing, and a single set of documentation and coding standards (Jenness et al. 2018). The primary implementation language is Python and, where necessary for performance reasons, C++.[97]

The LSST data management software has been prototyped for over 8 yr. Besides processing simulated LSST data (Section 2.7.3), it has been used to process images from CFHTLS (Cuillandre et al. 2012) and SDSS (Abazajian et al. 2009). As an example, Figure 15 shows a small region in the vicinity of M2 taken from a large co-addition of SDSS Stripe 82 data, generated with LSST software stack prototypes (Jurić et al. 2013).

Other than when prohibited by licensing, security, or other similar considerations, the LSST makes all newly developed source code, and especially that pertaining to scientific algorithms, public. Our primary goals in publicizing the code are to simplify reproducibility of LSST data products and to provide insight into algorithms used to create them. Achieving these goals requires that the source code is not only available

---

[97] All components implemented in C++ have been wrapped and exposed as Python modules to the rest of the system. Typical users should not have to work directly with the C++ layer.
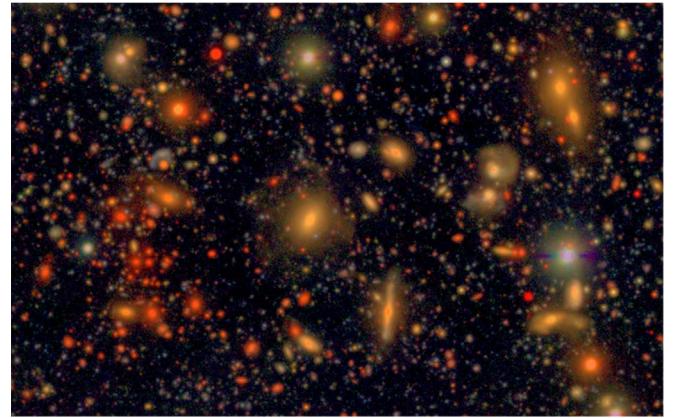

Figure 16. Small portion, $4' \times 6'$, of the HSC *gri* imaging of the COSMOS field. The limiting magnitude is about 27.5, roughly equivalent to 10 yr LSST depth.

but also appropriately documented at all levels. Given that, most of the LSST software stack is licensed under the terms of the GNU General Public License, Version 3, and can be found at https://github.com/lsst. The documentation for the LSST Science Pipelines components of the stack is available at https://pipelines.lsst.io.

The LSST Software Stack may be of interest and (re)used beyond the LSST project (e.g., by other survey projects, or by individual LSST end users). Enabling or supporting such applications goes beyond LSST's construction requirements; however, when developing the LSST codes, we strongly prefer design choices that enable future generalization. As an example of such reuse, a pipeline derived from the present-day LSST software stack prototypes has been used to reduce data taken with the HSC camera (Miyazaki et al. 2018) on Subaru as part of the large SSP survey (http://hsc.mtk.nao.ac.jp/ssp/survey; Aihara et al. 2018, Bosch et al. 2018; see Figure 16).

2.6.5. The LSST Database Design: Qserv

The scale of the LSST DR catalogs, in combination with desired targets for user concurrency and query response times, presents some engineering challenges. The LSST project has been developing *Qserv*, a shared-nothing MPP (massively parallel processing) database system, to meet these needs (Wang et al. 2011). Catalog data within Qserv are spatially partitioned and hosted on shard servers running on dedicated hardware resources within the LSST Data Facility. The shard servers locally leverage conventional RDBMS (relational database management system) technologies, running behind custom front-end codes that handle query analysis, rewrite, distribution, and result aggregation. The Qserv shard servers also provide a facility for cross-user synchronization of full-table scans in order to provide predictable query response times when serving many users concurrently. More details about Qserv can be found in the LSST document LDM-135 (Becla et al. 2017).

2.7. Simulating the LSST System

Throughout its design, construction, and commissioning, the LSST needs to be able to demonstrate that it can achieve the requirements laid out in the SRDs given its design and as-delivered components, that the system can be calibrated to the required level of fidelity, that the data management software can

extract the appropriate astrophysical signals, and that this can be achieved with sufficient efficiency such that the telescope can complete its primary objectives within a 10 yr survey.

Realizing these objectives requires that the project can characterize the performance of the LSST, including the performance of the opto-mechanical systems, the response of the detectors and their electronics, and the capabilities of the analysis software. A simulation framework provides such a capability, delivering a virtual prototype LSST against which design decisions, optimizations (including descoping), and trade studies can be evaluated (Connolly et al. 2014).

The framework underlying the LSST simulations is designed to be extensible and scalable (i.e., capable of being run on a single processor or across many thousand core compute clusters). It comprises four primary components: a simulation of the survey scheduler (Section 2.7.1); databases of simulated astrophysical catalogs of stars, galaxies, quasars, and solar system objects (Section 2.7.2); a system for generating observations based on the pointing of the telescope; and a system for generating realistic LSST images of a given area of sky (Section 2.7.3). Computationally intensive routines are written in C/C++, with the overall framework and database interactions using Python. The purpose of this design is to enable the generation of a wide range of data products for use by the collaboration, from all-sky catalogs used in simulations of the LSST calibration pipeline, to studies of the impact of survey cadence on recovering variability, to simulated images of a single LSST focal plane.

2.7.1. The LSST Operations Simulator

The LSST Operations Simulator (Delgado et al. 2014) was developed to enable a detailed quantitative analysis of the various science trade-offs described in this paper. It contains detailed models of site conditions, hardware and software performance, and an algorithm for scheduling observations that will, eventually, drive the largely robotic observatory. Observing conditions include a model for seeing derived from an extensive body of on-site Multi-Aperture Scintillation Sensor and Differential Image Motion Monitor (MASS/DIMM) measurements obtained during site selection and characterization (see Figure 1). It not only reproduces the observed seeing distribution but also includes the autocorrelation spectrum of seeing with time over intervals from minutes to seasons. Weather data are taken from 10 yr of hourly measurements at nearby Cerro Tololo. Thus, the simulator correctly represents the variation of limiting magnitude between pairs of observations used to detect NEOs and the correlation between, for example, seasonal weather patterns and observing conditions at any given point on the sky. In addition, downtime for observatory maintenance is also included.

The S/N of each observation is determined using a sky background model that includes the dark sky brightness in each filter, the effects of seeing and atmospheric transparency, and a detailed model for scattered light from the Moon and/or twilight at each observation (Yoachim et al. 2016). The time taken to move from one observation to the next is given by a detailed model of the camera, telescope, and dome. It includes such effects as the acceleration/deceleration profiles employed in moving the telescope, the dome, and the wind screen; the time needed to damp vibrations excited by each slew; cable wrap; the time taken for active optics lock and correction as a function of slew distance; and the time for filter changes and focal plane readout.

Observations are scheduled by a ranking algorithm. After a given exposure, all possible next observations are assigned a score that depends on their locations, times, and filters according to a set of scientific requirements that can vary with time and location. For example, if an ecliptic field has been observed in the r band, the score for another r-band observation of the same field will initially be quite low, but it will rise in time to peak about 1 hr after the first observation, and decline thereafter. This algorithm results in observations being acquired as pairs roughly an hour apart, which enables efficient association of NEO detections. To ensure uniform sky coverage, fields with fewer previous observations will be scored more highly than those that have already been observed more frequently.

Once all possible next observations have been scored for scientific priority, their scores are modified according to observing conditions (e.g., seeing, air mass, and sky brightness) and to criteria such as slew time to move from the current position, time required to change filters, etc. The highest-ranked observation is then performed, and the cycle repeats. The result of a simulator run is a detailed history of which locations on the sky were observed when, in what filter, and with what sky background, seeing, and other observing conditions. It takes a few days to produce a decade-long simulation using an average PC.

Results of the simulated surveys can be visualized and analyzed using a Python-based package called the Metrics Analysis Framework (MAF; Jones et al. 2014). MAF provides tools to analyze the properties of a survey (e.g., the distribution of air masses) through the creation of functions or metrics that are applied to OpSim outputs. These metrics can express the expected technical performance of the survey, such as the number of visits per field or the integrated depth after 10 yr, as well as the science capabilities or a survey, such as the number of SNe detected or the number of SNe with sufficient observations to have a well-characterized light curve.

2.7.2. Catalog Generation

The simulated astronomical catalogs (CatSim; Connolly et al. 2014) are stored in an SQL database. This base catalog is queried using sequences of observations derived from the Operations Simulator. Each simulated pointing provides a position and time of the observation, together with the appropriate sky conditions (e.g., seeing, moon phase and angle, sky brightness, and sky transparency). Positions of sources are propagated to the time of observation (including proper motions for stars and orbits for solar system sources). Magnitudes and source counts are derived using the atmospheric and filter response functions appropriate for the air mass of the observation and after applying corrections for source variability. The resulting catalogs are then formatted to be output to users, or to be fed into an image simulator.

The current version of the LSST simulation framework incorporates galaxies derived from an N-body simulation of a ΛCDM cosmology, quasars/AGNs, stars that match the observed stellar distributions within our Galaxy, asteroids generated from simulations of our solar system, and a 3D model for Galactic extinction. Stellar sources are based on the Galactic structure models of Jurić et al. (2008) and include thin-disk, thick-disk, and halo star components. The distribution and colors of the stars match those observed by SDSS. Each star in the simulation is matched to a template SED. Kurucz (1993) model spectra are used to represent

main-sequence F, G, and K stars, as well as RGB stars, blue horizontal branch stars, and RR Lyrae variables. SEDs for white dwarf stars are taken from Bergeron et al. (1995). SEDs for M, L, and T dwarfs are generated from a combination of spectral models and stacks of spectra from SDSS (e.g., Pettersen & Hawley 1989; Cushing et al. 2005; Burrows et al. 2006; Bochanski et al. 2007; Kowalski et al. 2010). The adopted metallicity for each star is based on a model from Ivezić et al. (2008), and proper motions are based on the kinematic model of Bond et al. (2010). Light-curve templates are assigned to a subset of the stellar population so that variability may also be simulated. This assignment and variability are matched to variability trends observed by the *Kepler* satellite and augmented by simulated distributions of RR Lyrae and Cepheids. For Galactic reddening, a value of $E(B-V)$ is assigned to each star using the three-dimensional Galactic model of Amôres & Lépine (2005). To provide consistency with the modeling of extragalactic fluxes in the simulations, the dust model in the Milky Way integrated to 100 kpc is renormalized to match the Schlegel et al. (1998) dust maps.

Galaxy catalogs are derived from the Millennium simulations of De Lucia et al. (2006). These models extend pure dark matter *N*-body simulations to include gas cooling, star formation, SNe, and AGNs and are designed to reproduce the observed colors, luminosities, and clustering of galaxies as a function of redshift. To generate the LSST simulated catalogs, a light cone, covering redshifts $0 < z < 6$, was constructed from 58 simulation snapshots $500\,h^{-1}$ Mpc on a side. This light cone extends to a depth of approximately $r = 28$ and covers a $4\overset{\circ}{.}5 \times 4\overset{\circ}{.}5$ footprint on the sky. Replicating this catalog across the sky simulates the full LSST footprint. As with the stellar catalog, an SED is fit to the colors of each source using Bruzual & Charlot (2003) spectral synthesis models. These fits are undertaken separately for the bulge and disk components and, for the disk, include inclination-dependent reddening. Morphologies are modeled using two Sérsic profiles. The bulge-to-disk ratio and disk scale lengths are taken from De Lucia et al. (2006). Half-light radii for bulges are estimated using the empirical absolute magnitude versus half-light radius relation given by González et al. (2009). Comparisons of the redshift and number–magnitude distributions of the simulated catalogs with those derived from deep imaging and spectroscopic surveys showed that the De Lucia et al. (2006) models underpredict the density of sources at faint magnitudes and high redshifts. To correct for these effects, sources are cloned in magnitude and redshift space until their densities reflect the average observed properties.

Quasar/AGN catalogs are generated using the Bongiorno et al. (2007) luminosity function for $M_B < -15$. Their observed SEDs are generated using a composite rest-frame spectrum derived from SDSS data by Vanden Berk et al. (2001). The host galaxy is selected to have the closest match to the preferred stellar mass and color at the AGN's redshift, following the results from Xue et al. (2010). Each galaxy hosts at most one AGN, and no explicit distinction is made between low-luminosity AGNs and quasars that dramatically outshine their host galaxies. The light curve for each AGN is generated using a damped random walk model and prescriptions given by MacLeod et al. (2010).

Asteroids are simulated using the solar system models of Grav et al. (2007). They include NEOs; main belt asteroids; the Trojans of Mars, Jupiter, Saturn, Uranus, and Neptune; TNOs; and Centaurs. SEDs are assigned using the C- and S-type asteroids of DeMeo et al. (2009). Positions for the 11 million asteroids in the simulation are stored within the base catalog (sampled once per night for the 10 yr duration of the LSST survey). We generate accurate ephemerides of all asteroids falling within a given LSST point using the *OpenOrb* software package (Granvik et al. 2009). With typically 8000 sources per LSST field of view, this procedure significantly reduces the computational resources required to simulate asteroid ephemerides.

2.7.3. Image Simulations

The framework described above provides a parameterized view of the sky above the atmosphere. Images are simulated using two packages: GalSim (Rowe et al. 2015), and Phosim (Peterson et al. 2015). Galsim is a modular and open-source package that provides a library for simulating stars and galaxies through a range of modern astronomical telescopes. PSFs are either treated as analytic functions or modeled from ray-traced optics. Convolutions by the PSF can be applied to parameterized galaxy profiles (e.g., Sérsic profiles) or to directly observed images. Operations are applied in Fourier space to enable an effective trade-off between speed of simulation and accuracy. GalSim is written in C++ with a Python API and is integrated within the LSST CatSim framework.

Phosim is an open-source package that simulates images by drawing photons from the SED of each source (scaled to the appropriate flux density based on the apparent magnitude of a source and accounting for the spatial distribution of light for extended sources). Each photon is ray-traced through the atmosphere, telescope, and camera to generate a CCD image. The atmosphere is modeled using a Taylor frozen screen approximation (with the atmosphere described by six layers). The density fluctuations within these screens are described by a Kolmogorov spectrum with an outer scale (typically 10–200 m). All screens move during an exposure, with velocities derived from NOAA measurements of the wind velocities above the LSST site in Chile. Typical velocities are on the order of $20\,\mathrm{m\,s^{-1}}$ and are found to have a seasonable dependence that is modeled when generating the screens. Each photon's trajectory is altered due to refraction as it passes through each screen.

After the atmospheric refraction, the photons in PhoSim are reflected and refracted by the optical surfaces within the telescope and camera. The mirrors and lenses are simulated using geometric optics techniques in a fast ray-tracing algorithm, and all optical surfaces include a spectrum of perturbations based on design tolerances. Each optic moves according to its six degrees of freedom within tolerances specified by the LSST system. Fast techniques for finding intercepts on the aspheric surface and altering the trajectory of a photon by reflection or wavelength-dependent refraction have been implemented to optimize the efficiency of the simulated images. Wavelength- and angle-dependent transmission functions are incorporated within each of these techniques, including simulation of the telescope spider.

Both GalSim and PhoSim model the propagation of photons through the silicon of the detector. The conversion probability, refraction as a function of wavelength and temperature, and charge diffusion within the silicon are modeled for all photons. Photons are pixelated and the readout process simulated including blooming, charge saturation, charge transfer inefficiency, gain and offsets, hot pixels and columns, the dependence of the image size on intensity (aka the "brighter-fatter" effect), and QE variations.
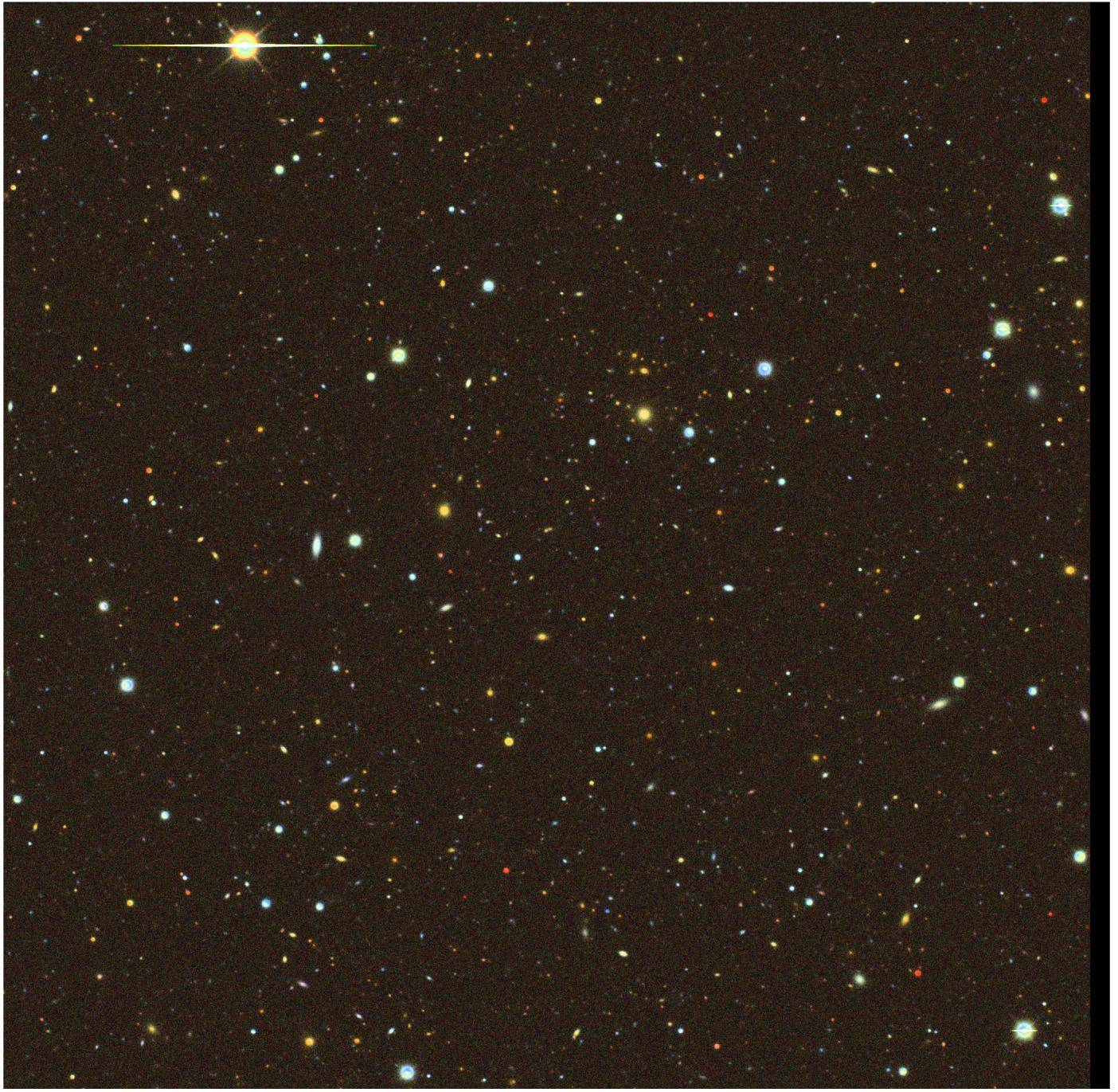
Figure 17. Simulated image of a single LSST CCD using PhoSim (covering a 13.3 × 13.3 arcmin^2 region of the sky). The image is a color composite (Lupton et al. 2004) from a set of 30 s *gri* visits.

An example of a simulated LSST image using PhoSim is shown in Figure 17.

3. Anticipated Data Products and Their Characteristics

The LSST observing strategy is designed to maximize the scientific throughput by minimizing slew and other downtime and by making appropriate choices of the filter bands given the real-time weather conditions. Using simulated surveys produced with the Operations Simulator described in Section 2.7.1, we illustrate predictions of LSST performance with two examples.

3.1. The Baseline LSST Surveys

The fundamental basis of the LSST concept is to scan the sky deep, wide, and fast and to obtain a data set that simultaneously satisfies the majority of the science goals. We present here a specific realization, the so-called "universal cadence," which yields the main deep-wide-fast survey and meets our core science goals. However, at this writing, there is a vigorous discussion of cadence plans in the LSST community, exploring variants and alternatives that enhance various specific science programs, while maintaining the science requirements described in the SRD.

Benchmark survey baseline2018a
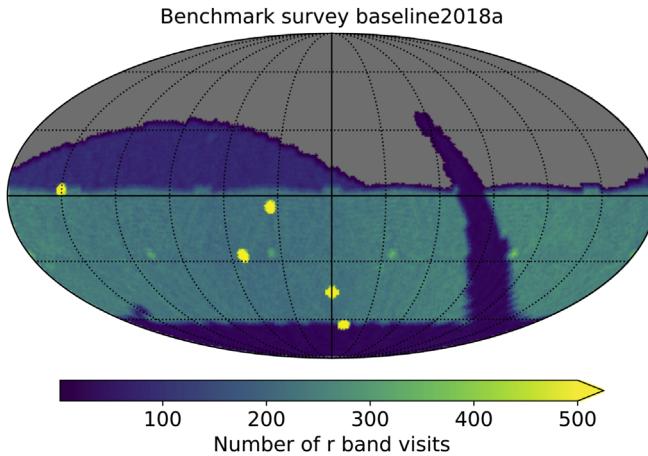
Figure 18. Distribution of the *r*-band visits on the sky for a simulated realization of the baseline cadence. The sky is shown in the equal-area Mollweide projection in equatorial coordinates (the vernal equinoctial point is in the center, and the R.A. is increasing from right to left). The number of visits for a 10 yr survey is color-coded according to the legend. The three regions with smaller number of visits than the main survey ("mini-surveys") are the Galactic plane (arc on the right), the region around the south celestial pole (bottom), and the so-called "northern ecliptic region" (upper left; added in order to increase completeness for moving objects). Deep Drilling Fields, with a much higher number of visits ($\approx$2500–4500 in the *r* band) than the main survey (a median over all fields of 200 visits in the *r* band), are also visible as small circles. The fields were dithered on subfield scales, and pixels with angular resolution of $\sim$30 arcmin were used to evaluate and display the coverage. The slightly elevated number of visits for four locations along the decl. $\approx -30°$ line is due to the pattern of the pointing tessellation on the sky.

The main deep-wide-fast survey will use about 90% of the observing time. The remaining 10% of the observing time will be used to obtain improved coverage of parameter space such as very deep ($r \sim 26$) observations, observations with very short revisit times ($\sim$1 minute), and observations of "special" regions such as the ecliptic plane, Galactic plane, and the Large and Small Magellanic Clouds.

3.1.1. The Main Deep-wide-fast Survey and Its Extensions

The observing strategy for the main survey will be optimized for the homogeneity of depth and number of visits. In times of good seeing and at low air mass, preference is given to *r*- and *i*-band observations. As often as possible, each field will be observed twice, with visits separated by 15–60 minutes. This strategy will provide motion vectors to link detections of moving objects in the solar system and fine-time sampling for measuring short-period variability. The ranking criteria also ensure that the visits to each field are widely distributed in position angle on the sky and rotation angle of the camera in order to minimize systematic effects in galaxy shape determination.

The universal cadence provides most of LSST's power for detecting NEOs and Kuiper Belt objects (KBOs) and naturally incorporates the southern half of the ecliptic within its 18,000 square degrees, with a decl. cut of about $\delta = +2°$. Additional coverage of a crescent within 10 degrees of the northern ecliptic plane would sample the full azimuthal distribution of KBOs, crucial for understanding the different dynamical families in which they fall. Thus, we plan to extend the universal cadence to this region using the *r* and *i* filters only, along with more relaxed limits on air mass and seeing. Relaxed limits on air mass and seeing are also adopted for $\sim$700 deg^2

around the south celestial pole, allowing coverage of the Large and Small Magellanic Clouds (Figure 18).

Finally, the universal cadence proposal excludes observations at low Galactic latitudes, where the high stellar density leads to a confusion limit at much brighter magnitudes than those attained in the rest of the survey. Within this region, the Galactic plane proposal provides 30 observations in each of the six filters, distributed roughly logarithmically in time (it may not be necessary to use the *u* and *g* filters for this heavily extincted region).

The resulting sky coverage for the LSST baseline cadence (known internally as *baseline2018a*), based on detailed operations simulations, is shown for the *r* band in Figure 18. The anticipated total number of visits for a 10 yr LSST survey is about 2.45 million ($\sim$4.9 million 15 s long exposures, summing over the six filters). The per-band allocation of these visits is shown in Table 1. Details of the cadence of visits over a single season, for two distinct pointings, are shown in Figure 19.

The baseline universal cadence is by no means the definitive plan for the entire survey. Rather, it represents a proof of concept that it is indeed possible to design a observing strategy that addresses a wide variety of science goals in a nearly optimal way. With input and engagement of the community, we are undertaking a vigorous and systematic research effort to explore the enormously large parameter space of possible surveys (see LSST Science Collaboration et al. 2017). The scientific commissioning period will be used to test the usefulness of various observing modes and to explore alternative strategies.

3.1.2. Mini-surveys and Deep Drilling Fields

Although the uniform treatment of the sky provided by the universal cadence proposal can satisfy the majority of LSST scientific goals, roughly 10% of the time will be allocated to other strategies that significantly enhance the scientific return. These surveys aim to extend the parameter space accessible to the main survey by going deeper or by employing different time/filter sampling. We have already discussed three examples of such mini-surveys: the northern ecliptic spur to improve completeness of the asteroid and KBO population, the southern celestial cap to extend the survey footprint to the South Pole (thus providing coverage of the Magellanic Clouds), and the Galactic plane survey to include low Galactic latitude fields.

As an additional example of a mini-survey, consider a program that uses 1 hr of observing time per night to observe a single pointing (9.6 deg^2) to substantially greater depth in individual visits. Accounting for readout time and filter changes, it could obtain about 50 consecutive 15 s exposures in each of four filters in an hour. If a field is visited every 2 days over 4 months, about 600 deg^2 can be observed with this cadence over 10 yr. Taking weather into account, the selected fields would each have on average about 40 hr long sequences of 200 exposures each. Each 15 s exposure in a sequence would have an equivalent 5σ depth of $r \sim 24$, and each filter subsequence when co-added would be 2 mag deeper than the main survey visits ($r \sim 26.5$). When all 40 sequences and the main survey visits are co-added, they would extend the depth to $r \sim 28$.
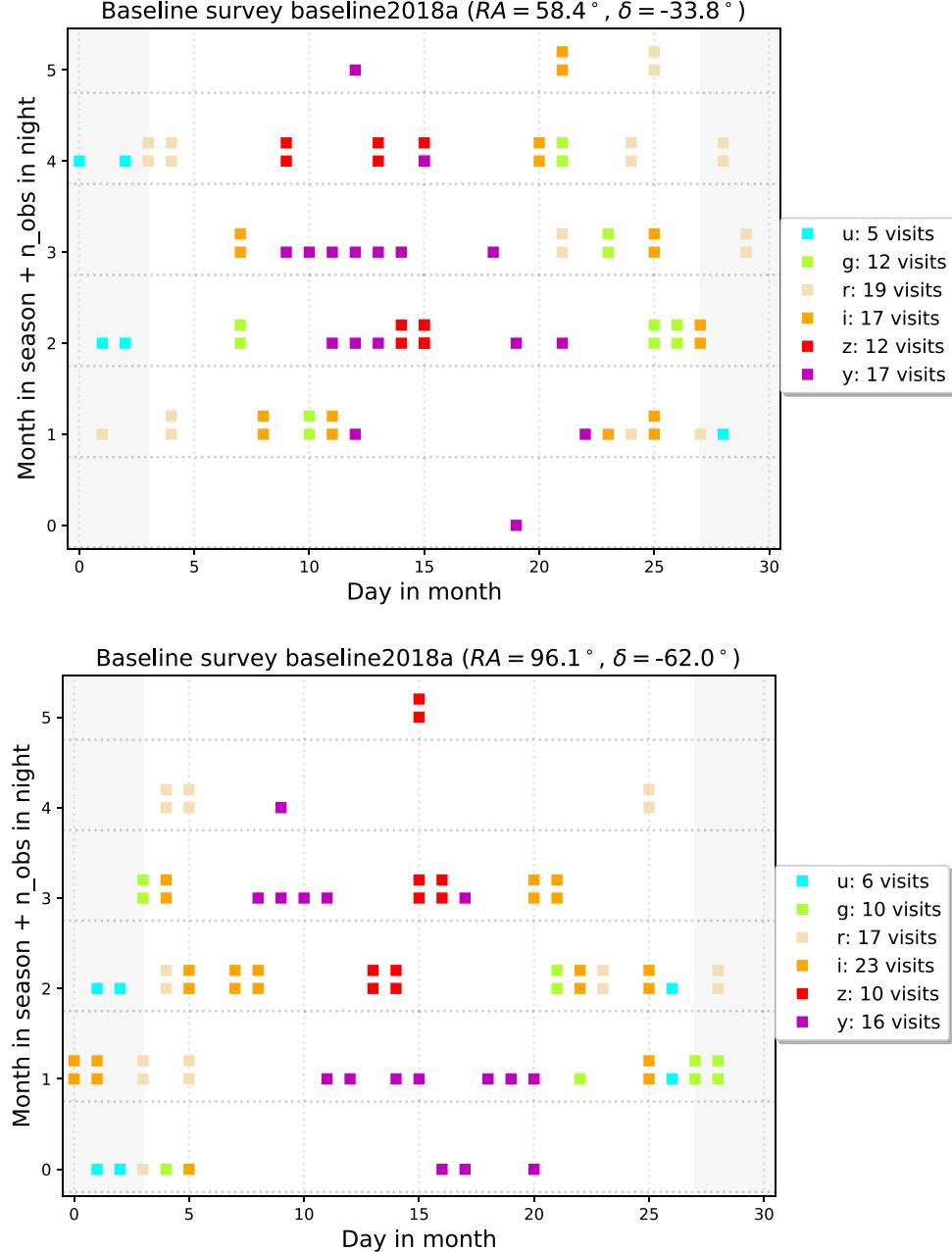
Figure 19. Distribution of visits over a single season at two distinct pointings, for a simulated realization of the baseline cadence. Two pointings within the "Wide Fast Deep" universal cadence footprint were chosen, one nearly overhead at the LSST site and one near the southern limit of the WFD footprint. The timing of the visits within the season is illustrated in the figure by calculating the month within the season (shown in the y-axis location in the plot), the night within the month (x-axis location in the plot), and number of visits within each night (a small additional offset in the y-axis). Each visit is color-coded according to its observed filter; the shaded gray regions show the nights around new moon.

This data set would be excellent for a wide variety of science programs. The individual sequences would be sensitive to 1% variability on subminute timescales, allowing discovery of planetary eclipses and of interstellar scintillation effects, expected when the light of a background star propagates through a turbulent gas medium (Moniez 2003; Habibi et al. 2011). If these fields were selected at Galactic latitudes of $|b| \sim 30°$, they would include about 10 million stars with $r < 21$ observed with S/N above 100 in each visit. When subsequences from a given night were co-added, they would provide dense time sampling to a faint limit of $r \sim 26.5$ and would enable deep searches for SNe, TNOs, and other faint transient, moving, and variable sources. For example, the SN

sample would be extended to redshifts of $z \sim 1.2$, with more densely sampled light curves than obtained from the universal cadence. Such sequences would also serve as excellent tests of our photometric calibration procedures.

The LSST has already selected four distant extragalactic survey fields[98] that the project guarantees to observe as Deep Drilling Fields with deeper coverage and more frequent temporal sampling than provided by the standard LSST observing pattern. These fields (Elias S1, XMM-LSS, Extended Chandra Deep Field-South, and COSMOS) are well-studied

---

[98] For details, see https://www.lsst.org/News/enews/deep-drilling-201202.html.

Table 2
Parameters from Equations (5) and (6)

Parameter	u	g	r	i	z	y
m_{sky} [a]	22.99	22.26	21.20	20.48	19.60	18.61
θ [b]	0.81	0.77	0.73	0.71	0.69	0.68
θ_{eff} [c]	0.92	0.87	0.83	0.80	0.78	0.76
γ [d]	0.038	0.039	0.039	0.039	0.039	0.039
k_m [e]	0.491	0.213	0.126	0.096	0.069	0.170
C_m [f]	23.09	24.42	24.44	24.32	24.16	23.73
m_5 [g]	23.78	24.81	24.35	23.92	23.34	22.45
ΔC_m^{∞} [h]	0.62	0.18	0.10	0.07	0.05	0.04
$\Delta C_m(2)$ [i]	0.23	0.08	0.05	0.03	0.02	0.02
Δm_5 [j]	0.21	0.16	0.14	0.13	0.13	0.14

Notes.
[a] The expected median zenith sky brightness at Cerro Pachón (AB mag arcsec^{-2}).
[b] The expected delivered median zenith seeing (FWHM, arcseconds). The seeing approximately scales with air mass, X, as $X^{0.6}$.
[c] The effective zenith seeing (arcseconds) used for m_5 computation.
[d] The band-dependent parameter from Equation (5).
[e] Adopted atmospheric extinction.
[f] The band-dependent parameter from Equation (6).
[g] The typical 5σ depth for point sources at zenith, assuming exposure time of 2×15 s, and observing conditions as listed. For larger air mass the 5σ depth is brighter; see the bottom row.
[h] The loss of depth due to instrumental noise (assuming 9 e$^-$ per pixel and readout, and two readouts per visit).
[i] Additive correction to C_m when exposure time is doubled from its fiducial value to 60 s.
[j] The loss of depth at air mass of $X = 1.2$ due to seeing degradation and increased atmospheric extinction.

survey fields with substantial existing multiwavelength coverage and other positive attributes. These four fields are only the first chosen for deep-drilling observations. The project plans a community call for white papers suggesting additional Deep Drilling Fields and other specialized observing cadences.

3.2. Detailed Analysis of Simulated Surveys

As examples of analysis enabled by the Operations Simulator (Section 2.7.1), we describe determination of the completeness of the LSST NEO sample, and estimation of errors expected for trigonometric parallax and proper-motion measurements. In both examples, the conclusions crucially depend on the assumed accuracy of the photometry and astrometry, as we now describe.

3.2.1. Expected Photometric S/N

The output of operations simulations is a data stream consisting of a position on the sky and the time of observation, together with observing conditions such as seeing and sky brightness. The expected photometric error in magnitudes (roughly the inverse of the S/N) for a single visit can be written as

$$\sigma_1^2 = \sigma_{sys}^2 + \sigma_{rand}^2, \qquad (4)$$

where σ_{rand} is the random photometric error and σ_{sys} is the systematic photometric error (due to, e.g., imperfect modeling of the PSF, but not including uncertainties in the absolute photometric zero-point). The calibration system and procedures are designed to maintain $\sigma_{sys} < 0.005$ mag. Based on SDSS experience (Sesar et al. 2007), the random photometric error for

point sources, as a function of magnitude, is well described[99] by

$$\sigma_{rand}^2 = (0.04 - \gamma)x + \gamma x^2 \ (mag^2), \qquad (5)$$

with $x \equiv 10^{0.4(m - m_5)}$. Here m_5 is the 5σ depth (for point sources) in a given band, and γ depends on the sky brightness, readout noise, etc. Detailed determination of the system throughput yields the values of γ listed in Table 2. The 5σ depth for point sources is determined from

$$m_5 = C_m + 0.50(m_{sky} - 21) + 2.5 \log_{10}(0.7/\theta_{eff})$$
$$+ 1.25 \log_{10}(t_{vis}/30) - k_m(X - 1), \qquad (6)$$

where m_{sky} is the sky brightness (AB mag arcsec^{-2}), θ_{eff} is the seeing (in arcseconds), t_{vis} is the exposure time (seconds), k is the atmospheric extinction coefficient, and X is air mass. Here the seeing corresponds to the "effective" seeing computed from the seeing FWHM following the procedure described in Angeli et al. (2016). The seeing FWHM in each band is listed in the second row of Table 2, and the effective seeing is listed in the third row of Table 2.

The constants C_m depend on the overall throughput of the instrument and are computed using our current best throughput estimates for optical elements and sensors. The values of C_m listed in Table 2 assume instrumental noise of 9 e$^-$ per pixel and per readout (whose effect on m_5 is significant only in the u band). In all six bands they imply single-visit depths m_5 (also listed in Table 2) that lie between the minimum and design specification values from the SRD listed in Table 1. The differences in performance between LSST and, for example, SDSS follow directly from these relations.[100]

The structure of Equation (6) nicely illustrates decoupling between the system sensitivity that is fully absorbed into C_m and observing conditions specified by m_{sky}, θ, t_{vis}, k_m, and X. However, this decoupling between the system sensitivity expressed via C_m and observing conditions is only correct in the limit that the instrumental noise (dominated by the readout noise) is negligible compared to the background noise. When this assumption is not correct (e.g., in the u band), the coefficients C_m do slightly depend on t_{vis}. In the limit $t_{vis} \to \infty$, the following correction needs to be added to C_m:

$$\Delta C_m^{\infty} = 1.25 \log_{10}\left[1 - \left(\frac{\text{instrumental noise}}{\text{total noise}}\right)^2\right]. \qquad (7)$$

Another meaning of ΔC_m^{∞} is the loss of depth at the nominal value of t_{vis} due to finite readout noise. The values of ΔC_m^{∞} are listed in Table 2. To predict 5σ depths for an exposure time a factor of τ longer than the fiducial $t_{vis} = 30$ s, the following

---

[99] Equation (5) can be derived from $\sigma_{rand} = N/S$, where N is noise and S is signal, and by assuming that $N^2 = N_o^2 + \alpha S$. The constants N_o and α can be expressed in terms of a single unknown constant γ by using the condition that $\sigma_{rand} = 0.2$ for $m = m_5$.
[100] SDSS data typically reach a 5σ depth for point sources of $r = 22.5$ with an effective aperture of $D = 2.22$ m, an exposure time of $t_{vis} = 54$ s, the median r-band sky brightness of $r_{sky} = 20.9$ mag arcsec^{-2}, the median seeing of $\theta = 1''.5$, and the median air mass of $X = 1.3$. In comparison, the LSST loses 0.32 mag in depth due to shorter exposures and gains 1.17 mag due to larger aperture, 0.83 mag due to better seeing, and 0.20 mag due to fainter sky, for a net gain of ~1.9 mag.
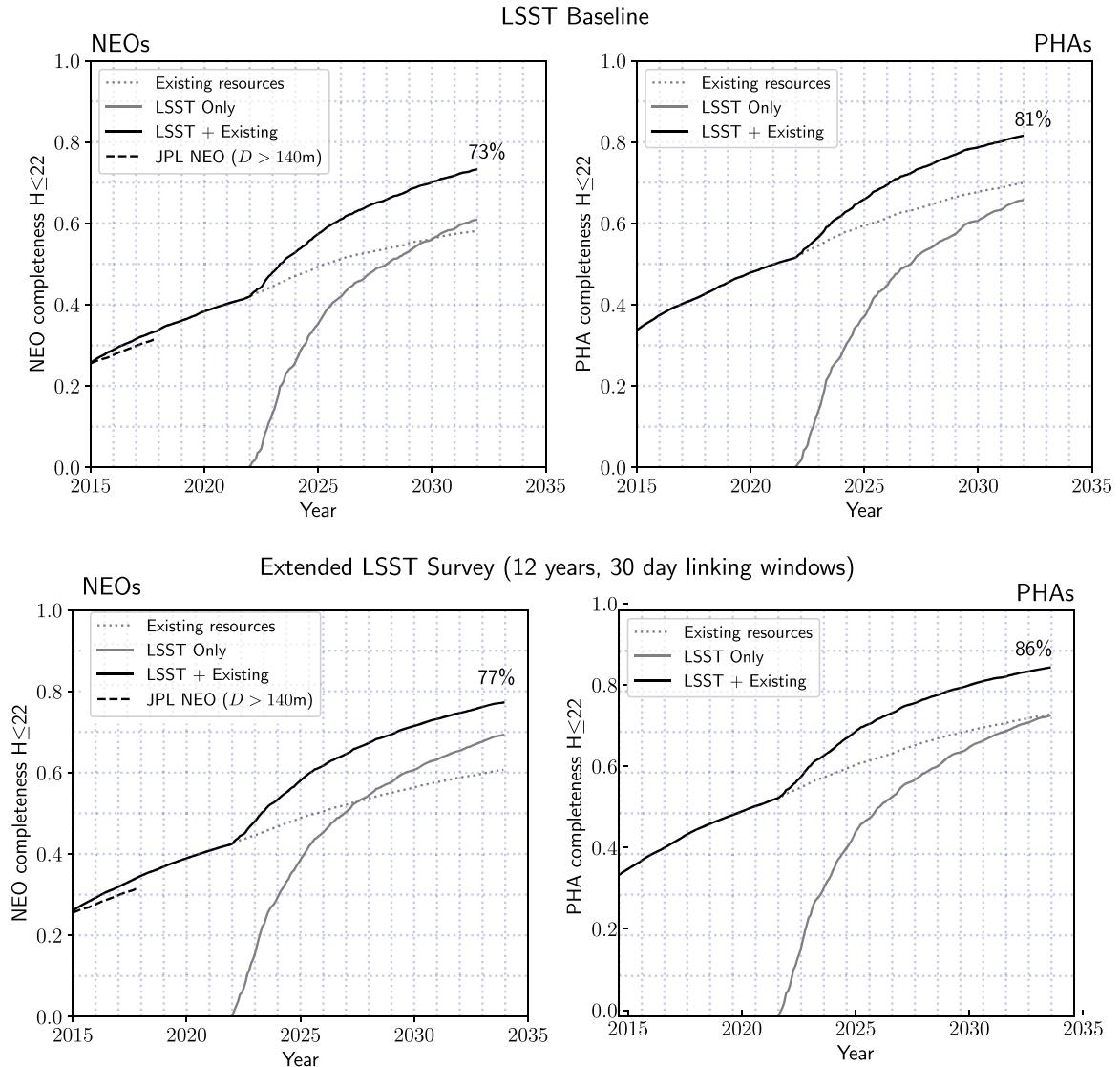
Figure 20. Cumulative completeness of the LSST survey for NEOs (left panels) and PHAs (right panels) brighter than a given absolute magnitude, $H \leqslant 22$ (related to the size of the object and albedo; $H = 22$ mag is equivalent to a typical 140 m asteroid). The top panels illustrate cumulative completeness for the LSST baseline cadence and MOPS configuration. In the baseline, LSST alone would discover 66% of the PHAs with $H \leqslant 22$ (61% of NEOs); LSST combined with current and ongoing surveys can discover 81% of PHAs (73% of NEOs). The bottom panels illustrate cumulative completeness when LSST is operated for 12 yr, with extra visits around the ecliptic, and when the MOPS linking window is increased to 30 days from the baseline 15. In this case, LSST alone could discover 74% of the PHAs with $H \leqslant 22$ (69% of NEOs); LSST combined with existing resources could discover 86% of PHAs (77% of NEOs).

correction should be added to the values of C_m listed in Table 2:

$$\Delta C_m(\tau) = \Delta C_m^{\infty} - 1.25 \log_{10}\left[1 + \frac{10^{(0.8\,\Delta C_m^{\infty})} - 1}{\tau}\right]. \quad (8)$$

By definition, $\Delta C_m(\tau = 1) = 0$. Again, this effect is only substantial in the u band, as demonstrated by the values of $\Delta C_m(\tau = 2)$ listed in Table 2.

The loss of depth at the air mass of $X = 1.2$ due to seeing degradation and increased atmospheric extinction is listed in the last row in Table 2. Note that the limiting depth predictions are uncertain by about 0.1–0.2 mag, due to unpredictable solar activity (which influences the night sky brightness; Patat 2008).

3.2.2. The NEO Completeness Analysis

Detailed analyses of the LSST completeness for PHAs and NEOs are described in Jones et al. (2018), Vereš & Chesley (2017a, 2017b), and Grav et al. (2016). After accounting for differences in their input assumptions and models, each of these independent works calculates a completeness value that is consistent within a few percent. Here we briefly summarize the LSST project analysis carried out in Jones et al. (2018); this approach is roughly the same for each of the studies mentioned above.

To assess the LSST completeness for PHAs, the PHA population is represented by a sample of orbits taken from the solar system model of Grav et al. (2007). The simulated baseline survey is used to determine which PHAs are present in each exposure and at what S/N they were observed. In addition to seeing, atmospheric transparency, and sky background effects (see Equation (6)), the S/N computation takes into account losses due to nonoptimal detection filters and object trailing. Using mean asteroid reflectance spectra (DeMeo et al. 2009), combined with the LSST bandpasses, we calculate expected magnitudes and colors, assuming that all PHAs are C-type asteroids, of $V - m = (-1.53, -0.28, 0.18, 0.29, 0.30,$

Table 3
The Expected Proper Motion, Parallax, and Accuracy for a 10 yr Long Baseline Survey

r (mag)	σ_{xy} [a] (mas)	σ_π [b] (mas)	σ_μ [c] (mas yr^{-1})	σ_1 [d] (mag)	σ_C [e] (mag)
21	11	0.6	0.2	0.01	0.005
22	15	0.8	0.3	0.02	0.005
23	31	1.3	0.5	0.04	0.006
24	74	2.9	1.0	0.10	0.009

Notes.
[a] Typical astrometric accuracy (rms per coordinate per visit).
[b] Parallax accuracy for 10 yr long survey.
[c] Proper-motion accuracy for 10 yr long survey.
[d] Photometric error for a single visit (two 15 s exposures).
[e] Photometric error for co-added observations (see Table 1).

0.30) for $m = (u, g, r, i, z, y)$ to transform standard V-band magnitudes to the magnitudes expected in each filter (Ivezić et al. 2001). Due to very red $V - u$ colors and the relatively bright limiting magnitude in the y band, the smallest objects are preferentially detected in the $griz$ bands. The correction for trailing is implemented by subtracting from the right-hand side of Equation (6),

$$\Delta m_5^{\text{trailing}} = 1.25 \log_{10}(1 + 0.42\, x^2) \qquad (9)$$

$$x = \frac{v\, t_{\text{vis}}}{24\, \theta}, \qquad (10)$$

where the object's velocity, v, is expressed in deg day^{-1} (see Section 5.1.4 in Jones et al. 2018). For the nominal exposure time of 30 s and $\theta = 0\rlap{.}''7$, the loss of limiting magnitude is 0.04 mag for $v = 0\rlap{.}^\circ 25$ day^{-1}, typical for objects in the main asteroid belt, and 0.46 mag for $v = 1\rlap{.}^\circ 0$ day^{-1}, typical of PHAs passing near Earth. PHAs are characterized by their "absolute magnitude" H, i.e., their apparent magnitude if they were placed 1 au from both the Sun and the Earth, with a phase angle of $0°$. For a given albedo and spherical asteroids, H depends only on the asteroid diameter. The PHA orbits are cloned over an H magnitude distribution with $dN/dH = 10^{\alpha H}$, with $\alpha = 0.33$, in order to evaluate completeness as a function of H (this magnitude distribution corresponds to a differential size distribution $dN/dD \propto 1/D^\beta$, with $\beta = 5\alpha + 1$).

An object is considered to be discovered if the object was detected on at least three nights within a window of 15 days, with a minimum of two visits per night. The same criterion has been used in NASA studies and is confirmed as reliable by a detailed analysis of orbital linking and orbit determination using the Moving Object Processing System (MOPS) code (Jedicke et al. 2005; Vereš & Chesley 2017a, 2017b) developed by the Pan-STARRS project (and adopted by LSST in a collaborative effort with Pan-STARRS). The MOPS software system and its algorithms are significantly more advanced than anything previously fielded for this purpose to date. Realistic MOPS simulations show >99% linking efficiency across all classes of solar system objects (Denneau et al. 2013), and at least 93% efficiency for NEOs (Vereš & Chesley 2017a, 2017b).

The LSST baseline cadence discovers 66% of PHAs and 61% of NEOs with $H \leqslant 22$ (equivalent[101] to $D \geqslant 140$ m) after 10 yr of operations (Jones et al. 2018). This cadence spends 6% of the total observing time on NEO-optimized observations north of $\delta = +5°$, and MOPS links objects with windows of 15 days. The baseline survey cumulative completeness as a function of time for objects with $H \leqslant 22$ is shown in the top panel of Figure 20, both with and without including contributions from current and ongoing surveys. These figures are likely to be uncertain at the level of $\pm 5\%$, due to uncertainties in the orbital distribution of the true population, the size distribution, uncertain distributions of shape (and thus light-curve variations), and surface properties (thus colors and albedo), plus variations in survey cadence due to weather, etc.

Various adjustments to the baseline cadence and MOPS can boost the completeness for $H \leqslant 22$ PHAs. By improving MOPS and increasing the MOPS linking window from 15 to 30 days, we can boost completeness by about 3%. By running the survey for an additional 2 yr, we can boost completeness by another 4%. Considering this "extended" LSST in the context of existing/ongoing surveys would result in a system-wide cumulative completeness of 86% for PHAs (77% for NEOs), approaching the 90% required by the congressional mandate (see bottom panels of Figure 20).

3.2.3. The Expected Accuracy of Trigonometric Parallax and Proper-motion Measurements

To model the astrometric errors, we need to consider both random and systematic effects. Random astrometric errors per visit for a given star are modeled as $\theta/\text{S/N}$, with $\theta = 700$ mas and S/N determined using Equation (6). Systematic errors of 10 mas are added in quadrature and are assumed to be uncorrelated between different observations of a given object. Systematic and random errors become similar at about $r = 22$, and there are about 100 stars per LSST sensor (0.05 deg^2) to this depth (and fainter than the LSST saturation limit at $r \sim 16$) even at the Galactic poles.

HSC data from the Subaru telescope reduced with the LSST software stack indicate that systematic errors of 10 mas on spatial scales of several arcminutes are realistic even at this stage of maturity of the code; results reported by DES (Bernstein et al. 2017) indicate astrometric residuals of ~ 7 mas for 30 s exposures in a 4 m, with scope for further improvements from denser astrometric standard grids. Even a drift-scanning survey such as SDSS delivers uncorrelated systematic errors (dominated by seeing effects) at the level of 20–30 mas (measured from repeated scans; Pier et al. 2003); the expected image quality for LSST will be twice as good as for SDSS. Furthermore, there are close to 1000 galaxies per sensor with $r < 22$, which will provide exquisite control of systematic astrometric errors as a function of magnitude, color, and other parameters and thus enable absolute proper-motion measurements.

Given the observing sequence for each sky position in the main survey as produced by the Operations Simulator (Section 2.7.1), we generate a time sequence of mock astrometric measurements, with random and statistical errors

---

[101] It is customary to interpret an asteroid diameter of 140 m as corresponding to an absolute magnitude of $H = 22$, which implies a visual albedo of 0.142 for all objects. A more realistic treatment of the albedo distribution can lead to a decrease in completeness on the order of 5% (Grav et al. 2016; Wright et al. 2016).

modeled as described above. The astrometric transformations for a given CCD and exposure, and proper-motion and parallax for all the stars from a given CCD, are simultaneously solved for using an iterative algorithm. The astrometric transformations from pixel to sky coordinates are modeled using low-order polynomials and standard techniques developed at the US Naval Observatory (Monet et al. 2003). The expected proper-motion and parallax errors for a 10 yr long baseline survey, as a function of apparent magnitude, are summarized in Table 3. Blue stars (e.g., F/G stars) fainter than $r \sim 23$ will have about 50% larger proper-motion and parallax errors than given in the table, due to decreased numbers of z- and y-band detections. The impact on red stars is smaller, due to a relatively small number of observations in the u and g bands, but extremely red objects, such as L and T dwarfs, will definitely have larger errors, depending on details of their SEDs. After the first 3 yr of the survey, the proper-motion errors will be about five times as large, and parallax errors will be about twice as large, as the values given in Table 3; the errors scale as $t^{-3/2}$ and $t^{-1/2}$, respectively. This error behavior is a strong independent argument for a survey lifetime of at least 10 yr (see Section 2).

For comparison with Table 3, the SDSS-POSS proper-motion measurements have an accuracy of $\sim 5\,\mathrm{mas\,yr^{-1}}$ per coordinate at $r = 20$ (Munn et al. 2004), and *Gaia* DR 2 has delivered a median uncertainty in parallax of 0.7 mas and in proper motion of $1.2\,\mathrm{mas\,yr^{-1}}$ at its faint end, approximately corresponding to $r = 20$ (Gaia Collaboration et al. 2018; Lindegren et al. 2018). Hence, LSST will smoothly extend *Gaia*'s error versus magnitude curve about 4 mag fainter (for illustration, see Figure 21 in Ivezić et al. 2012).

3.3. Data Products and Archive Services

Data collected by the LSST telescope and camera will be automatically processed to *data products*—catalogs, alerts, and reduced images—by the LSST Data Management system (Section 2.6.3). These products are designed to enable a large majority of LSST science cases, without the need to work directly with the raw pixels. We give a high-level overview of the LSST data products here; further details may be found in the LSST Data Products Definition Document (Jurić et al. 2017b).

Two major categories of data products will be produced and delivered by LSST DM:

1. Prompt products,[102] designed to support the discovery, characterization, and rapid follow-up of time-dependent phenomena ("transient science"). These will be generated continuously every observing night, by detecting and characterizing sources in images differenced against deep templates. They will include alerts to objects that were newly discovered or have changed brightness or position at a statistically significant level. The alerts to such events will be published within 60 s of observation; we expect several million alerts per night (Ridgway et al. 2014).

   In addition to transient science, the prompt products will support discovery and follow-up of objects in the solar system. Objects with motions sufficient to cause trailing in a single exposure will be identified and flagged as such when the alerts are broadcast. Those that are not trailed will be identified and linked based on their motion from observation to observation, over a period of a few days. Their orbits as derived by MOPS will be published within 24 hr of identification. The efficiency of linking (and thus the completeness of the resulting orbit catalog) will depend on the final observing cadence chosen for LSST, as well as the performance of the linking algorithm (Section 3.2.2).

2. DR products[103] are designed to enable systematics- and flux-limited science and will be made available in annual DRs.[104] These will include the (reduced and raw) single-epoch images, deep co-adds of the observed sky, catalogs of objects detected in LSST data, catalogs of sources (the detections and measurements of objects on individual visits), and catalogs of "forced sources" (measurements of flux on individual visits at locations where objects were detected by LSST or other surveys). LSST DRs will also include fully reprocessed prompt products, as well as all metadata and software necessary for the end user to reproduce any aspect of LSST DR processing.

   A noteworthy aspect of LSST DR processing is that it will largely rely on multi-epoch model fitting, or *MultiFit*, to perform near-optimal characterization of object properties. That is, while the co-adds will be used to perform object *detection*, the *measurement* of their properties will be performed by simultaneously fitting (PSF-convolved) models to all single-epoch observations. It is not yet clear to what extent we will be able to make some of these measurements on suitable linear combinations of input images (with careful propagation of PSFs and noise). An extended source model—a constrained linear combination of two Sérsic profiles—and a point-source model with proper motion—will generally be fitted to each detected object.[105]

   Second, for the extended source model fits, the LSST will characterize and store the shape of the associated likelihood surface (and the posterior), and not just the maximum likelihood values and covariances. The characterization will be accomplished by sampling, with up to ~ 200 (independent) likelihood samples retained for each object. For storage cost reasons, these samples may be retained only for those bands of greatest interest for WL studies.

As described in Section 3.1.2, approximately 10% of the observing time will be devoted to mini-surveys that do not follow the LSST baseline cadence. The data products for these programs will be generated using the same processing system and will be released on the same timescale as the rest of the survey; any specialized processing that these require will be the responsibility of the community.

While a large majority of science cases will be adequately served by prompt and DR products, more specialized investigations may benefit from custom, user-created products derived from the LSST data. These could be new catalogs

---

[102] Historically, these have been referred to as "Level 1 Data Products," but going forward we prefer to use the more descriptive *Prompt Products* designation. Note that the old terminology is still in use in present-day LSST documents and code; new and updated documents will gradually transition to the new, descriptive nomenclature used in this paper.

[103] These have been referred to as "Level 2 Data Products" in the past; as with their "Level 1" counterparts, we will use the more descriptive nomenclature going forward.

[104] The first-year data will probably be split into two DRs.

[105] For performance reasons, it is likely that only the point-source model will be fitted in the most crowded regions of the Galactic plane.

created by simple post-processing of the LSST DR catalogs, entirely new data products generated by running custom code on raw LSST imaging data, or something in between. We will make it possible for the end users to create (or use) such user-generated[106] products at the LSST Data Facility, using the services offered within the LSST Science Platform (Section 3.3.1).

3.3.1. The LSST Science Platform

The LSST Science Platform (Jurić et al. 2017) represents LSST's vision for a large-scale astronomical data archive that can enable effective research with data sets of LSST size and complexity. It builds on recent trends in remote data analysis and practical experiences in the astronomical context gathered by projects such as the JHU SciServer (Raddick et al. 2017), Gaia GAVIP (Vagg et al. 2016), or NOAO Datalab (Fitzpatrick et al. 2016).

The LSST Science Platform will be a set of web applications (portals) and services through which the users will access the LSST data products and, if desired, conduct remote analyses or create user-generated products. The platform makes this possible through three user-facing *aspects*:

1. The web Portal, designed to provide the essential data access and visualization services through a simple-to-use website. It will enable querying and browsing of the available data sets in ways the users are accustomed to at archives such as IRSA, MAST, or the SDSS archive.
2. The JupyterLab aspect, which will provide a Jupyter[107] Notebook-like interface and is geared toward enabling next-to-the-data remote analysis. A large suite of commonly used astronomical software, including the LSST software stack (Section 2.6.4), will be made available through this interface. The user experience will be nearly identical to working with Jupyter notebooks locally, except that computation and analysis will occur with resources provided at the LSST Data Access Center. This is an implementation of the "bringing computation to the data" paradigm: rather than imposing the burden of downloading, storing, and processing (potentially large) subsets of LSST data at their home institutions, we make it possible for the users to bring their codes and perform analyses at the LSST DAC. This reduces the barrier to entry and shortens the path to science for the LSST science community.
3. The Web API aspect will expose the LSST DAC services to other software tools and services using commonly accepted formats and protocols.[108] This interface will open the possibility for remote access and analysis of the LSST data set using applications that the users are already comfortable with such as TOPCAT (Taylor 2005), or libraries such as Astropy (Astropy Collaboration et al. 2013; Jenness et al. 2016). Furthermore, the offered APIs will allow for federation with other astronomical archives, bringing added value to the LSST data set.

---

[106] Formerly known as "Level 3 Data Products."
[107] http://jupyter.org/
[108] For example, industry-standard protocols such as WebDAV may be used to expose file data, or Virtual Observatory protocols such as TAP and SIAP may be used for access to catalogs and images, respectively.

Approximately 10% of the total budget for the LSST Data Facility compute and storage capacity has been reserved for the LSST Science Platform needs, and to be shared by all LSST DAC users. Based on the current plans and technology projections, these equate to approximately 2400 cores, 4 PB of file storage, and 3 PB of database storage at the beginning of LSST operations (in 2022).

4. Examples of LSST Science Projects

The design and optimization of the LSST system leverage its unique capability to scan a large sky area to a faint flux limit in a short amount of time. The main product of the LSST system will be a multicolor *ugrizy* image of about half the sky to unprecedented depth ($r \sim 27.5$). For a comparison, one of the best analogous contemporary data sets is that of SDSS, which provides *ugriz* images of about a quarter of the sky to $r \sim 22.5$, with twice as large seeing (see Figures 21 and 22). A major advantage of LSST is the fact that this deep sky map will be produced by taking hundreds of shorter exposures (see Table 1). Each sky position within the main survey area will be observed close to 1000 times, with timescales spanning seven orders of magnitude (from 30 s to 10 yr), and produce roughly *30 trillion photometric measures* of celestial sources.

It is not possible to predict all the science that LSST data will enable. We now briefly discuss a few projects to give a flavor of anticipated studies, organized by the four science themes that drive the LSST design (although some projects span more than one theme). For an in-depth discussion of LSST science cases, we refer the reader to the LSST Science Book, as well as more specialized documents discussing cosmology (LSST Dark Energy Science Collaboration 2012; Zhan & Tyson 2018), galaxy science (Robertson et al. 2017), and synergy with other ground-based and space-based facilities (Jain et al. 2015; Najita et al. 2016; Rhodes et al. 2017).

4.1. Probing Dark Energy and Dark Matter

A unique aspect of LSST as a probe of dark energy and dark matter is the use of multiple cross-checking probes that reach unprecedented precision (see Figure 23). Any given probe constrains degenerate combinations of cosmological parameters, and each probe is affected by different systematics; thus, the combination of probes allows systematics to be calibrated and for degeneracies to be broken. Dark energy manifests itself in two ways. The first is the relationship between redshift and distance (the Hubble diagram), or equivalently the expansion rate of the universe as a function of cosmic time. The second is the rate at which matter clusters with time. Structure formation involves a balance between gravitational attraction of matter overdensities and the rapid expansion of the background. Thus, quantifying the rate of growth of structures from early times until the present provides additional tests of the energy contents of the universe and their interactions.

The joint analysis of LSST WL and galaxy clustering is particularly powerful in constraining the dynamical behavior of dark energy, i.e., how it evolves with cosmic time or redshift (Hu & Jain 2004; Zhan 2006). By simultaneously measuring the growth of large-scale structure and luminosity and angular distances as functions of redshift (via WL, LSS, SN, and cluster counting), LSST data can reveal whether the recent cosmic acceleration is due to dark energy or modified gravity
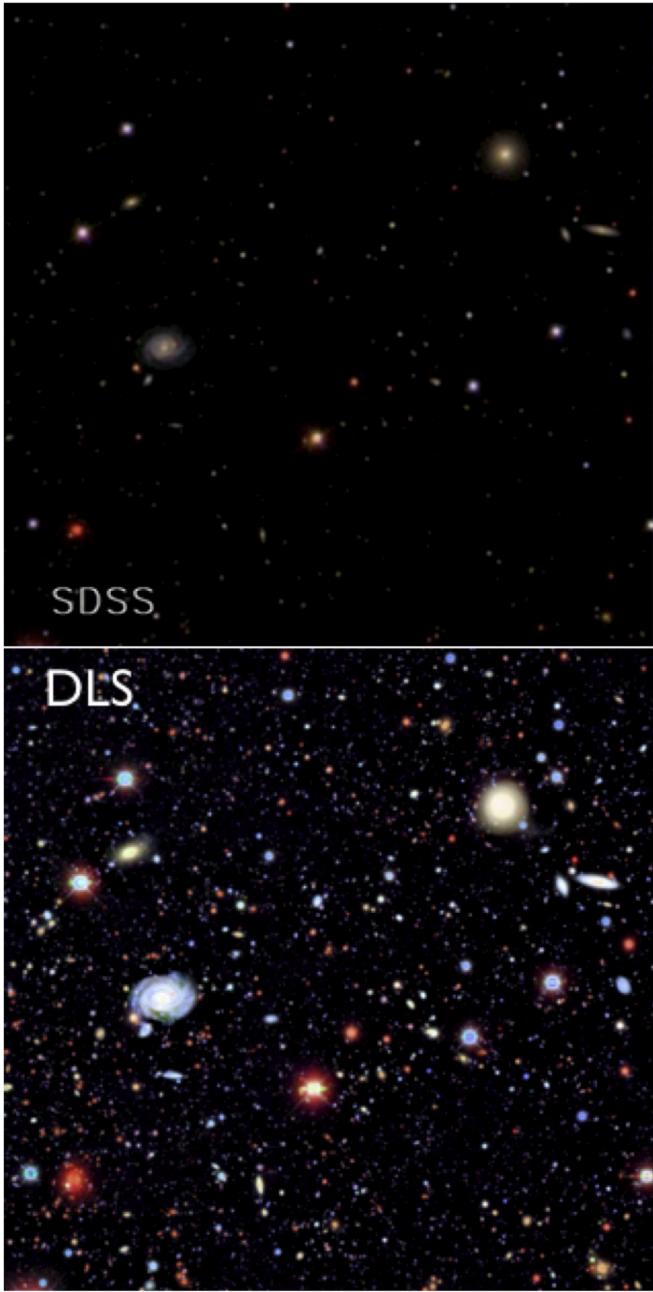
Figure 21. Comparison of ∼7.5 × 7.5 arcmin² images of the same area of sky (centered on $\alpha = 9^h\ 20'\ 47''$ and $\delta = 30°\ 8'\ 12''$) obtained by SDSS (top, $r < 22.5$) and the Deep Lens Survey (bottom, $r < 24.5$). These are gri composites, colorized following Lupton et al. (2004). The depth gain for the bottom image is mostly due to the lower surface brightness limit, which is also responsible for the apparent increase of galaxy sizes. LSST will obtain ∼100 gri color images to the same depth (∼200 for the riz composites) of each point over half the celestial sphere (18,000 deg², equivalent to 1.15 million ∼7.5 × 7.5 arcmin² regions), and with better seeing. After their co-addition, the final image will be another ∼3 mag deeper (a faint limit of $r = 27.5$ for point sources).

(Lue et al. 2004; Ishak et al. 2006; Knox et al. 2006; Jain & Zhang 2008; Oguri & Takada 2011; Jain et al. 2013; Weinberg et al. 2013). The DES (see, e.g., DES Collaboration et al. 2018, and references therein) provides a compelling proof of concept for this program.

Over a broad range of accessible redshifts, the simple linear model for the dark energy equation of state ($w = w_0 + w_a(1 - a)$) is a poor representation of more general
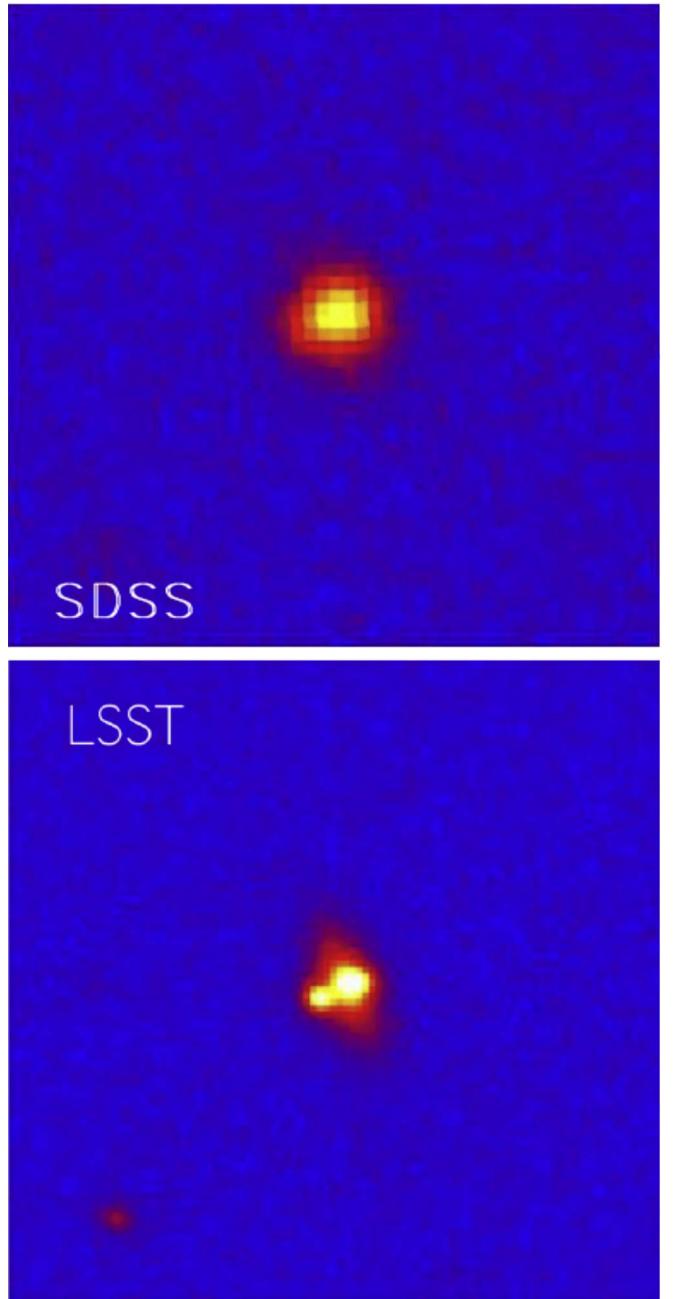
Figure 22. Comparison of angular resolution for 20 × 20 arcsec² images obtained by the SDSS (top, median seeing of $1''5$) and expected from LSST (bottom, seeing of $0''7$). The images show a lensed SDSS quasar (SDSS J1332 +0347; Morokuma et al. 2007); the bottom image was taken with Suprime-cam at Subaru. Adapted from Blandford & LSST Strong Lensing Science Collaboration (2007).

dark energy theories. Barnard et al. (2008) showed that in a high-dimensional dark energy model space, LSST data could lead to a hundred- to thousand-fold increase in precision over its precursor experiments, thereby confirming its status as a premier Stage IV experiment in the sense of Albrecht et al. (2006).

The power and accuracy of LSST dark energy and dark matter probes are a result of the enormous samples that LSST will have, including several billion galaxies and millions of SNe Ia. At $i < 25.3$ (S/N > 20 for point sources), the photometry of galaxies will be of high enough quality to
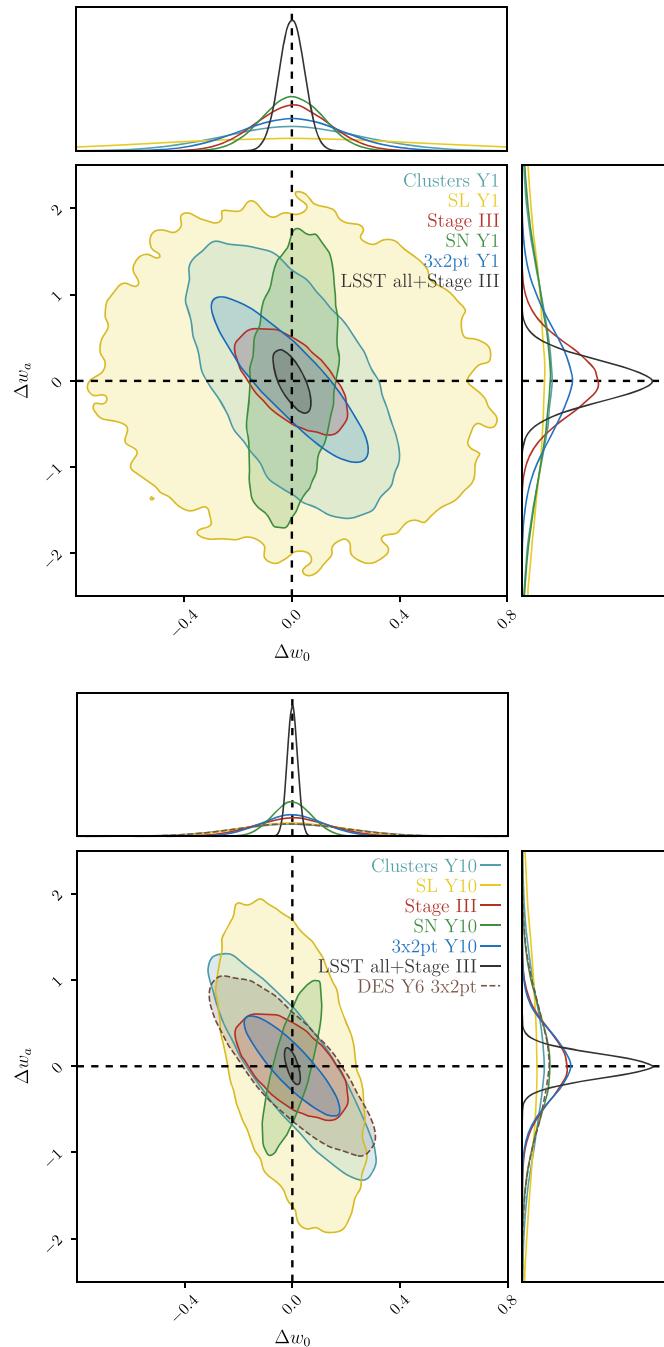
Figure 23. Constraints on the dark energy equation of state ($w = w_0 + w_a(1 - a)$) from LSST cosmological probes after 1 yr of data (Y1; top) and the full 10 yr survey (Y10; bottom), from each probe individually, and the joint forecast including "Stage III priors" (i.e., Planck, JLA SNe, and BOSS BAOs). The 68% confidence intervals are shown in all cases; the plotted quantities Δw_0 and Δw_a are the difference between w_0 and w_a and their fiducial values of -1 and 0. In the bottom panel we show, for reference, the expected constraints from the Y6 Dark Energy Survey 3x2pt analysis (brown): the corresponding LSST analysis is already expected to be higher precision than this after just 1 yr. Figures reproduced with permission from the LSST DESC Science Requirements Document v1 (LSST Dark Energy Science Collaboration et al. 2018) and related analysis.

provide photometric redshifts with an rms accuracy ($\sigma/(1 + z)$) of 2% over the range $0.3 < z < 3.0$ (only 10% of the sample will have redshift errors larger than 6%). This number represents a requirement on the accuracy of the photometry at delivering photometric redshifts given known templates for the SEDs. The degradation in photometric redshift quality associated with requiring more training data than currently exists to define the template set increases the expected $\sigma/(1 + z)$ to ~ 0.05 (e.g., Newman et al. 2015; Graham et al. 2018), which is still well within the expected range for a Stage IV dark energy experiment. The sample to $i = 25.3$ will include several billion galaxies. At a slightly brighter cut, there will be around 30 galaxies arcmin^{-2} with shapes measured well enough for WL measurements (Chang et al. 2013, 2015), with the number realized in practice being dependent on the performance of the deblending and shape measurement algorithms. The median redshift for this sample will be $z \sim 1.2$, with the third quartile at $z \sim 2$. It will be possible to further improve photometric redshift calibration by cross-correlating the photometric sample with redshift surveys of galaxies and quasars in the same fields (Newman 2008; Matthews & Newman 2010; Ménard et al. 2013; Davis et al. 2017). The *Euclid* mission's planned 6 yr survey should reach a similar galaxy density over 15,000 square degrees of sky (Laureijs et al. 2011); its space-based resolution and broadband optical and NIR filters should provide a complementary WL survey of comparable constraining power but limited by different systematics. The *WFIRST* baseline survey is expected to cover some 2000 square degrees but reach a galaxy density of 45 arcmin^{-2} (Spergel et al. 2015). We refer the reader to the papers by Jain et al. (2015) and Rhodes et al. (2017) for a discussion of the complementarity of the three surveys.

The main LSST observables in the context of dark energy and matter are described below. For more details, we refer the reader to the LSST Dark Energy Science Collaboration's SRD, from which Figure 23 was drawn (LSST Dark Energy Science Collaboration et al. 2018); see also Krause & Eifler (2017) for more details on how the forecasts were calculated.

1. The joint analysis of shear–shear, galaxy–shear, and galaxy–galaxy correlation functions has become standard in analyses of precursor data sets (e.g., DES Collaboration et al. 2018; Joudaki et al. 2018). WL and LSS are highly complementary probes, and the combination of their auto- and cross-correlations will constrain the properties of the late-time accelerated expansion while providing internal cross-checks for marginalizing over systematic uncertainties (e.g., Mandelbaum 2018). These measurements consist of the two-point auto- and cross-correlations of shear and positions for billions of galaxies across ~ 10 redshift bins. As described in the following two items, the galaxy–galaxy and galaxy–shear correlation functions provide additional probes of dark energy and dark matter.

2. The galaxy–shear correlation function probes the growth of dark matter large-scale structure and is a diagnostic of the underlying cosmology. The combination with the galaxy–velocity correlation function estimated from currently planned spectroscopic surveys could test general relativity and its variants at high redshift (Reyes et al. 2010).

3. The galaxy–galaxy correlation function is vital to constrain the galaxy bias impacting the galaxy–shear correlation and is therefore an essential component in the joint analysis of LSS and WL. In addition, the presence of BAOs in the galaxy angular correlation functions is a strong cosmological probe on its own. The sound horizon at decoupling, which is imprinted on the mass distribution

at all redshifts and calibrated with the CMB, provides a standard ruler to measure the angular diameter distance as a function of redshift (Eisenstein et al. 1998; Cooray et al. 2001; Blake & Glazebrook 2003; Hu & Haiman 2003; Linder 2003; Seo & Eisenstein 2003). LSST photo-z BAOs will achieve percent-level precision on the angular diameter distance at ∼10 redshifts logarithmically spaced between $z = 0.4$ and 3.6. The combination with CMB and WL shear yields tight constraints on the dynamical behavior of dark energy (Figure 24). In particular, high-redshift BAO data can break the degeneracy between curvature and dark energy, constraining Ω_k to within 0.001.

4. Higher-order shear and galaxy statistics and shear peak counts can improve dark energy constraints and provide self-calibration of various systematics (Takada & Jain 2004; Dolney et al. 2006; Huterer et al. 2006; Petri et al. 2016). They are also probes of both primordial non-Gaussianities and those caused by nonlinear structure.

5. Primordial non-Gaussianity is also probed by the large-scale power of any biased tracer of the matter over-densities (Dalal et al. 2008). Although measurements of the galaxy power spectrum on very large scales are challenging owing to sky systematics (Leistedt et al. 2014) and cosmic variance, the prospect of using multiple tracers of the same field could significantly improve the constraining power for this observable (Seljak 2009). Similar measurements of the large-scale power will also be used to test phenomenological models of clustering dark energy (Takada 2006).

6. Similarly, WL magnification tomography (Morrison et al. 2012) offers a complementary probe of a mix of cosmic geometry and growth of dark matter structure.

7. The two LSST observing programs are complementary in the SN samples they will provide. The main survey will obtain light curves in six bands and photometric redshifts of about 400,000 photometrically classified SNe Ia that can be used for cosmological distance measurements, with further spectroscopic follow-up of a subsample of their host galaxies. Such a sample will not only provide larger statistics for the study of the Type Ia population in the universe but also be spread across the full 18,000 deg^2 LSST main survey footprint, allowing different probes of the large-scale structure of the low-redshift universe. This sample of SNe can be used as a tracer of large-scale structure by directly probing the gravitational potential of structure through inferences of their peculiar velocities (Gordon et al. 2007; Bhattacharya et al. 2011; Howlett et al. 2017), WL of SN brightnesses (Dodelson & Vallinotto 2006; Quartin et al. 2014; Macaulay et al. 2017; Scovacricchi et al. 2017), and the local bulk flow (Riess 2000; Dai et al. 2011; Turnbull et al. 2012; Feindt et al. 2013; Huterer et al. 2015), as well as low-redshift constraints on the isotropy of the universe (Antoniou & Perivolaropoulos 2010; Campanelli et al. 2011; Colin et al. 2011; Cai et al. 2013; Javanmardi et al. 2015). The rapidly sampled Deep Drilling Fields, possibly co-added over short timescales, will yield well-sampled light curves of tens of thousands of SNe to redshifts peaking around $z \sim 0.7$ and reaching beyond a redshift of 1.0, limited by the systematics related to the limits of our astrophysical understanding of SN populations and
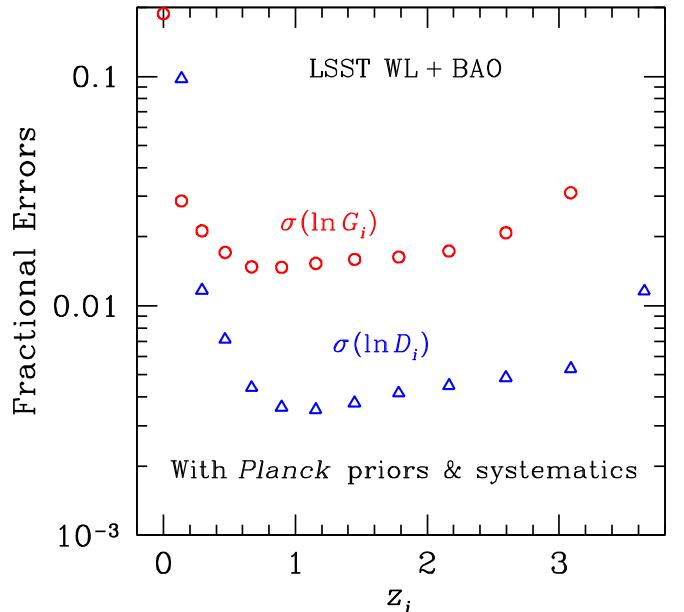
Figure 24. Marginalized 1σ errors on the comoving distance (open triangles) and growth factor (open circles) parameters from the joint analysis of LSST LSS and WL (galaxy–galaxy, galaxy–shear, and shear–shear power spectra) with a conservative level of systematic uncertainties in the photometric redshift error distribution and additive and multiplicative errors in the shear and galaxy power spectra. The maximum multipole used for WL is 2000, and that for LSS is 3000 (with the additional requirement that $\Delta_\delta^2(\ell/D_A; z) < 0.4$). The growth parameters are evenly spaced in $\log(1 + z)$ between $z = 0$ and 5, and the distance parameters start at $z_1 = 0.14$. The error of each distance (growth) parameter is marginalized over all the other parameters, including growth (distance) parameters. The joint constraints on distance are relatively insensitive to the assumed systematics (Zhan et al. 2009).

relative photometric calibration. In addition to the usual use of SNe Ia to probe the redshift–distance relation to high redshift, the luminosities will be magnified by lensing from foreground structure, a correlation that can be probed with these data. The ultimate promise of such SN surveys will be linked to the observing strategy employed by the LSST.

8. Cosmological analyses can be carried out using SN, WL, and LSS in subsets of the LSST data in different regions of the sky, testing fundamental cosmological assumptions of homogeneity and isotropy (e.g., Zhan et al. 2009).

9. The shape of the power spectrum of dark matter fluctuations measured by LSST WL will constrain the sum of neutrino masses with an accuracy of 0.04 eV or better (Cooray 1999; Song & Knox 2004; Hannestad et al. 2006). Given the current constraints on neutrino mass mixing, this is at the level to determine whether there is an inverted neutrino mass hierarchy, a fundamental question in particle physics.

10. Tens of thousands of galaxy–galaxy lenses will provide the needed statistics to probe dark matter halo profiles and substructure (e.g., Mandelbaum et al. 2006; Vegetti et al. 2012). The image fluxes in several thousand well-measured strongly lensed quasars will enable constraints of the dark matter mass function on small scales (Dalal & Kochanek 2002).

11. The abundance of galaxy clusters as a function of mass and redshift is sensitive to cosmological parameters (SciBook, Chap. 13; von der Linden et al. 2014). LSST will produce a large catalog of clusters detected through

their member galaxy population to redshift $z \sim 1.2$. In addition, LSST will identify optical counterparts and provide deep optical imaging for clusters detected in other wavebands (e.g., Staniszewski et al. 2009).

12. The clustering properties of those same galaxy clusters will also be used to constrain cosmological parameters (Mo et al. 1996; Mana et al. 2013), to marginalize over uncertainties in the mass–observable relation and photometric redshift uncertainties (Oguri & Takada 2011), and to constrain the effects of supersample covariance in the two-point functions of WL and LSS (Hu & Kravtsov 2003; Takada & Spergel 2014).

13. LSST will discover several hundred galaxy clusters that produce multiple-image lenses of background objects. Cluster mass reconstruction based on the multiple image positions can probe the cluster inner mass profile and can provide a separate test of cosmology, especially in cases with strongly lensed background objects at different redshifts (Porciani & Madau 2000; Oguri & Kawano 2003).

14. Time delays of galaxy-scale lensed quasars will allow one to measure Hubble's constant (e.g., Suyu et al. 2010; Bonvin et al. 2017) in hundreds of systems; subpercent-level precision in $H(z)$ should be achievable (Coe & Moustakas 2009; Treu & Marshall 2016), providing a further independent dark energy probe. LSST will also discover between 500 and 1000 strongly lensed SNe Ia (Goldstein & Nugent 2017; Goldstein et al. 2018), which will provide hundreds of additional high-quality time delays. Time delays for quasars multiply lensed by clusters as a function of redshift are an independent test of dark energy (Kundić et al. 1997). The natural timescale (many months to years) is well matched to the LSST survey (Oguri & Marshall 2010).

15. Standard sirens are a new cosmological probe, demonstrated by the recent discovery of a binary neutron star merger by the Laser Interferometer Gravitational Wave Observatory (LIGO) with an electromagnetic counterpart (Abbott et al. 2017a), which was used to constrain the Hubble parameter to roughly 15% precision (Abbott et al. 2017b). Constraints from standard sirens are independent of the local distance ladder, with the primary uncertainties being the local velocity field and the inclination angle of the system. Assuming that the gravitational wave network is working well, Scolnic et al. (2018) estimate that LSST could find of order 70 electromagnetic counterparts to standard sirens.

4.2. Taking an Inventory of the Solar System

The small bodies of the solar system, such as main belt asteroids, the Trojan populations of the giant planets, and the KBOs, offer a unique insight into its early stages because they provide samples of the original solid materials of the solar nebula. Understanding these populations, both physically and in their number and size distribution, is a key element in testing various theories of solar system formation and evolution.

The baseline LSST cadence will result in orbital parameters for several million objects; these will be dominated by main belt asteroids, with light curves and multicolor photometry for a substantial fraction of detected objects. The LSST sample of asteroids with accurate orbits and multicolor light curves will

be 10–100 times larger than the currently available sample. LSST will make a significant contribution to the congressional target completeness of 90% for PHAs larger than 140 m (Section 3.2.2) and will detect over 30,000 TNOs brighter than $r \sim 24.5$ using its baseline cadence. LSST will be capable of detecting objects like Sedna to beyond 100 au, thus enabling in situ exploration far beyond the edge of the Kuiper Belt at $\sim$50 au. Because most of these objects will be observed several hundred times, accurate orbital elements, colors, and variability information will also be available.

The following are some examples of the LSST science opportunities in solar system science:

1. Studies of the distribution of orbital elements for over 5 million main belt asteroids as a function of color-based taxonomy (see Figure 25) and size; size distributions of asteroid families (Parker et al. 2008) and their correlations with age (Jedicke et al. 2004; Nesvorný et al. 2005); dynamical effects (Bottke et al. 2001); and studies of object shapes and spin states using light-curve inversion techniques (Pravec & Harris 2000; Durech et al. 2009).

2. Studies of transient mass loss in asteroids (active asteroids or main belt comets; Hsieh & Jewitt 2006); such objects will appear extended in the sensitive LSST images. Only a few such objects are currently known (Jewitt et al. 2011; Jewitt 2012); LSST will increase the sample of such objects to $\sim$100.

3. Studies of the distribution of orbital elements for about 100,000 NEOs as a function of color and size (Rabinowitz 1993; Dandy et al. 2003); correlations with the analogous distributions for main belt objects, and studies of object shapes and structure using light curves.

4. Studies of the distribution of orbital elements for close to 300,000 Jovian Trojan asteroids as a function of color and size (Jewitt et al. 2000; Yoshida & Nakamura 2005; Szabó et al. 2007); the search for dynamical families (Knezevic & Milani 2005); studies of shapes and structure using light curves.

5. Studies of the distribution of orbital elements for about 30,000 TNOs (see Figure 26) as a function of color and size; the search for dynamical families (Marcus et al. 2011); studies of shapes and structure using light curves (Duncan et al. 1995; Gladman et al. 2001; Trujillo et al. 2001; Bernstein et al. 2004; Elliot et al. 2005; Jones et al. 2006; Doressoundiram et al. 2007).

6. An unbiased and complete census of both Jupiter-family and Oort Cloud comets. These comets will have detailed six-band high-resolution images extending to low surface brightness, in multiple points through their orbits, allowing detailed studies of activity as a function of distance from the Sun (Lowry et al. 1999; A'Hearn 2004). LSST will discover an unprecedentedly large number of comets, with typically 50 observations per object spread throughout their orbits during the 10 yr survey, and will help us to constrain models of the origin of comets (Solontoi 2010; Silsbee & Tremaine 2016). Combining the CN production rates determined from observations in the u bandpass, as a proxy for overall gas activity, with the nonvolatile production rate calculated from the continuum-sensitive r, i, and z bands allows for the determination of the gas-to-dust ratio. The relationship between the gas-to-dust ratio in comets and their dynamical class (and places of formation) is a
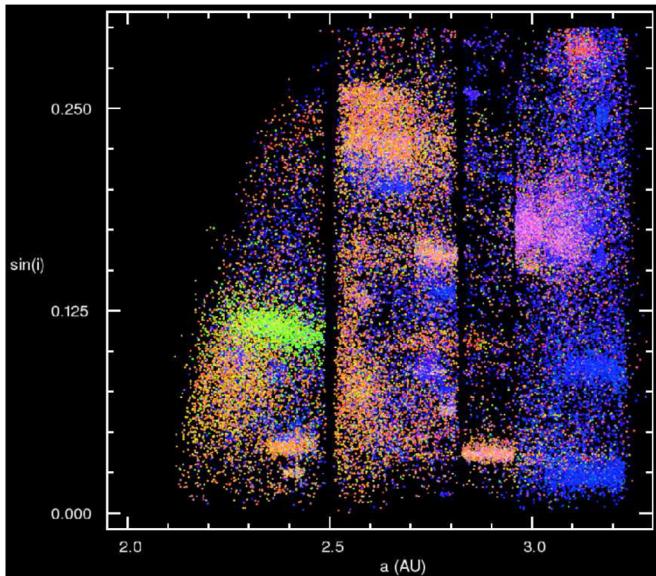
Figure 25. Example of color-based asteroid taxonomy. The figure shows the distribution of asteroids in the proper semimajor axis vs. sin(i) plane for 45,000 asteroids with colors measured by SDSS (Parker et al. 2008). The color of each dot is representative of the object's color. Note the strong correlation between asteroid families (objects with similar orbital elements) and colors. There are at least five different taxonomic types distinguishable with SDSS measurements; LSST color measurements of asteroids will be at least as accurate as SDSS measurements shown here and will increase the number of objects by roughly two orders of magnitude.
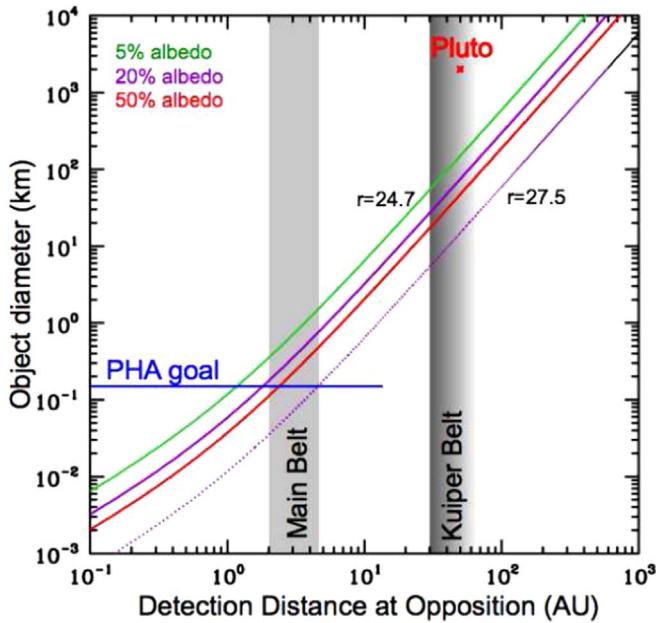
Figure 26. LSST detection limits for distant solar system objects as a function of distance. Moving objects with diameters as small as 100 m in the main asteroid belt and 100 km in the Kuiper Belt (TNOs) will be detected in individual visits, depending on the albedo. Specialized deeper observations (see Section 3.1.2) will detect TNOs as small as 10 km. Adapted from Jones et al. (2007).

fundamental, and still unresolved, question in cometary science (see, e.g., A'Hearn et al. 1995; Bockelée-Morvan & Biver 2017).

7. Searching for objects with perihelia out to several hundred astronomical units. For example, an object like

Sedna (Brown et al. 2004) would be detectable at 130 au. This will result in a much larger, well-understood sample of inner Oort Cloud objects like Sedna and 2012 VP113 (Trujillo & Sheppard 2014). Studying the distribution of their orbits (in particular including any clustering in the argument of perihelion) will test models predicting the existence of a planetary-mass object beyond Neptune, a proposed Planet 9 (Trujillo & Sheppard 2014; Batygin & Brown 2016; Brown & Batygin 2016; Sheppard & Trujillo 2016; Brown 2017). Depending on the proposed Planet 9's on-sky location and brightness, it may be possible for LSST to directly detect it in the wide survey images (Batygin & Brown 2016; Brown & Batygin 2016; Sheppard & Trujillo 2016; Brown 2017).

8. Mapping the propagation of coronal mass ejections through the solar system using induced activity in a large sample of comets at different heliocentric distances (SciBook, Chap. 5).

9. Probing the inventory and frequency of interstellar asteroids/comets. The recent Pan-STARRS1 discovery of the interstellar object 1I/2017 U1 ('Oumuamua) (Bacci et al. 2017) has shown the power of large, complete all-sky surveys to unearth rare and exciting classes of objects. LSST will be some 3 mag more sensitive than current NEO surveys (like Pan-STARRS1) and will cover more sky more often. Therefore, LSST is likely to find more interstellar objects, and more frequently. Estimates from Cook et al. (2016), Engelhardt et al. (2017), and Trilling et al. (2017) suggest that LSST will increase the number of such rare objects by an order of magnitude, which, among other outcomes, will help constrain the frequency and properties of planetary system formation in the solar neighborhood.

4.3. Exploring the Transient Optical Sky

Time domain science will greatly benefit from LSST's unique capability to simultaneously provide large-area coverage, dense temporal coverage, accurate color information, good image quality, and rapid data reduction and classification. Since LSST extends time–volume–color space 50–100 times over current surveys (e.g., Djorgovski et al. 2013), it will facilitate new population and statistical studies and also the discovery of new classes of objects. LSST data products will enable many projects, including:

1. Discovery and characterization of thousands of hot Jupiters in exoplanetary systems via the transit method (Wright et al. 2012). LSST will extend the extrasolar planet census to larger distances within the Galaxy, thus enabling detailed studies of planet frequency as a function of stellar metallicity and parent population (e.g., Hartman et al. 2009; Bayliss & Sackett 2011). The out-of-transit variability of exoplanet host stars will also provide characterization of the system via flaring behavior and stellar age via gyrochronology, the latter helping constrain theories of tidal evolution and migration in giant planets.

2. Gravitational microlensing in the Milky Way (see Han 2008), as well as in the Local Group and beyond (de Jong et al. 2008).

3. Studies of dwarf novae, including their use as probes of stellar populations and structure in the Local Group

(Neill & Shara 2005; Shara 2006; Shen & Bildsten 2009); population studies of the end points of binary evolution, mapping the distribution and quantifying the demographics of long and short orbital period dwarf novae, and distinguishing recurrent from normal novae. Regular-cadence, long-term color observation on a large sample of galactic sources will enable the identification of CVs containing highly magnetic white dwarfs, which are red due to cyclotron emission from the magnetic accretion column and in the low state for the majority of the 10 yr survey.

4. Studies of transients from poorly constrained stages of stellar evolution including stellar eruptions, LBVs, stellar mergers, and helium core flashes leading to white dwarf formation. We will be able to identify the progenitors of eruptive transients in the deep LSST stacks and even look for faint precursor eruptions. We will also constrain the rates of individual eruption subclasses (Smith 2014) by detecting them in galaxies out to tens of megaparsecs.

5. A census of light echoes of historical explosive and eruptive transients in the Milky Way and Local Group through high-resolution time series.

6. Studies of known and unusual SN populations and parameterization of their light curves (e.g., Höflich et al. 1998; Wang et al. 2003; Howell et al. 2007; Kowalski et al. 2008; Hicken et al. 2009; Foley 2012; Bianco et al. 2014; Arcavi et al. 2017), including late-time observations of rapidly evolving transients to deep limits, critical for ascertaining their nature. Measurements of intrinsic rates for both peculiar transients (e.g., Drout et al. 2014) and SNe as a function of subtype and host environment properties (e.g., metallicity; Graur et al. 2017).

7. A deep search for new populations of novae and SN progenitors (Smartt 2009; Thompson et al. 2009; Smith et al. 2011, see Figure 27), both through direct imaging and through the detection of SN precursor events (Ofek et al. 2013); characterization of pre-SN variability of SN progenitors and the frequency of pre-SN outbursts.

8. The discovery of strongly lensed SNe; 500–1000 multiply imaged SNe Ia (Goldstein & Nugent 2017; Goldstein et al. 2018) and at least several hundred strongly lensed core-collapse SNe (Oguri & Marshall 2010) are expected to be discovered by LSST. Time delays between the multiple images of strongly lensed core-collapse SNe can be used to observe the elusive shock breakout phase of the light curve, providing an unprecedented look at the earliest emission from these transients (Suwa 2018).

9. A large, well-characterized sample of superluminous SNe, including objects at redshift as high as $z = 2.5$, a sample large enough to be leveraged for cosmology improving constraints on w and Ω_m (Scovacricchi et al. 2016).

10. Studies of optical bursters (those varying faster than 1 mag hr^{-1}) to $r \sim 25$ mag.

11. Detection and measurement of gamma-ray burst afterglows and transients (e.g., Zhang & Mészáros 2004; Zhang et al. 2006; Kann et al. 2010) to high redshift ($\sim$7.5).

12. Large-scale studies of stellar tidal disruptions by nuclear supermassive black holes (e.g., Evans & Kochanek 1989; Gezari et al. 2008; Strubbe & Quataert 2009; Bloom et al. 2011; Gezari 2012; Komossa 2015), as well as binary
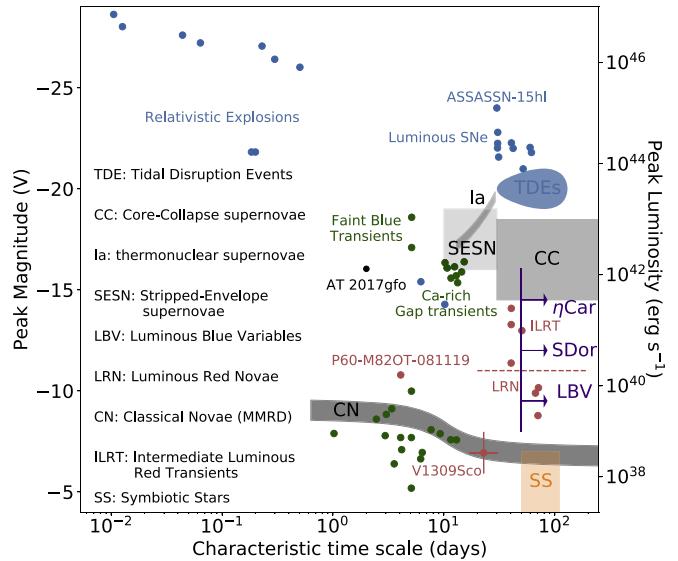
Figure 27. Phase space of cosmic explosive and eruptive transients as represented by their absolute *V*-band peak brightness and the event timescale, defined as the time taken to drop 1 mag in *V*-band brightness from peak luminosity (adapted from Kulkarni et al. 2007 and Kasliwal 2011). The locus of the classical novae is as described in della Valle & Livio (1995). LSST will open up large regions of this phase space for systematic exploration by extending time–volume space more than 100 times over existing surveys.

supermassive black holes in the in-spiral phase (e.g., Cuadra et al. 2009; Coughlin et al. 2017a). Persistent observations leading to complete light curves (other than the seasonal gaps) of long-duration events like TDEs. Measurements of rates as a function of galaxy type, redshift, and level of nuclear activity. An assessment of the diversity of these events in terms of total power, effective temperature, and jet launching efficiency.

13. A study of quasar variability using accurate, multicolor light curves for a few million quasars, leading to constraints on the accretion physics and nuclear environments (de Vries et al. 2003; Vanden Berk et al. 2004; MacLeod et al. 2010; Jiang et al. 2017). Relations between quasar variability properties and luminosity, redshift, rest-frame wavelength, timescale, color, radio-jet emission, black hole mass, and Eddington-normalized luminosity will be defined with massive statistics, including the potential to detect rare but important events such as jet flares and obscuration events. Microlensing events will also be monitored in the $\sim$4000 gravitationally lensed quasars discovered by LSST and used to measure the spatial structure of quasar accretion disks.

14. The superb continuum light curves of AGNs will enable economical "piggyback" reverberation-mapping efforts using spectroscopy of emission lines (e.g., Chelouche & Daniel 2012; Shen et al. 2015; Grier et al. 2017). These results will greatly broaden the luminosity–redshift plane of reverberation-mapped AGNs with black hole mass estimates. For LSST data alone, the interband continuum lags will provide useful structural information.

15. Optical identification of transients and variables detected in other electromagnetic wavebands, from gamma-rays to radio. Examples include optical and gamma-ray variability in blazars (Hovatta et al. 2014), radio transients associated with tidal disruption flares (Giannios & Metzger 2011), and radio counterparts to SNe and GRBs

(Gal-Yam et al. 2006). Deep optical observations with LSST may also help illuminate the nature of fast radio bursts (FRBs; Lorimer et al. 2007; Thornton et al. 2013).

16. Optical identification of counterparts to non-electromagnetic sources, such as gravitational waves (GWs) and neutrino events (LIGO,[109] ICECUBE[110]). LSST's unique ability to characterize the faint variable sky over large areas will be important for the detection of GW associated sources, with an estimate of $\sim$7 discoveries per year (Scolnic et al. 2018). The power of the Advanced LIGO (aLIGO)/Virgo[111] experiment has led to the discovery of four GW events in less than a year. The binary neutron star merger event GW170817 was accompanied by emission detected across the entire electromagnetic spectrum (Abbott et al. 2017a). The optical/NIR emission had two distinct components, a blue emission (which peaked and then faded away on a timescale of a few days) and a redder component that persisted for $\sim$15 days. This longer-lasting component arose from the radioactive decay of heavy elements synthesized during the NS merger, a "kilonova" (AT 2017gfo). While both of these components had been predicted (Metzger 2017), the $\sim$100-kilonova sample that LSST is expected to generate will enable comparative studies of these transients, allowing us to understand how the presence and relative luminosity of the two components varies with the properties of the binary system (e.g., mass) and its remnant. Furthermore, LSST will be important for identifying the optical transient corresponding to LIGO events in the first place, eliminating false positives (Metzger & Berger 2012; Nissanke et al. 2013; Cowperthwaite & Berger 2015; Coughlin et al. 2017b). At 24th magnitude, rejecting thousands of false positives from other new transients appearing during the imaging of the GW event area requires a strategy of multiple passes in different filters.

4.4. Mapping the Milky Way

The LSST will map the Galaxy in unprecedented detail, and by doing so revolutionize the fields of Galactic astronomy and near-field cosmology. The great detail with which the Milky Way can be studied complements the statistical power of extragalactic observations. The overarching goal of near-field cosmology is to use spatial, kinematic, and chemical measurements of stars to reveal the structure and evolution history of the Milky Way and its environment. LSST will reveal this fossil record in great detail and provide a Rosetta stone for extragalactic astronomy by setting the context within which we interpret these broader data sets. Moreover, different candidate supersymmetric particle dark matter models predict different mass clustering on small scales, and thus different mass functions for subhalos of the Milky Way. Thus, the LSST census of faint satellites and stellar streams in the halo will offer a unique means to constrain the particle nature of dark matter.

The LSST will produce a massive and exquisitely accurate photometric and astrometric data set for about 20 billion Milky
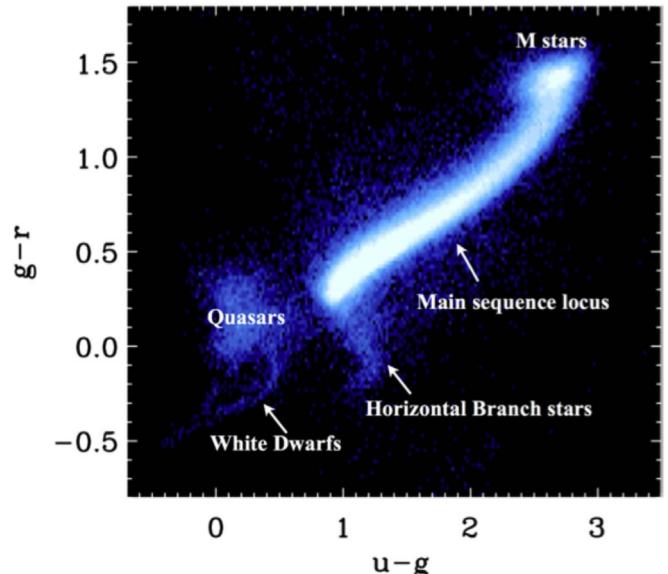
Figure 28. The $g - r$ vs. $u - g$ color–color diagram for about 1 million point sources from the SDSS Stripe 82 area. Accurate multicolor photometry contains information that can be used for source classification and determination of detailed stellar properties such as effective temperature and metallicity. LSST will enable such measurements for billions of stars.

Way stars. The coverage of the Galactic plane will yield data for numerous star-forming regions, and the y-band data will penetrate through the interstellar dust layer. Photometric metallicity measurements (see Figures 28 and 29) will be available for about 200 million main-sequence F/G stars, which will sample the halo to distances of 100 kpc (Ivezić et al. 2008; An et al. 2013) over a solid angle of roughly 20,000 deg^2. No other existing or planned survey will provide such a powerful data set to study the outer halo: Gaia is flux limited at $r = 20$, and the DES (Rossetto et al. 2011) and Pan-STARRS both lack observations in the u band, necessary for estimating metallicity. The LSST in its standard surveying mode will be able to detect RR Lyrae variables (pulsating stars and standard candles) and classical novae (exploding stars and standard candles) at a distance of 400 kpc and hence explore the extent and structure of our halo out to half the distance to the Andromeda galaxy. Thus, the LSST will enable studies of the distribution of main-sequence stars beyond the presumed edge of the Galaxy's halo (see Figure 30), of their metallicity distribution throughout most of the halo, and of their kinematics beyond the thick-disk/ halo boundary. LSST will also obtain direct distance measurements via trigonometric parallax below the hydrogen-burning limit for a representative thin-disk sample.

In addition to the study of hydrogen-burning stars, LSST will uncover the largest sample of stellar remnants to date. Over 97% of all stars eventually exhaust their fuel and cool to become white dwarfs. Given the age of the Galactic halo, a significant fraction of the mass in this component may reside in these remnant stars (e.g., Alcock et al. 2000; Tisserand et al. 2007), and therefore their discovery directly constrains the Galactic mass budget. These large populations of disk and halo white dwarfs will provide unprecedented constraints on the luminosity function of these stars, which will directly yield independent ages for the Galactic disk and halo (e.g., through the initial–final mass relation; Kalirai et al. 2008).
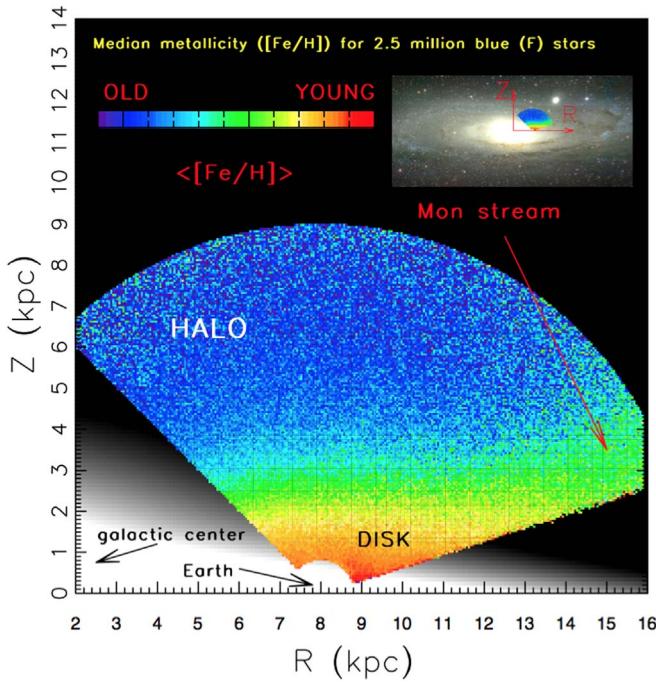
Figure 29. Median metallicity map for 2.5 million main-sequence F-type stars within 10 kpc from the Sun (adapted from Ivezić et al. 2008). The metallicity is estimated using $u - g$ and $g - r$ colors measured by SDSS. The position and size of the mapped region, relative to the rest of the Milky Way, are illustrated in the upper right corner, where the same map is scaled and overlaid on an image of the Andromeda galaxy. The gradient of the median metallicity is essentially parallel to the Z-axis, except in the Monoceros stream region, as marked. LSST will extend this map out to 100 kpc, using a sample of over 100 million main-sequence F stars.

Figure 30. Predicted spatial distribution of stars out to 150 kpc from the center of the Milky Way, from Bullock & Johnston (2005). LSST will resolve main-sequence turnoff stars out to 300 kpc, 10 times more volume than shown here, enabling a high-fidelity spatial map over the entire observed virial volume. (Note that this is significantly larger than the 100 kpc probed by *metallicity* measurements in Figure 29, which is limited by the depth of the u-band observations.) Overlaid on this prediction is the observed SDSS stellar number density map based on main-sequence stars with $0.10 < r - i < 0.15$ (Jurić et al. 2008). This map extends up to ∼20 kpc from the Sun, with the white box showing a scale of 20 kpc across and the left side aligned with the Galactic center. The revolutionary Galaxy map provided by SDSS is only complete to ∼40 kpc, or only ∼1% of the virial volume. However, the outermost reaches of the stellar halo are predicted to bear the most unique signatures of our Galaxy's formation (Johnston et al. 2008; Cooper et al. 2010). LSST will be the only survey capable of fully testing such predictions.

The sky coverage of LSST naturally targets both field stars and star clusters. To date, no systematic survey of the stellar populations of southern hemisphere clusters has been performed (e.g., such as the CFHT Open Star Cluster Survey, or the WIYN Open Star Cluster Survey in the North; Mathieu 2000; Kalirai et al. 2001). Multiband imaging of these coeval, cospatial, and isometallic systems will provide vital insights into fundamental stellar evolution. For example, the depth of LSST will enable construction of luminosity and mass functions for nearby open clusters down to the hydrogen-burning limit and beyond. Variations in the initial mass function will be studied as a function of environment (e.g., age and metallicity). The wide-field coverage will also allow us to track how the stellar populations in each cluster vary as a function of radius, from the core to beyond the tidal radius. Fainter remnant white dwarfs will be uncovered in both open and globular clusters (the nearest of which are all in the south), thereby providing a crucial link to the properties of the now evolved stars in each system.

In summary, the LSST data will revolutionize studies of the Milky Way and the entire Local Group. We list a few specific Galactic science programs that LSST will enable:

1. High-resolution studies of the distribution of stars in the outer halo in the six-dimensional space spanned by position, metallicity, and proper motions (e.g., Girard et al. 2006; Bell et al. 2008; Ivezić et al. 2008; Jurić et al. 2008; Bond et al. 2010).
2. The most complete search possible for halo streams, Galaxy satellites, and intra–Local Group stars (e.g.,

Belokurov et al. 2007b; Walsh et al. 2009; Bochanski et al. 2014).
3. Deep and highly accurate color–magnitude diagrams for over half of the known globular clusters, including tangential velocities from proper-motion measurements (Casetti-Dinescu et al. 2007; An et al. 2008).
4. Mapping the metallicity, kinematics, and spatial profile of the Sagittarius dwarf tidal stream (e.g., Ibata et al. 2001; Majewski et al. 2003; Law et al. 2005; Belokurov et al. 2014) and the Magellanic Stream (Zaritsky et al. 2004).
5. The measurement of the internal motions of Milky Way dwarf galaxies via proper motions, thereby constraining their density profiles and possibly the nature of dark matter (e.g., Walker & Peñarrubia 2011).
6. Detailed constraints on the formation and evolution of the populations within the Galactic bulge, as traced by the spatial distribution, motion, and chemistry of $\sim 10^{7-8}$ of its stars (e.g., Hill et al. 2011; Ness et al. 2014).
7. Studies of the clumpiness of the gravitational potential in the Galaxy using fragile wide-angle binaries selected with the aid of trigonometric and photometric parallaxes and common proper motion (e.g., Yoo et al. 2004; Longhitano & Binggeli 2010).
8. Detailed studies of variable star populations; 2% or better accurate multicolor light curves will be available for a sample of at least 50 million variable stars

(Sesar et al. 2007), enabling studies of cataclysmic variables, eclipsing binary systems, and rare types of variables.

9. Discovery of rare and faint high-proper-motion objects: probing the faint end of the stellar mass function (Lépine 2008; Finch et al. 2010), and searching for free-floating planet candidates (Lucas & Roche 2000; Luhman 2014).

10. Direct measurement of the faint end of the stellar luminosity function using trigonometric parallaxes (Reid et al. 2002) and a complete census of the solar neighborhood to a distance of 100 pc based on trigonometric parallax measurements for objects as faint as $M_r = 17$ (∼L5 brown dwarfs). For example, LSST will deliver 10% or better distances for a sample of about 2500 stars with $18 < M_r < 19$.

11. The separation of halo M subdwarfs from disk M dwarfs, using the $z - y$ color, which is sensitive to their rich molecular band structure (West et al. 2011; Bochanski et al. 2013).

12. Studies of white dwarfs using samples of several million objects, including the determination of the halo white dwarf luminosity function (SciBook, Chap. 6).

13. Measurements of physical properties of stars using large samples of eclipsing binary stars (Stassun et al. 2013).

14. High-resolution three-dimensional studies of interstellar dust using five-color SEDs of main-sequence stars (Planck Collaboration et al. 2011; Berry et al. 2012; Green et al. 2014).

15. A census of AGB stars in the Galaxy by searching for resolved envelopes and optical identifications of IR counterparts (e.g., from the *WISE* survey), and by using long-term variability and color selection (Ivezić 2007).

16. A complete census of faint populations in nearby star-forming regions using color and variability selection (e.g., Briceño et al. 2005).

4.5. Additional Science Projects

The experience with any large survey (e.g., SDSS, 2MASS, VISTA, *WISE*, *GALEX*, to name but a few) is that much of their most interesting science is often unrelated to the main science drivers and is often unanticipated at the time the survey is designed. LSST will enable far more diverse science than encompassed by the four themes that drive the system design. We list a few anticipated major programs:

1. Detailed studies of galaxy formation and evolution using their distribution in luminosity–color–morphology space as a function of redshift. For example, LSST will enable studies of the rest-frame UV emission, similar to those based on *GALEX* data for local galaxies, to a redshift of ∼2 for an unprecedentedly large number of galaxies. These studies project onto many axes:

   (i) the evolution of the galaxy luminosity function with redshift, as a function of morphology and color;

   (ii) the evolution of the galaxy color distribution over a wide range of rest-frame wavelengths, and as a function of luminosity and morphology;

   (iii) bulge–disk decomposition, as a function of luminosity and color, over a large redshift range;

   (iv) detailed distribution of satellite galaxies in luminosity–color–morphology space as a function of luminosity, color, and morphology of the primary galaxy;

   (v) correlations of luminosity, color, and morphology with local environment from kiloparsec to megaparsec scales, and as a function of redshift (see Figures 31 and 32);

   (vi) the properties of galaxy groups and clusters as a function of cosmic time.

2. AGN census to very faint luminosity and a large redshift limit (Ivezić et al. 2014), yielding 20 million objects from LSST data alone, and the ability to identify up to ∼100 million objects once multiwavelength data are used to aid AGN selection (see Figure 33). By reaching substantially further down the AGN luminosity function than has been possible before over a very large solid angle, LSST data will test evolutionary cosmic downsizing scenarios across the full range of cosmic environments and lead to a much clearer understanding of black hole growth during the first gigayear. For example, LSST should discover several thousand AGNs at $z \sim$ 6–7.5, representing a dramatic increase over present samples (Brandt & LSST Active Galaxies Science Collaboration 2007; see also SciBook, Chap. 10).

3. The combination of LSST, *Euclid*, and *WFIRST* data should allow discovery of at least tens of quasars at $z > 7.5$ (R. Barnett 2017, private communication).

4. LSST data will provide good constraints on AGN lifetimes, or at least the timescales over which they make distinct accretion-state transitions (MacLeod et al. 2016), due to large sample size and survey lifetime (e.g., Martini & Schneider 2003).

5. The first wide-field survey of ultra-low-surface-brightness galaxies, with photometric redshift information. The currently available samples (e.g., Greco et al. 2018) are highly incomplete, especially in the southern hemisphere (see Figure 7 in Belokurov et al. 2007b).

6. Search for strong gravitational lenses to a faint surface brightness limit (e.g., Bartelmann et al. 1998; Tyson et al. 1998; Belokurov et al. 2007a), which can be used to explore the dark matter profiles of galaxies (e.g., Treu et al. 2006).

4.5.1. Synergy with Other Projects

LSST will not operate in isolation and will greatly benefit from other precursor and coeval data at a variety of wavelengths, depths, and timescales. For example, in the visual wavelength range, most of the celestial sphere will be covered to a limit several magnitudes fainter than LSST saturation ($r \sim 16$), first by the combination of SDSS, Pan-STARRS1 (PS1), the DES (Dark Energy Survey Collaboration et al. 2016), and SkyMapper (Keller et al. 2007), and then by the *Gaia* survey. The SkyMapper survey will obtain imaging data in the southern sky to similar depths as SDSS, the PS1 survey provides multi-epoch data somewhat deeper than SDSS in the northern sky, and the DES is scanning ∼5000 deg² a magnitude deeper still in the southern sky. Despite the lack of the *u*-band data and its relatively shallow imaging, the Pan-STARRS surveys represent a valuable complement to LSST in providing northern sky coverage to a limit fainter than that of SDSS and SkyMapper. LSST and *Gaia* will be highly complementary data sets for studying the Milky Way in the multidimensional space of three-dimensional positions, proper motions, and metallicity (Ivezić et al. 2012). The *Gaia* survey
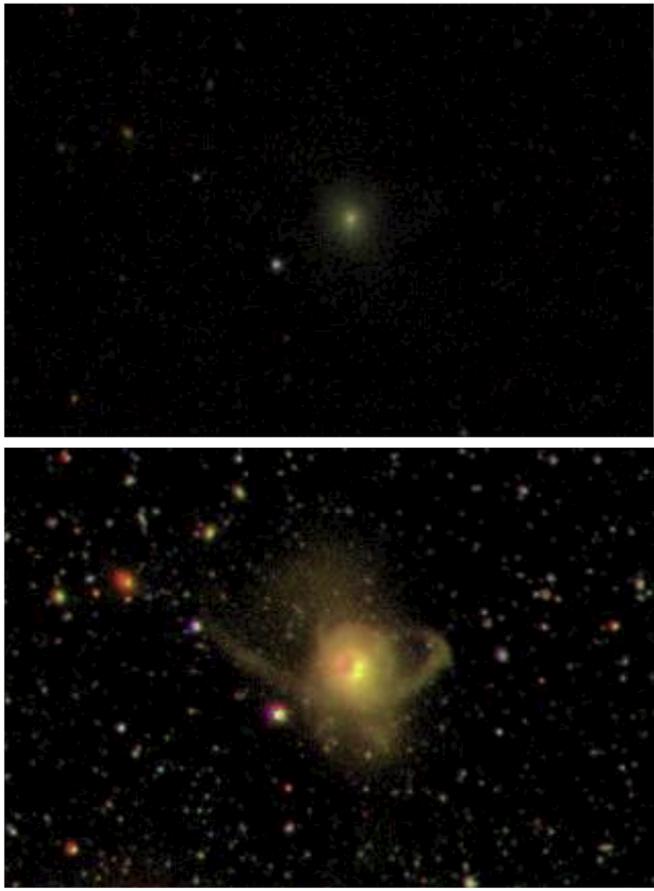
Figure 31. Comparison of an SDSS image (2×4 arcmin^2 *gri* composite) showing a typical galaxy at a redshift of $\sim$0.1 (top) with a similar *BVR* composite image of the same field obtained by the MUSYC survey (bottom; Gawiser et al. 2006). The MUSYC image is about 4 mag deeper than the SDSS image (and about 1 mag less deep than the anticipated LSST 10 yr co-added data). Note the rich surface brightness structure seen in the MUSYC image that is undetectable in the SDSS image.

will provide calibration checks at the bright end for proper motions and trigonometric parallax measurements by LSST, and LSST will extend the *Gaia* survey by 4 mag. The Zwicky Transient Facility (e.g., Laher et al. 2018), with its 600-megapixel camera and a 47 deg^2 large field of view, will generate the largest optical transient stream prior to LSST (at about 1/10 of the LSST rate) and thus provide an early insight into astrophysical surprises and technical challenges awaiting LSST. The LSST data stream will invigorate subsequent investigations by numerous other telescopes that will provide additional temporal, spectral, and spatial resolution coverage.

WFIRST and *Euclid* will carry out wide-field imaging surveys in the NIR, giving highly complementary photometry to LSST. The resulting galaxy SEDs should give rise to even better photometric redshifts, as well as tighter constraints on stellar masses and star formation histories crucial for galaxy evolution studies. The WL analyses from space and from the ground will also be highly complementary and will provide crucial cross-checks of one another. LSST also presents the opportunity to conduct simultaneous observations of *WFIRST*'s Galactic bulge survey fields, from which it will be possible to measure the parallax and hence the lens masses for most microlensing events, as well as providing valuable light-curve coverage during the large data gaps between *WFIRST* survey "seasons."

LSST will also enable multiwavelength studies of faint optical sources using gamma-ray, X-ray, IR, and radio data. For example, SDSS detected only one-third of all 20 cm FIRST sources (Becker et al. 1995) because it was too shallow by $\sim$4 mag for a complete optical identification. Similarly, deep optical data are required for identification of faint X-ray sources (Brandt & Hasinger 2005; Brandt & Vito 2017).

LSST will provide a crucial complementary capability to space experiments operating in other wavebands, such as the *NuSTAR* mission (Harrison et al. 2013), eROSITA (Merloni et al. 2012), and the *Fermi Gamma-ray Space Telescope* (e.g., Atwood et al. 2009). LIGO has now detected ultracompact binaries and black hole mergers through the gravitational wave outbursts that are emitted during the final stages of such events. LSST will aid studies of the electromagnetic signal that accompanies the gravitational wave emission, thereby providing an accurate position on the sky for the system, which is crucial for subsequent observations. LSST will also add new value to the archives for billion-dollar-class space missions such as *Chandra*, *XMM-Newton*, *Spitzer*, *Herschel*, *Euclid*, and *WFIRST*, because deep optical multicolor data will enable massive photometric studies of sources from these missions. All areas of the sky—whether by design or by serendipity—in which past, present, or future multiwavelength surveys overlap with LSST sky coverage will be further promoted by LSST investigations to become "optical plus multiwavelength Selected Areas." Last but not least, the huge samples of various astronomical source populations will yield extremely rare objects for investigations by powerful facilities such as *James Webb Space Telescope* (Gardner et al. 2006) and the next generation of 20–40 m telescopes.

In summary, the diversity of science enabled by LSST will be unparalleled, extending from the physics of gravity and the early universe to the properties of "killer" asteroids. While there are other projects that aim to address some of the same science goals, no other project matches this diversity and LSST's potential impact on society in general.

5. Community Involvement

LSST has been conceived as a public facility: the database that it will produce, and the associated object catalogs that are generated from that database, will be made available with no proprietary period to the US and Chilean scientific communities, as well as to those international partners who contribute to operations funding. As described in Section 6, data will also be made available to the general public for educational and outreach activities. The LSST data management system (Section 3.3) will provide user-friendly tools to access this database, support user-initiated queries and data exploration, and carry out scientific analyses on the data, using LSST computers either at the archive facility or at the data access centers. We expect that many, perhaps even the majority, of LSST discoveries will come from research astronomers with no formal affiliation to the project, from students, and from interested amateurs, intrigued by the accessibility to the universe that this facility uniquely provides.

The SDSS provides a good example for how the scientific community can be effective in working with large, publicly available astronomical data sets. The SDSS has published a series of large incremental DRs via a sophisticated database, roughly once per year, together with a paper describing the content of each DR, and extensive online documentation giving
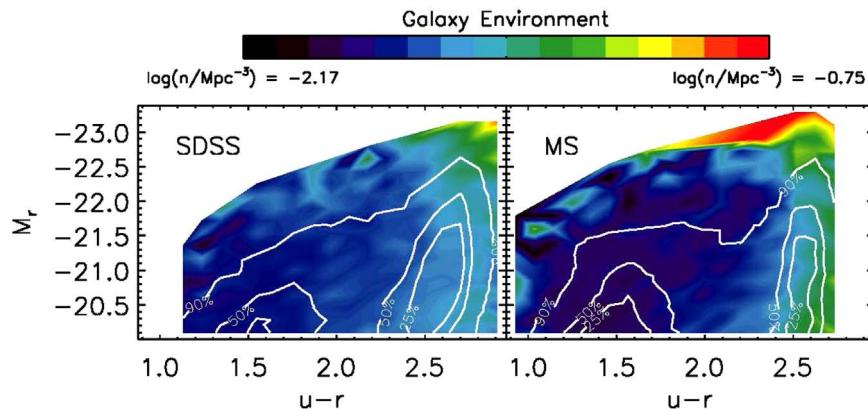
Figure 32. Comparison of the distribution of galaxies in luminosity–color–density space measured by SDSS (left) and a model based on the Millennium simulation (right). The linearly spaced contours outline the distribution of a volume-limited sample of galaxies in the plotted diagram, and the color-coded background shows the median environmental density (computed using the 10 nearest neighbors) for galaxies with the corresponding luminosity and color. Such multi-variate distributions encode rich information about formation and evolution of galaxies. Galaxies detected by SDSS are representative of the low-redshift universe (the median redshift is ∼0.1). The LSST will enable such studies as a function of redshift, to $z \sim 2$. Adapted from Cowan & Ivezić (2008).

instructions on downloading the catalogs and image data (see http://www.sdss.org). The overwhelming majority of the almost 8000 refereed papers based on SDSS data to date have been written by scientists from outside the project and include many of the most high-profile results that have come from the survey.

Nevertheless, it is clear that many of the highest-priority LSST science investigations will require organized teams of professionals working together to optimize science analyses and to assess the importance of systematic uncertainties on the derived results. To meet this need, a number of science collaborations have been established in core science areas. For example, the LSST Dark Energy Science Collaboration includes members with interests in the study of dark energy and related topics in fundamental physics with LSST data. As of the time of this contribution, there are over 800 participants in these collaborations. The science collaborations are listed on the LSST web page, together with a description of the application process for each one. All those at US and Chilean institutions, as well as named individuals from institutions in other countries that have signed Memoranda of Agreement to contribute to LSST operations costs, are eligible to apply. As described in Sections 2.6.3 and 3.3, LSST will make available substantial computational resources to the science community to carry out their analyses; the system has been sized accordingly.

As we design our observing strategies, we are actively seeking and implementing input by the LSST science community. The LSST science collaborations in particular have helped develop the LSST science case and continue to provide advice on how to optimize their science with choices in cadence, software, and data systems. A recent example is the publication of a document entitled "Science-Driven Optimization of the LSST Observing Strategy" (LSST Science Collaboration et al. 2017), a living document that quantifies the science returns in different areas for different observing cadence. The cadence will continue to be refined, with input from the science collaborations, during the commissioning, and the observing strategy will be regularly reviewed, with flexibility built in, during operations.

The Science Advisory Committee (SAC), chaired by Michael Strauss, provides a formal, and two-way, connection to the external science community served by LSST. This committee takes responsibility for policy questions facing the project and also deals with technical topics of interest to both the science community and the LSST Project. The SAC minutes and notes are available publicly. Current members on this committee are T. Anguita (Andrés Bello, Chile), R. Bean (Cornell), W. N. Brandt (Penn State), J. Kalirai (STScI), M. Kasliwal (Caltech), D. Kirkby (UC Irvine), C. Liu (Staten Island), A. Mainzer (JPL), R. Malhotra (U Arizona), N. Padilla (U. Católica de Chile), J. Simon (Carnegie), A. Slosar (Brookhaven), M. Strauss (Princeton), L. Walkowicz (Adler), and R. Wechsler (Stanford).

6. Educational and Societal Impacts

The impact and enduring societal significance of LSST will exceed its direct contributions to advances in physics and astronomy. LSST is uniquely positioned to have high impact with the interested public, planetariums and science centers, and citizen science projects, as well as middle school through university educational programs. LSST will contribute to the national goals of enhancing science literacy and increasing the global competitiveness of the US science and technology workforce. Engaging the public in LSST activities has been part of the project design from the beginning.

The mission of LSST's Education and Public Outreach (EPO) program is to provide worldwide access to a subset of LSST data through accessible and engaging online experiences so anyone can explore the universe and be part of the discovery process. To do this, LSST EPO will facilitate a pathway from entry-level exploration of astronomical imagery and information to more sophisticated interaction with LSST data using tools similar to what professional astronomers use for their work.

A dynamic, immersive web portal will enable members of the public to explore color images of the full LSST sky, examine objects in more detail, view events from the nightly alert stream, learn more about LSST science topics and discoveries, and investigate scientific questions that excite them using real LSST data in online science notebooks. The portal will also link to numerous citizen science projects using LSST data.

LSST data can become a key part of classrooms emphasizing student-centered research in middle school, high school, and
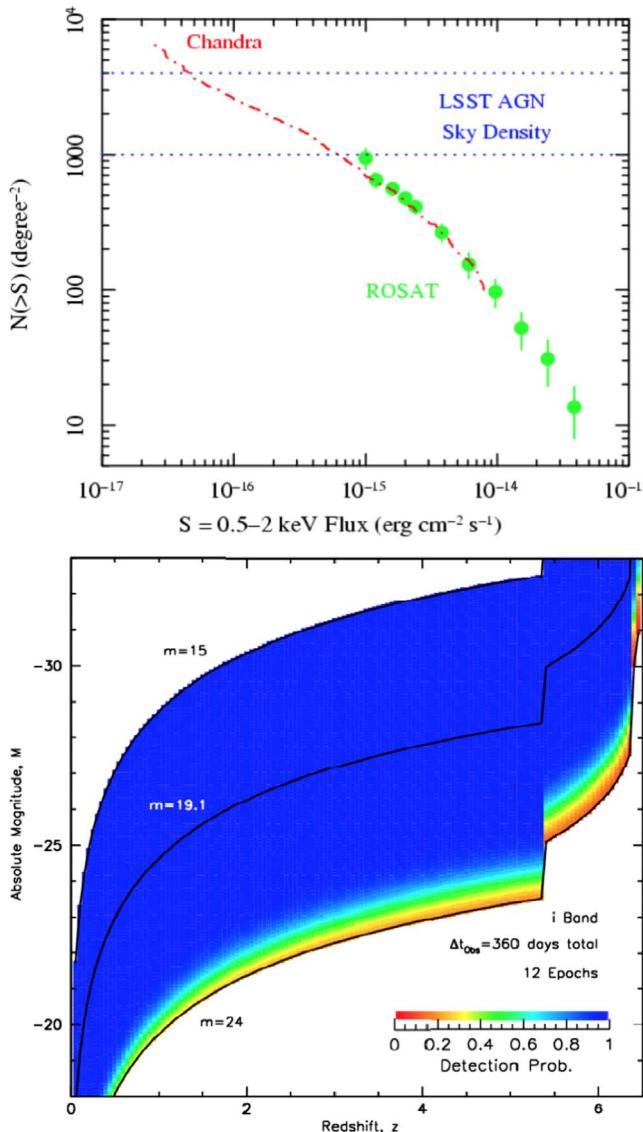
Figure 33. The LSST will deliver AGN sky densities of 1000–4000 deg^{-2} (top panel). The total LSST AGN yield, selected using colors and variability, should be well over 10 million objects, especially once multiwavelength data are also utilized. The bottom panel shows the expected distribution of these objects in the absolute magnitude vs. redshift plane, color-coded by the probability for an object to be detected as variable after 1 yr of observations. Note that quasars will be detected to their formal luminosity cutoff ($M < -23$) even at redshifts of ∼5. Adapted from Brandt & LSST Active Galaxies Science Collaboration (2007).

Team will work with the Zooniverse to develop the *Project Builder* to include tools specifically designed to utilize LSST data, allowing LSST principal investigators to create any number of projects to help them accomplish their science goals. EPO anticipates that the number of citizen science projects in the astronomy field will increase dramatically when LSST is operational, giving a whole new generation of citizen scientists the opportunity to deepen their engagement with astronomy using authentic data from LSST.

LSST EPO will produce and maintain a digital library of multimedia assets including images, video clips, and 3D models. Multimedia assets will be aligned to standards such as IMERSA Dome Master and Astronomy Visualization Metadata, when applicable, allowing full flexibility for adoption by content creators at planetariums and science centers. We will also follow the International Planetarium Society's Data2Dome standard, to maximize the number of platforms that can use our assets.

The LSST EPO program will rely on a cloud-based EPO Data Center (EDC) to handle the unique needs of the EPO audiences. These needs include, for example, a fast and smooth browsing experience on mobile devices and the need to handle inevitable spikes and lulls in visitor traffic and data transfers. As such, the EDC will follow best practices popularized by cloud computing, leveraging on-demand computing and auto-scalable architecture. Remaining agile and relevant during the full lifetime of operations by adjusting to technology trends and education priorities is an important part of the LSST EPO design process.

LSST EPO is committed to engaging with diverse audiences and is undertaking a multifaceted approach to reaching diverse individuals. LSST EPO is planning to partner with at least five organizations serving (1) women/girls, (2) individuals from traditionally underrepresented groups in STEM, and (3) individuals in low socioeconomic communities. Representatives from these organizations will be key stakeholders of the EPO program, helping to shape deliverables and a culturally responsive program evaluation. Furthermore, these relationships will allow for cocreation of EPO deliverables to help ensure materials are accessible to, of interest to, and relevant to diverse populations.

LSST EPO is breaking new ground in bringing astronomical data to the public in a timely, engaging, and easy-to-use way. It is not unreasonable to anticipate tens of millions of public users browsing the LSST sky, exploring discoveries as they are broadcast, and monitoring objects of interest. Results of EPO's ongoing evaluation will be made publicly available, allowing us to share lessons learned, insights, and program impacts with the larger science EPO community.

7. Summary and Conclusions

Until recently, most astronomical investigations have focused on small samples of cosmic sources or individual objects. Over the past few decades, however, advances in technology have made it possible to move beyond the traditional observational paradigm and to undertake large-scale sky surveys, such as SDSS, 2MASS, *GALEX*, *Gaia*, and others. This observational progress, based on a synergy of advances in telescope construction, detectors, and, above all, information technology, has had a dramatic impact on nearly all fields of astronomy, many areas of fundamental physics, and society in general. The LSST builds on the experience of these surveys

undergraduate settings. Using online science notebooks, teachers will be able to bring real LSST telescope data into their classrooms without having to download, install, and maintain software locally. Educational investigations will be designed to support key aspects of the Next-Generation Science Standards (NGSS) in the US and goals of the Explora program through CONICYT in Chile. Educators will be supported through professional development that offers training on the online notebook technology and also relevant science content. Science notebooks will also accommodate access to LSST data for lifelong learners and anyone who visits the portal.

Anyone around the world will be able to participate in a variety of citizen science projects that use LSST data. The EPO

and addresses the broad goals stated in several nationally endorsed reports by the US National Academy of Sciences. The 2010 report "New Worlds, New Horizons in Astronomy and Astrophysics" by the Committee for a Decadal Survey of Astronomy and Astrophysics ranked LSST as its top priority for large ground-based programs. The LSST will be unique: the combination of large aperture and large field of view, coupled with the needed computation power and database technology, will enable simultaneously fast and wide and deep imaging of the sky, addressing in one sky survey the broad scientific community's needs in both the time domain and deep universe.

The realization of the LSST involves extraordinary engineering and technological challenges: the fabrication of large, high-precision optics; construction of a huge, highly integrated array of sensitive, wide-band imaging sensors; and the operation of a data management facility handling tens of terabytes of data each day. The design, development, and construction effort has been underway since 2006 and will continue through the onset of full survey operations. This work involves hundreds of personnel at institutions all over the US, Chile, and the rest of the world.

In 2013 December, LSST passed the NSF Final Design Review for construction, and in 2014 May the National Science Board approved the project. The primary/tertiary mirror was cast in 2008, and the polished mirror was completed in 2015. In 2014 LSST transitioned from the design and development phase to construction, and the Associated Universities for Research in Astronomy (AURA) has had formal responsibility for the LSST project since 2011. At this writing, the project is near the peak of the construction effort and is preparing for the transition to commissioning and operations.

The construction cost of LSST is being borne by the US National Science Foundation, the Department of Energy, generous contributions from several private foundations and institutions, and the member institutions of the LSST Corporation. The LSST budget includes a significant Education and Public Outreach program (Section 6). The US Department of Energy is supporting the cost of constructing the camera. LSST has high visibility in the high-energy physics community, at both universities and government laboratories. The telescope will see first light with a commissioning camera in late 2019, and the project is scheduled to begin regular survey operations by 2022.

The LSST survey will open a movie-like window on objects that change brightness, or move, on timescales ranging from 10 s to 10 yr. The survey will have a raw data rate of about 15 TB per night (about the same as one complete SDSS per night) and will collect about 60 PB of data over its lifetime, resulting in an incredibly rich and extensive public archive that will be a treasure trove for breakthroughs in many areas of astronomy and physics. About 20 billion galaxies and a similar number of stars will be detected—for the first time in history, the number of cataloged celestial objects will exceed the number of living people! About a thousand observations of each position across half of the celestial sphere will represent the greatest movie of all time.

Alerts of transient, variable, and moving objects will be issued worldwide within 60 s of detection. An extensive public outreach program will provide a new view of the sky to curious minds of all ages worldwide. We are working with prospective foreign partners to make all of the LSST science data more broadly available worldwide. As of 2017, 34 institutions from 23 countries have signed Memoranda of Agreement to contribute significantly to the LSST operating costs, in exchange for participation in the science collaborations and data access. The software that processes the pixels and creates the LSST database is open source. LSST will be a significant milestone in the globalization of the information revolution. The vast relational database of 32 trillion observations of 40 billion objects will be mined for the unexpected and used for precision experiments in astrophysics. LSST will be in some sense an internet telescope: the ultimate network peripheral device to explore the universe, and a shared resource for all humanity.

ORCID iDs

Željko Ivezić ● https://orcid.org/0000-0001-5250-2633
J. Anthony Tyson ● https://orcid.org/0000-0002-9242-8797
Kirk T. Arndt ● https://orcid.org/0000-0002-6826-8340
Tim S. Axelrod ● https://orcid.org/0000-0002-5722-7199
Deborah J. Bard ● https://orcid.org/0000-0002-5162-5153
Amanda E. Bauer ● https://orcid.org/0000-0001-9037-6981
Andrew C. Becker ● https://orcid.org/0000-0001-6661-3043
Federica B. Bianco ● https://orcid.org/0000-0003-1953-8727
James F. Bosch ● https://orcid.org/0000-0003-2759-5764
Dominique Boutigny ● https://orcid.org/0000-0003-4887-2150
William Nielsen Brandt ● https://orcid.org/0000-0002-0167-2453
Michael E. Brown ● https://orcid.org/0000-0002-8255-0545
David L. Burke ● https://orcid.org/0000-0003-1866-1950
Jeffrey L. Carlin ● https://orcid.org/0000-0002-3936-9628
Steve Chesley ● https://orcid.org/0000-0003-3240-6497
Hsin-Fang Chiang ● https://orcid.org/0000-0002-1181-1621
Johann Cohen-Tanugi ● https://orcid.org/0000-0001-9022-4232
Rebecca Coles ● https://orcid.org/0000-0002-4774-9364
Andrew J. Connolly ● https://orcid.org/0000-0001-5576-8189
Kevin R. Covey ● https://orcid.org/0000-0001-6914-7797
Wei Cui ● https://orcid.org/0000-0002-6324-5772
Roc Cutri ● https://orcid.org/0000-0002-0077-2305
William Dawson ● https://orcid.org/0000-0003-0248-6123
Miguel de Val-Borro ● https://orcid.org/0000-0002-0455-9384
Gregory P. Dubois-Felsmann ● https://orcid.org/0000-0003-1598-6979
Frossie Economou ● https://orcid.org/0000-0002-8333-7615
Michael Eracleous ● https://orcid.org/0000-0002-3719-940X
Angelo Fausti Neto ● https://orcid.org/0000-0002-8095-305X
Henry Ferguson ● https://orcid.org/0000-0001-7113-2738
Merlin Fisher-Levine ● https://orcid.org/0000-0001-9440-8960

Emmanuel Gangler ⬤ https://orcid.org/0000-0001-6728-1423
Eric Gawiser ⬤ https://orcid.org/0000-0003-1530-8713
Marla Geha ⬤ https://orcid.org/0000-0002-7007-9725
Thomas Glanzman ⬤ https://orcid.org/0000-0001-9649-3871
Daniel A. Goldstein ⬤ https://orcid.org/0000-0003-3461-8661
Melissa L. Graham ⬤ https://orcid.org/0000-0002-9154-3136
Leanne P. Guy ⬤ https://orcid.org/0000-0003-0800-8755
Fabio Hernandez ⬤ https://orcid.org/0000-0001-7203-2552
Joshua Hoblitt ⬤ https://orcid.org/0000-0002-5292-5879
Patrick Ingraham ⬤ https://orcid.org/0000-0003-3715-8138
Tim Jenness ⬤ https://orcid.org/0000-0001-5982-167X
Anthony S. Johnson ⬤ https://orcid.org/0000-0002-5729-2716
R. Lynne Jones ⬤ https://orcid.org/0000-0001-5916-0031
Mario Jurić ⬤ https://orcid.org/0000-0003-1996-9252
Nitya J. Kallivayalil ⬤ https://orcid.org/0000-0002-3204-1742
Bryce Kalmbach ⬤ https://orcid.org/0000-0002-6825-5283
Mansi M. Kasliwal ⬤ https://orcid.org/0000-0002-5619-4938
Richard Kessler ⬤ https://orcid.org/0000-0003-3221-0419
David Kirkby ⬤ https://orcid.org/0000-0002-8828-5463
K. Simon Krughoff ⬤ https://orcid.org/0000-0002-4410-7868
Shri Kulkarni ⬤ https://orcid.org/0000-0001-5390-8563
Kian-Tat Lim ⬤ https://orcid.org/0000-0002-6338-6516
Chris J. Lintott ⬤ https://orcid.org/0000-0001-5578-359X
Robert H. Lupton ⬤ https://orcid.org/0000-0003-1666-0962
Nate B. Lust ⬤ https://orcid.org/0000-0002-4122-9384
Rachel Mandelbaum ⬤ https://orcid.org/0000-0003-2271-1527
Thomas W. Markiewicz ⬤ https://orcid.org/0000-0003-3646-8724
Joshua Meyers ⬤ https://orcid.org/0000-0002-2308-4230
Joachim Moeyens ⬤ https://orcid.org/0000-0001-5820-3925
Fred E. Moolekamp ⬤ https://orcid.org/0000-0003-0093-4279
Knut Olsen ⬤ https://orcid.org/0000-0002-7134-8296
William O'Mullane ⬤ https://orcid.org/0000-0003-4141-6195
Nathan M. Pease ⬤ https://orcid.org/0000-0002-9701-5975
J. Matt Peterson ⬤ https://orcid.org/0000-0002-6564-6246
John R. Peterson ⬤ https://orcid.org/0000-0001-5471-9609
Joel P. Plutchak ⬤ https://orcid.org/0000-0002-1501-825X
Michael A. Reuter ⬤ https://orcid.org/0000-0003-3881-8310
Stephen T. Ridgway ⬤ https://orcid.org/0000-0003-2557-7132
Aaron Roodman ⬤ https://orcid.org/0000-0001-5326-3486
Abhijit Saha ⬤ https://orcid.org/0000-0002-6839-4881
Pim Schellart ⬤ https://orcid.org/0000-0002-8324-0880
Samuel Schmidt ⬤ https://orcid.org/0000-0002-5091-0470
Michael D. Schneider ⬤ https://orcid.org/0000-0002-8505-7094
Megan E. Schwamb ⬤ https://orcid.org/0000-0003-4365-1455
Jonathan Sick ⬤ https://orcid.org/0000-0003-3001-676X
Colin T. Slater ⬤ https://orcid.org/0000-0002-0558-0521
Michael A. Strauss ⬤ https://orcid.org/0000-0002-0106-7755
Rachel A. Street ⬤ https://orcid.org/0000-0001-6279-0552
Christopher W. Stubbs ⬤ https://orcid.org/0000-0003-0347-1724
Ian S. Sullivan ⬤ https://orcid.org/0000-0001-8708-251X
John D. Swinbank ⬤ https://orcid.org/0000-0001-9445-1846
Sandrine Thomas ⬤ https://orcid.org/0000-0002-9121-3436
Adam J. Thornton ⬤ https://orcid.org/0000-0001-9342-6032
David E. Trilling ⬤ https://orcid.org/0000-0003-4580-3790

Lucianne Walkowicz ⬤ https://orcid.org/0000-0003-2918-8687
Brian Walsh ⬤ https://orcid.org/0000-0001-7426-5413
Christopher W. Walter ⬤ https://orcid.org/0000-0003-2035-2380
Beth Willman ⬤ https://orcid.org/0000-0003-2892-9906
David Wittman ⬤ https://orcid.org/0000-0002-0813-5888
W. Michael Wood-Vasey ⬤ https://orcid.org/0000-0001-7113-1233
Bo Xin ⬤ https://orcid.org/0000-0002-9171-4046
Peter Yoachim ⬤ https://orcid.org/0000-0003-2874-6464

References

Abazajian, K. N., Adelman-McCarthy, J. K., Agüeros, M. A., et al. 2009, ApJS, 182, 543
Abazajian, K. N., Adshead, P., Ahmed, Z., et al. 2016, arXiv:1610.02743
Abbott, B. P., Abbott, R., Abbott, T. D., et al. 2017a, ApJL, 848, L12
Abbott, B. P., Abbott, R., Abbott, T. D., et al. 2017b, Natur, 551, 85
A'Hearn, M. F. 2004, in Comets II, ed. M. C. Festou, H. U. Keller, & H. A. Weaver (Tucson, AZ: Univ. Arizona Press), 17
A'Hearn, M. F., Millis, R. C., Schleicher, D. O., Osip, D. J., & Birch, P. V. 1995, Icar, 118, 223
Aihara, H., Arimoto, N., Armstrong, R., et al. 2018, PASJ, 70, S4
Albrecht, A., Bernstein, G., Cahn, R., et al. 2006, arXiv:astro-ph/0609591
Alcock, C., Allsman, R. A., Alves, D. R., et al. 2000, ApJ, 542, 281
Alcock, C., Allsman, R. A., Alves, D. R., et al. 2001, ApJL, 550, L169
Amôres, E. B., & Lépine, J. R. D. 2005, AJ, 130, 659
An, D., Beers, T. C., Johnson, J. A., et al. 2013, ApJ, 763, 65
An, D., Johnson, J. A., Clem, J. L., et al. 2008, ApJS, 179, 326
Anderson, G. P., Berk, A., Acharya, P. K., et al. 1999, Proc. SPIE, 3866, 2
Anderson, S. F., Haggard, D., Homer, L., et al. 2005, AJ, 130, 2230
Angel, R., Lesser, M., Sarlot, R., & Dunham, E. 2000, in ASP Conf. Ser. 195, Imaging the Universe in Three Dimensions, ed. W. van Breugel & J. Bland-Hawthorn (San Francisco, CA: ASP), 81
Angeli, G. Z., Xin, B., Claver, C., et al. 2016, Proc. SPIE, 9911, 991118
Antilogus, P., Bailly, P., Barrillon, P., et al. 2017, JInst, 12, C03017
Antoniou, I., & Perivolaropoulos, L. 2010, JCAP, 12, 012
Araujo-Hauck, C., Sebag, J., Liang, M., et al. 2016, Proc. SPIE, 9906, 99060L
Arcavi, I., Howell, D. A., Kasen, D., et al. 2017, Natur, 551, 210
Arnett, W. D., & Meakin, C. 2011, ApJ, 741, 33
Astropy Collaboration, Robitaille, T. P., Tollerud, E. J., et al. 2013, A&A, 558, A33
Atwood, W. B., Abdo, A. A., Ackermann, M., et al. 2009, ApJ, 697, 1071
Bacci, P., Maestripieri, M., Tesi, L., et al. 2017, MPEC, 2017-U181, https://minorplanetcenter.net/mpec/K17/K17UI1.html
Barnard, M., Abrahamse, A., Albrecht, A., Bozek, B., & Yashar, M. 2008, PhRvD, 78, 043528
Bartelmann, M., Huss, A., Colberg, J. M., Jenkins, A., & Pearce, F. R. 1998, A&A, 330, 1
Batista, V., Beaulieu, J.-P., Gould, A., et al. 2014, ApJ, 780, 54
Batygin, K., & Brown, M. E. 2016, AJ, 151, 22
Bayliss, D. D. R., & Sackett, P. D. 2011, ApJ, 743, 103
Beaulieu, J.-P., Bennett, D. P., Fouqué, P., et al. 2006, Natur, 439, 437
Becker, A. C., Wittman, D. M., Boeshaar, P. C., et al. 2004, ApJ, 611, 418
Becker, R. H., White, R. L., & Helfand, D. J. 1995, ApJ, 450, 559
Becla, J., Wang, D., Monkewitz, S., et al. 2017, LSST Data Management Database Design, LSST Document LDM-135, https://ls.st/LDM-135
Bell, E. F., Zucker, D. B., Belokurov, V., et al. 2008, ApJ, 680, 295
Bellm, E. 2014, in The Third Hot-wiring the Transient Universe Workshop, ed. P. R. Wozniak et al. (Stanford, CA: Stanford Univ.), 27, http://www.slac.stanford.edu/econf/C131113.1/proceedings.html
Belokurov, V., Evans, N. W., Moiseev, A., et al. 2007a, ApJL, 671, L9
Belokurov, V., & Koposov, S. E. 2016, MNRAS, 456, 602
Belokurov, V., Koposov, S. E., Evans, N. W., et al. 2014, MNRAS, 437, 116
Belokurov, V., Zucker, D. B., Evans, N. W., et al. 2007b, ApJ, 654, 897
Benson, B. A., Ade, P. A. R., Ahmed, Z., et al. 2014, Proc. SPIE, 9153, 91531P
Bergeron, P., Wesemael, F., & Beauchamp, A. 1995, PASP, 107, 1047
Bernstein, G. M., Armstrong, R., Plazas, A. A., et al. 2017, PASP, 129, 074503
Bernstein, G. M., Trilling, D. E., Allen, R. L., et al. 2004, AJ, 128, 1364
Berry, M., Ivezić, Ž, Sesar, B., et al. 2012, ApJ, 757, 166

Bhattacharya, S., Kosowsky, A., Newman, J. A., & Zentner, A. R. 2011, PhRvD, 83, 043004
Bianco, F. B., Modjaz, M., Hicken, M., et al. 2014, ApJS, 213, 19
Blake, C., & Glazebrook, K. 2003, ApJ, 594, 665
Blandford, R. D. & LSST Strong Lensing Science Collaboration 2007, BAAS, 39, 979
Bloom, J. S., Giannios, D., Metzger, B. D., et al. 2011, Sci, 333, 203
Bloom, J. S., Starr, D. L., Butler, N. R., et al. 2008, AN, 329, 284
Bochanski, J. J., Savcheva, A., West, A. A., & Hawley, S. L. 2013, AJ, 145, 40
Bochanski, J. J., West, A. A., Hawley, S. L., & Covey, K. R. 2007, AJ, 133, 531
Bochanski, J. J., Willman, B., West, A. A., Strader, J., & Chomiuk, L. 2014, AJ, 147, 76
Bockelée-Morvan, D., & Biver, N. 2017, RSPTA, 375, 20160252
Bond, N. A., Ivezić, Ž, Sesar, B., et al. 2010, ApJ, 716, 1
Bongiorno, A., Zamorani, G., Gavignaud, I., et al. 2007, A&A, 472, 443
Bonvin, V., Courbin, F., Suyu, S. H., et al. 2017, MNRAS, 465, 4914
Bosch, J., AlSayyad, Y., Armstrong, R., et al. 2019, arXiv:1812.03248
Bosch, J., Armstrong, R., Bickerton, S., et al. 2018, PASJ, 70, S5
Bottke, W. F., Vokrouhlický, D., Broz, M., Nesvorný, D., & Morbidelli, A. 2001, Sci, 294, 1693
Brandt, N. & LSST Active Galaxies Science Collaboration 2007, BAAS, 39, 980
Brandt, W. N., & Hasinger, G. 2005, ARA&A, 43, 827
Brandt, W. N., & Vito, F. 2017, AN, 338, 241
Briceño, C., Calvet, N., Hernández, J., et al. 2005, AJ, 129, 907
Brown, M. E. 2017, AJ, 154, 65
Brown, M. E., & Batygin, K. 2016, ApJL, 824, L23
Brown, M. E., Trujillo, C., & Rabinowitz, D. 2004, ApJ, 617, 645
Bruzual, G., & Charlot, S. 2003, MNRAS, 344, 1000
Budavári, T., Connolly, A. J., Szalay, A. S., et al. 2003, ApJ, 595, 59
Bullock, J. S., & Johnston, K. V. 2005, ApJ, 635, 931
Burke, D. L., Axelrod, T., Blondin, S., et al. 2010, ApJ, 720, 811
Burke, D. L., Rykoff, E. S., Allam, S., et al. 2018, AJ, 155, 41
Burrows, A., Sudarsky, D., & Hubeny, I. 2006, ApJ, 640, 1063
Cai, R.-G., Ma, Y.-Z., Tang, B., & Tuo, Z.-L. 2013, PhRvD, 87, 123522
Campanelli, L., Cea, P., Fogli, G. L., & Marrone, A. 2011, PhRvD, 83, 103503
Carlsten, S. G., Strauss, M. A., Lupton, R. H., Meyers, J. E., & Miyazaki, S. 2018, MNRAS, 479, 1491
Carollo, D., Beers, T. C., Lee, Y. S., et al. 2007, Natur, 450, 1020
Casetti-Dinescu, D. I., Girard, T. M., Herrera, D., et al. 2007, AJ, 134, 195
Chambers, K. C., Magnier, E. A., Metcalfe, N., et al. 2016, arXiv:1612.05560
Chang, C., Jarvis, M., Jain, B., et al. 2013, MNRAS, 434, 2121
Chang, C., Jarvis, M., Jain, B., et al. 2015, MNRAS, 447, 1746
Chapline, G. F., & Frampton, P. H. 2016, JCAP, 11, 042
Chelouche, D., & Daniel, E. 2012, ApJ, 747, 62
Choi, J.-Y., Han, C., Udalski, A., et al. 2013, ApJ, 768, 129
Chou, M.-Y., Majewski, S. R., Cunha, K., et al. 2007, ApJ, 670, 346
Coe, D., & Moustakas, L. A. 2009, ApJ, 706, 45
Colin, J., Mohayaee, R., Sarkar, S., & Shafieloo, A. 2011, MNRAS, 414, 264
Connolly, A. J., Angeli, G. Z., Chandrasekharan, S., et al. 2014, Proc. SPIE, 9150, 915014
Cook, N. V., Ragozzine, D., Granvik, M., & Stephens, D. C. 2016, ApJ, 825, 51
Cooper, A. P., Cole, S., Frenk, C. S., et al. 2010, MNRAS, 406, 744
Cooray, A., Hu, W., Huterer, D., & Joffre, M. 2001, ApJL, 557, L7
Cooray, A. R. 1999, A&A, 348, 31
Coughlin, E. R., Armitage, P. J., Nixon, C., & Begelman, M. C. 2017a, MNRAS, 465, 3840
Coughlin, M., Dietrich, T., Kawaguchi, K., et al. 2017b, ApJ, 849, 12
Cowan, N. B., & Ivezić, Ž 2008, ApJL, 674, L13
Cowperthwaite, P. S., & Berger, E. 2015, ApJ, 814, 25
Cuadra, J., Armitage, P. J., Alexander, R. D., & Begelman, M. C. 2009, MNRAS, 393, 1423
Cuillandre, J.-C. J., Withington, K., Hudelot, P., et al. 2012, Proc. SPIE, 8448, 84480M
Cushing, M. C., Rayner, J. T., & Vacca, W. D. 2005, ApJ, 623, 1115
Dai, D.-C., Kinney, W. H., & Stojkovic, D. 2011, JCAP, 4, 015
Dalal, N., Doré, O., Huterer, D., & Shirokov, A. 2008, PhRvD, 77, 123514
Dalal, N., & Kochanek, C. S. 2002, ApJ, 572, 25
Dandy, C. L., Fitzsimmons, A., & Collander-Brown, S. J. 2003, Icar, 163, 363
Dark Energy Survey Collaboration, Abbott, T., Abdalla, F. B., et al. 2016, MNRAS, 460, 1270
Davis, C., Gatti, M., Vielzeuf, P., et al. 2017, MNRAS, submitted (arXiv:1710.02517)
Dawson, W. A., Wittman, D., Jee, M. J., et al. 2012, ApJL, 747, L42
De Bernardis, F., Stevens, J. R., Hasselfield, M., et al. 2016, Proc. SPIE, 9910, 991014

de Bruijne, J. H. J. 2012, Ap&SS, 341, 31
de Jong, J. T. A., Kuijken, K. H., & Héraudeau, P. 2008, A&A, 478, 755
Delgado, F., Saha, A., Chandrasekharan, S., et al. 2014, Proc. SPIE, 9150, 915015
della Valle, M., & Livio, M. 1995, ApJ, 452, 704
De Lucia, G., Springel, V., White, S. D. M., Croton, D., & Kauffmann, G. 2006, MNRAS, 366, 499
DeMeo, F. E., Binzel, R. P., Slivan, S. M., & Bus, S. J. 2009, Icar, 202, 160
Denneau, L., Jedicke, R., Grav, T., et al. 2013, PASP, 125, 357
DES Collaboration, Abbott, T. M. C., Abdalla, F. B., et al. 2018, PhRvD, 98, 043526
de Vries, W. H., Becker, R. H., & White, R. L. 2003, AJ, 126, 1217
Djorgovski, S. G., Mahabal, A., Drake, A., Graham, M., & Donalek, C. 2013, in Planets, Stars and Stellar Systems, Vol. 2: Astronomical Techniques, Software and Data, ed. T. D. Oswalt & H. E. Bond (Berlin: Springer), 223
Djorgovski, S. G., Mahabal, A. A., Drake, A. J., et al. 2012, in IAU Symp. 285, New Horizons in Time Domain Astronomy, ed. E. Griffin, R. Hanisch, & R. Seaman (Cambridge: Cambridge Univ. Press), 141
Dodelson, S., & Vallinotto, A. 2006, PhRvD, 74, 063515
Dolney, D., Jain, B., & Takada, M. 2006, MNRAS, 366, 884
Doressoundiram, A., Peixinho, N., Moullet, A., et al. 2007, AJ, 134, 2186
Drake, A. J., Beshore, E., Catelan, M., et al. 2010, arXiv:1009.3048
Drake, A. J., Djorgovski, S. G., Mahabal, A., et al. 2009, ApJ, 696, 870
Drlica-Wagner, A., Albert, A., Bechtol, K., et al. 2015, ApJL, 809, L4
Drout, M. R., Chornock, R., Soderberg, A. M., et al. 2014, ApJ, 794, 23
Duncan, M. J., Levison, H. F., & Budd, S. M. 1995, AJ, 110, 3073
Durech, J., Kaasalainen, M., Warner, B. D., et al. 2009, A&A, 493, 291
Eisenstein, D. J., Hu, W., & Tegmark, M. 1998, ApJL, 504, L57
Elliot, J. L., Kern, S. D., Clancy, K. B., et al. 2005, AJ, 129, 1117
Engelhardt, T., Jedicke, R., Vereš, P., et al. 2017, AJ, 153, 133
Evans, C. R., & Kochanek, C. S. 1989, ApJL, 346, L13
Feindt, U., Kerschhaggl, M., Kowalski, M., et al. 2013, A&A, 560, A90
Finch, C. T., Zacharias, N., & Henry, T. J. 2010, AJ, 140, 844
Fitzpatrick, M. J., Graham, M. J., Mighell, K. J., et al. 2016, Proc. SPIE, 9913, 99130L
Foley, R. J. 2012, ApJ, 748, 127
Fukugita, M., Ichikawa, T., Gunn, J. E., et al. 1996, AJ, 111, 1748
Gaia Collaboration, Brown, A. G. A., Vallenari, A., et al. 2016, A&A, 595, A2
Gaia Collaboration, Brown, A. G. A., Vallenari, A., et al. 2018, A&A, 616, A1
Gal-Yam, A., Ofek, E. O., Poznanski, D., et al. 2006, ApJ, 639, 331
Gardner, J. P., Mather, J. C., Clampin, M., et al. 2006, SSRv, 123, 485
Garnavich, P. M., Smith, R. C., Miknaitis, G., et al. 2004, BAAS, 36, 1530
Gawiser, E., van Dokkum, P. G., Herrera, D., et al. 2006, ApJS, 162, 1
Gezari, S. 2012, Euro. Phys. J. Web Conf., 39, 03001
Gezari, S., Basa, S., Martin, D. C., et al. 2008, ApJ, 676, 944
Gezari, S., Chornock, R., Rest, A., et al. 2012, Natur, 485, 217
Giannios, D., & Metzger, B. D. 2011, MNRAS, 416, 2102
Girard, T. M., Korchagin, V. I., Casetti-Dinescu, D. I., et al. 2006, AJ, 132, 1768
Gladman, B., Kavelaars, J. J., Petit, J.-M., et al. 2001, AJ, 122, 1051
Goldstein, D. A., & Nugent, P. E. 2017, ApJL, 834, L5
Goldstein, D. A., Nugent, P. E., Kasen, D. N., & Collett, T. E. 2018, ApJ, 855, 22
González, J. E., Lacey, C. G., Baugh, C. M., Frenk, C. S., & Benson, A. J. 2009, MNRAS, 397, 1254
Gordon, C., Land, K., & Slosar, A. 2007, PhRvL, 99, 081301
Gould, A. 1992, ApJ, 392, 442
Graham, M. L., Connolly, A. J., Ivezić, Ž, et al. 2018, AJ, 155, 1
Graham, M. J., Djorgovski, S. G., Drake, A. J., et al. 2014, MNRAS, 439, 703
Granvik, M., Virtanen, J., Oszkiewicz, D., & Muinonen, K. 2009, M&PS, 44, 1853
Graur, O., Bianco, F. B., Huang, S., et al. 2017, ApJ, 837, 120
Grav, T., Jedicke, R., Denneau, L., et al. 2007, BAAS, 39, 807
Grav, T., Mainzer, A. K., & Spahr, T. 2016, AJ, 151, 172
Greco, J. P., Greene, J. E., Strauss, M. A., et al. 2018, ApJ, 857, 104
Green, G. M., Schlafly, E. F., Finkbeiner, D. P., et al. 2014, ApJ, 783, 114
Grier, C. J., Trump, J. R., Shen, Y., et al. 2017, ApJ, 851, 21
Gunn, J. E., Carr, M., Rockosi, C., et al. 1998, AJ, 116, 3040
Gunn, J. E., Siegmund, W. A., Mannery, E. J., et al. 2006, AJ, 131, 2332
Habibi, F., Moniez, M., Ansari, R., & Rahvar, S. 2011, A&A, 525, A108
Han, C. 2008, ApJ, 681, 806
Hannestad, S., Tu, H., & Wong, Y. Y. 2006, JCAP, 6, 025
Hargis, J. R., Willman, B., & Peter, A. H. G. 2014, ApJL, 795, L13
Harrison, F. A., Craig, W. W., Christensen, F. E., et al. 2013, ApJ, 770, 103
Hartman, J. D., Gaudi, B. S., Holman, M. J., et al. 2009, ApJ, 695, 336
Helmi, A., Ivezić, Ž, Prada, F., et al. 2003, ApJ, 586, 195

Hicken, M., Wood-Vasey, W. M., Blondin, S., et al. 2009, ApJ, 700, 1097
Hill, V., Lecureur, A., Gómez, A., et al. 2011, A&A, 534, A80
Höflich, P., Wheeler, J. C., & Thielemann, F. K. 1998, ApJ, 495, 617
Hovatta, T., Pavlidou, V., King, O. G., et al. 2014, MNRAS, 439, 690
Howell, D. A., Sullivan, M., Conley, A., & Carlberg, R. 2007, ApJL, 667, L37
Howlett, C., Robotham, A. S. G., Lagos, C. D. P., & Kim, A. G. 2017, ApJ, 847, 128
Hsieh, H. H., & Jewitt, D. 2006, Sci, 312, 561
Hu, W., & Haiman, Z. 2003, PhRvD, 68, 063004
Hu, W., & Jain, B. 2004, PhRvD, 70, 043009
Hu, W., & Kravtsov, A. V. 2003, ApJ, 584, 702
Hu, W., & Tegmark, M. 1999, ApJL, 514, L65
Huterer, D., Shafer, D. L., & Schmidt, F. 2015, JCAP, 12, 033
Huterer, D., Takada, M., Bernstein, G., & Jain, B. 2006, MNRAS, 366, 101
Ibata, R., Irwin, M., Lewis, G. F., & Stolte, A. 2001, ApJL, 547, L133
Ishak, M., Upadhye, A., & Spergel, D. N. 2006, PhRvD, 74, 043513
Ivezić, Ž. 2007, in ASP Conf. Ser. 378, Why Galaxies Care about AGB Stars: Their Importance as Actors and Probes, ed. F. Kerschbaum, C. Charbonnel, & R. F. Wing (San Francisco, CA: ASP), 485
Ivezić, Ž., Beers, T. C., & Jurić, M. 2012, ARA&A, 50, 251
Ivezić, Ž., Brandt, W. N., Fan, X., et al. 2014, in IAU Symp. 304, Multiwavelength AGN Surveys and Studies, ed. A. M. Mickaelian & D. B. Sanders (Cambridge: Cambridge Univ. Press), 11
Ivezić, Ž., Lupton, R., Schlegel, D., et al. 2004, in ASP Conf. Ser. 327, Satellites and Tidal Streams, ed. F. Prada, D. Martinez Delgado, & T. J. Mahoney (San Francisco, CA: ASP), 104
Ivezić, Ž., Sesar, B., Jurić, M., et al. 2008, ApJ, 684, 287
Ivezić, Ž., Smith, J. A., Miknaitis, G., et al. 2007a, AJ, 134, 973
Ivezić, Ž., Tabachnik, S., Rafikov, R., et al. 2001, AJ, 122, 2749
Ivezić, Ž., & The LSST Science Collaboration 2011, LSST Science Requirements Document, LSST Document LPM-17, https://ls.st/LPM-17
Ivezić, Ž., Tyson, J. A., Jurić, M., et al. 2007b, in IAU Symp. 236, Near Earth Objects, Our Celestial Neighbors: Opportunity and Risk, ed. G. B. Valsecchi, D. Vokrouhlický, & A. Milani (Cambridge: Cambridge Univ. Press), 353
Jain, B., Spergel, D., Bean, R., et al. 2015, arXiv:1501.07897
Jain, B., Vikram, V., & Sakstein, J. 2013, ApJ, 779, 39
Jain, B., & Zhang, P. 2008, PhRvD, 78, 063503
Javanmardi, B., Porciani, C., Kroupa, P., & Pflamm-Altenburg, J. 2015, ApJ, 810, 47
Jedicke, R., Denneau, L., Grav, T., et al. 2005, BAAS, 37, 1363
Jedicke, R., Nesvorný, D., Whiteley, R., Ivezić, Ž., & Jurić, M. 2004, Natur, 429, 275
Jee, M. J., & Tyson, J. A. 2011, PASP, 123, 596
Jenness, T., Bosch, J., Owen, R., et al. 2016, Proc. SPIE, 9913, 99130G
Jenness, T., Bosch, J. F., Schellart, P., et al. 2019, arXiv:1812.08085
Jenness, T., Economou, F., Findeisen, K., et al. 2018, Proc. SPIE, 10707, 1070709
Jewitt, D. 2012, AJ, 143, 66
Jewitt, D., Stuart, J. S., & Li, J. 2011, AJ, 142, 28
Jewitt, D. C., Trujillo, C. A., & Luu, J. X. 2000, AJ, 120, 1140
Jiang, Y.-F., Green, P. J., Greene, J. E., et al. 2017, ApJ, 836, 186
Johnston, K. V., Bullock, J. S., Sharma, S., et al. 2008, ApJ, 689, 936
Jones, R. L., Chesley, S. R., Connolly, A. J., et al. 2007, BAAS, 39, 981
Jones, R. L., Gladman, B., Petit, J.-M., et al. 2006, Icar, 185, 508
Jones, R. L., Slater, C. T., Moeyens, J., et al. 2018, Icar, 303, 181
Jones, R. L., Yoachim, P., Chandrasekharan, S., et al. 2014, Proc. SPIE, 9149, 91490B
Joudaki, S., Blake, C., Johnson, A., et al. 2018, MNRAS, 474, 4894
Jurić, M., Becker, A., Shaw, R., Krughoff, K. S., & Kantor, J. 2013, Winter 2013 LSST DM Data Challenge Release Notes, DM Tech. Note DMTN-035, https://dmtn-035.lsst.io
Jurić, M., Ciardi, D., & Dubois-Felsmann, G. 2017, LSST Science Platform Vision Document, LSST Document LSE-319, https://ls.st/LSE-319
Jurić, M., Ivezić, Ž., Brooks, A., et al. 2008, ApJ, 673, 864
Jurić, M., Kantor, J., Lim, K. T., et al. 2017a, in ASP Conf. Ser. 512, Astronomical Data Analysis Software and Systems XXV, ed. N. P. F. Lorente, K. Shortridge, & R. Wayth (San Francisco, CA: ASP), 279
Jurić, M., et al. 2017b, LSST Data Products Definition Document, LSST Document LSE-163, https://ls.st/LSE-163
Kaiser, N., Aussel, H., Burke, B. E., et al. 2002, Proc. SPIE, 4836, 164
Kaiser, N., Burgett, W., Chambers, K., et al. 2010, Proc. SPIE, 7733, 77330E
Kalirai, J. S., Hansen, B. M. S., Kelson, D. D., et al. 2008, ApJ, 676, 594
Kalirai, J. S., Richer, H. B., Fahlman, G. G., et al. 2001, AJ, 122, 257
Kann, D. A., Klose, S., Zhang, B., et al. 2010, ApJ, 720, 1513

Kasliwal, M. M. 2011, PhD thesis, California Inst. Tech., http://resolver.caltech.edu/CaltechTHESIS:05162011-094345225
Kaspi, S., Brandt, W. N., Maoz, D., et al. 2007, ApJ, 659, 997
Keller, S. C., Schmidt, B. P., Bessell, M. S., et al. 2007, PASA, 24, 1
Kilbinger, M. 2015, RPPh, 78, 086901
Knezevic, Z., & Milani, A. 2005, HiA, 13, 758
Knox, L., Song, Y.-S., & Tyson, J. A. 2006, PhRvD, 74, 023512
Komatsu, E., Dunkley, J., Nolta, M. R., et al. 2009, ApJS, 180, 330
Komossa, S. 2015, JHEAp, 7, 148
Kowalski, A. F., Hawley, S. L., Holtzman, J. A., Wisniewski, J. P., & Hilton, E. J. 2010, ApJL, 714, L98
Kowalski, M., Rubin, D., Aldering, G., et al. 2008, ApJ, 686, 749
Krause, E., & Eifler, T. 2017, MNRAS, 470, 2100
Kulkarni, S. R., Ofek, E. O., Rau, A., et al. 2007, Natur, 447, 458
Kundić, T., Turner, E. L., Colley, W. N., et al. 1997, ApJ, 482, 75
Kurucz, R. L. 1979, ApJS, 40, 1
Kurucz, R. L. 1993, SYNTHE Spectrum Synthesis Programs and Line Data (Washington, DC: Smithsonian Astrophysical Observatory)
Laher, R. R., Masci, F. J., Groom, S., et al. 2018, RTSRE, 1, 329
Laureijs, R., Amiaux, J., Arduini, S., et al. 2011, arXiv:1110.3193
Law, D. R., Johnston, K. V., & Majewski, S. R. 2005, ApJ, 619, 807
Law, N. M., Kulkarni, S. R., Dekany, R. G., et al. 2009, PASP, 121, 1395
Leistedt, B., Peiris, H. V., & Roth, N. 2014, PhRvL, 113, 221301
Lenz, D. D., Newberg, J., Rosner, R., Richards, G. T., & Stoughton, C. 1998, ApJS, 119, 121
Lépine, S. 2008, AJ, 135, 2177
Levi, M., Bebek, C., Beers, T., et al. 2013, arXiv:1308.0847
Lindegren, L., Hernández, J., Bombrun, A., et al. 2018, A&A, 616, A2
Linder, E. V. 2003, PhRvD, 68, 083504
Lintott, C., Schawinski, K., Bamford, S., et al. 2011, MNRAS, 410, 166
Longhitano, M., & Binggeli, B. 2010, A&A, 509, A46
Lorimer, D. R., Bailes, M., McLaughlin, M. A., Narkevic, D. J., & Crawford, F. 2007, Sci, 318, 777
Lowry, S. C., Fitzsimmons, A., Cartwright, I. M., & Williams, I. P. 1999, A&A, 349, 649
LSST Dark Energy Science Collaboration 2012, arXiv:1211.0310
LSST Dark Energy Science Collaboration, Mandelbaum, R., Eifler, T., et al. 2018, arXiv:1809.01669
LSST Science Collaboration, Abell, P. A., Allison, J., et al. 2009, arXiv:0912.0201
LSST Science Collaboration, Marshall, P., Anguita, T., et al. 2017, LSST Science Collaborations Observing Strategy White Paper: "Science-driven Optimization of the LSST Observing Strategy," Zenodo, doi:10.5281/zenodo.842713
Lucas, P. W., & Roche, P. F. 2000, MNRAS, 314, 858
Lue, A., Scoccimarro, R., & Starkman, G. 2004, PhRvD, 69, 044005
Luhman, K. L. 2014, ApJL, 786, L18
Lupton, R., Blanton, M. R., Fekete, G., et al. 2004, PASP, 116, 133
Macaulay, E., Davis, T. M., Scovacricchi, D., et al. 2017, MNRAS, 467, 259
MacLeod, C. L., Ivezić, Ž., Kochanek, C. S., et al. 2010, ApJ, 721, 1014
MacLeod, C. L., Ross, N. P., Lawrence, A., et al. 2016, MNRAS, 457, 389
Mahabal, A. A., Djorgovski, S. G., Drake, A. J., et al. 2011, BASI, 39, 387
Majewski, S. R., Skrutskie, M. F., Weinberg, M. D., & Ostheimer, J. C. 2003, ApJ, 599, 1082
Mamajek, E. E. 2012, arXiv:1210.1616
Mana, A., Giannantonio, T., Weller, J., et al. 2013, MNRAS, 434, 684
Mandelbaum, R. 2018, ARA&A, 56, 393
Mandelbaum, R., Seljak, U., Kauffmann, G., Hirata, C. M., & Brinkmann, J. 2006, MNRAS, 368, 715
Marcus, R. A., Ragozzine, D., Murray-Clay, R. A., & Holman, M. J. 2011, ApJ, 733, 40
Martin, D. C., Fanson, J., Schiminovich, D., et al. 2005, ApJL, 619, L1
Martini, P., & Schneider, D. P. 2003, ApJL, 597, L109
Mathieu, R. D. 2000, in ASP Conf. Ser. 198, Stellar Clusters and Associations: Convection, Rotation, and Dynamos, ed. R. Pallavicini, G. Micela, & S. Sciortino (San Francisco, CA: ASP), 517
Matthews, D. J., & Newman, J. A. 2010, ApJ, 721, 456
Ménard, B., Scranton, R., Schmidt, S., et al. 2013, arXiv:1303.4722
Merloni, A., Predehl, P., Becker, W., et al. 2012, arXiv:1209.3114
Metzger, B. D. 2017, LRR, 20, 3
Metzger, B. D., & Berger, E. 2012, ApJ, 746, 48
Meyers, J. E., & Burchat, P. R. 2015, ApJ, 807, 182
Miyazaki, S., Komiyama, Y., Kawanomoto, S., et al. 2018, PASJ, 70, S1
Mo, H. J., Jing, Y. P., & White, S. D. M. 1996, MNRAS, 282, 1096
Monet, D. G., Levine, S. E., Canzian, B., et al. 2003, AJ, 125, 984
Moniez, M. 2003, A&A, 412, 105

Morokuma, T., Inada, N., Oguri, M., et al. 2007, AJ, 133, 214
Morrison, C. B., Scranton, R., Ménard, B., et al. 2012, MNRAS, 426, 2489
Munn, J. A., Monet, D. G., Levine, S. E., et al. 2004, AJ, 127, 3034
Najita, J., Willman, B., Finkbeiner, D. P., et al. 2016, arXiv:1610.01661
National Research Council 2001, Astronomy and Astrophysics in the New Millennium (Washington, DC: The National Academies Press), https://www.nap.edu/catalog/9839/
National Research Council 2003a, Connecting Quarks with the Cosmos: Eleven Science Questions for the New Century (Washington, DC: The National Academies Press), https://www.nap.edu/catalog/10079/
National Research Council 2003b, New Frontiers in the Solar System: An Integrated Exploration Strategy (Washington, DC: The National Academies Press), https://www.nap.edu/catalog/10432/
National Research Council 2010, New Worlds, New Horizons in Astronomy and Astrophysics (Washington, DC: The National Academies Press), https://www.nap.edu/catalog/12951/
Neill, J. D., & Shara, M. M. 2005, AJ, 129, 1873
Nemiroff, R. J. 2003, AJ, 125, 2740
Ness, M., Debattista, V. P., Bensby, T., et al. 2014, ApJL, 787, L19
Nesvorný, D., Jedicke, R., Whiteley, R. J., & Ivezić, Ž. 2005, Icar, 173, 132
Newburgh, L. B., Addison, G. E., Amiri, M., et al. 2014, Proc. SPIE, 9145, 91454V
Newburgh, L. B., Bandura, K., Bucher, M. A., et al. 2016, Proc. SPIE, 9906, 99065X
Newman, A. B., Treu, T., Ellis, R. S., et al. 2013, ApJ, 765, 24
Newman, J. A. 2008, ApJ, 684, 88
Newman, J. A., Abate, A., Abdalla, F. B., et al. 2015, APh, 63, 81
Nissanke, S., Kasliwal, M., & Georgieva, A. 2013, ApJ, 767, 124
Ofek, E. O., Sullivan, M., Cenko, S. B., et al. 2013, Natur, 494, 65
Oguri, M., & Kawano, Y. 2003, MNRAS, 338, L25
Oguri, M., & Marshall, P. J. 2010, MNRAS, 405, 2579
Oguri, M., & Takada, M. 2011, PhRvD, 83, 023008
Padmanabhan, N., Schlegel, D. J., Finkbeiner, D. P., et al. 2008, ApJ, 674, 1217
Parker, A., Ivezić, Ž., Jurić, M., et al. 2008, Icar, 198, 138
Patat, F. 2008, A&A, 481, 575
Percival, W. J., Reid, B. A., Eisenstein, D. J., et al. 2010, MNRAS, 401, 2148
Perlmutter, S., Aldering, G., Goldhaber, G., et al. 1999, ApJ, 517, 565
Perryman, M. A. C., de Boer, K. S., Gilmore, G., et al. 2001, A&A, 369, 339
Peterson, J. R., Jernigan, J. G., Kahn, S. M., et al. 2015, ApJS, 218, 14
Petri, A., May, M., & Haiman, Z. 2016, PhRvD, 94, 063534
Pettersen, B. R., & Hawley, S. L. 1989, A&A, 217, 187
Pier, J. R., Munn, J. A., Hindsley, R. B., et al. 2003, AJ, 125, 1559
Pinto, P. A., Smith, C. R., & Garnavich, P. M. 2004, BAAS, 36, 1530
Planck Collaboration, Ade, P. A. R., Aghanim, N., et al. 2011, A&A, 536, A23
Porciani, C., & Madau, P. 2000, ApJ, 532, 679
Pravec, P., & Harris, A. W. 2000, Icar, 148, 12
Quartin, M., Marra, V., & Amendola, L. 2014, PhRvD, 89, 023009
Rabinowitz, D. L. 1993, ApJ, 407, 412
Raddick, J., Souter, B., Lemson, G., & Taghizadeh-Popp, M. 2017, AAS Meeting, 229, 236.15
Reid, I. N., Gizis, J. E., & Hawley, S. L. 2002, AJ, 124, 2721
Reyes, R., Mandelbaum, R., Seljak, U., et al. 2010, Natur, 464, 256
Rhodes, J., Nichol, R. C., Aubourg, É., et al. 2017, ApJS, 233, 21
Richards, G. T., Fan, X., Newberg, H. J., et al. 2002, AJ, 123, 2945
Ridgway, S. T., Matheson, T., Mighell, K. J., Olsen, K. A., & Howell, S. B. 2014, ApJ, 796, 53
Riess, A. G. 2000, in ASP Conf. Ser. 201, Cosmic Flows Workshop, ed. S. Courteau & J. Willick (San Francisco, CA: ASP), 80
Riess, A. G., Filippenko, A. V., Challis, P., et al. 1998, AJ, 116, 1009
Riess, A. G., Strolger, L.-G., Casertano, S., et al. 2007, ApJ, 659, 98
Robertson, B. E., Banerji, M., Cooper, M. C., et al. 2017, arXiv:1708.01617
Rocha, M., Peter, A. H. G., Bullock, J. S., et al. 2013, MNRAS, 430, 81
Ross, N. P., Myers, A. D., Sheldon, E. S., et al. 2012, ApJS, 199, 3
Rossetto, B. M., Santiago, B. X., Girardi, L., et al. 2011, AJ, 141, 185
Rowe, B. T. P., Jarvis, M., Mandelbaum, R., et al. 2015, A&C, 10, 121
Rowe, J. F., Bryson, S. T., Marcy, G. W., et al. 2014, ApJ, 784, 45
Schlafly, E. F., Finkbeiner, D. P., Jurić, M., et al. 2012, ApJ, 756, 158
Schlegel, D. J., Finkbeiner, D. P., & Davis, M. 1998, ApJ, 500, 525
Science Working Group of the LSST & Strauss, M. A. 2004, Towards a Design Reference Mission for the Large Synoptic Survey Telescope, Document-26952, https://ls.st/Document-26952
Scolnic, D., Kessler, R., Brout, D., et al. 2018, ApJ, 852, 3
Scovacricchi, D., Nichol, R. C., Bacon, D., Sullivan, M., & Prajs, S. 2016, MNRAS, 456, 1700
Scovacricchi, D., Nichol, R. C., Macaulay, E., & Bacon, D. 2017, MNRAS, 465, 2862
Scranton, R., Connolly, A., Krughoff, S., et al. 2007, arXiv:0709.0752
Seljak, U. 2009, PhRvL, 102, 021302
Seo, H.-J., & Eisenstein, D. J. 2003, ApJ, 598, 720
Sesar, B., Ivezić, Ž., Grammer, S. H., et al. 2010, ApJ, 708, 717
Sesar, B., Ivezić, Ž., Lupton, R. H., et al. 2007, AJ, 134, 2236
Shara, M. M. 2006, AJ, 131, 2980
Sharma, S., Johnston, K. V., Majewski, S. R., Bullock, J., & Muñoz, R. R. 2011, ApJ, 728, 106
Shen, K. J., & Bildsten, L. 2009, ApJ, 692, 324
Shen, Y., Brandt, W. N., Dawson, K. S., et al. 2015, ApJS, 216, 4
Sheppard, S. S., & Trujillo, C. 2016, AJ, 152, 221
Shields, G. A., & Bonning, E. W. 2008, ApJ, 682, 758
Silsbee, K., & Tremaine, S. 2016, AJ, 152, 103
Skrutskie, M. F., Cutri, R. M., Stiening, R., et al. 2006, AJ, 131, 1163
Smartt, S. J. 2009, ARA&A, 47, 63
Smith, N. 2014, ARA&A, 52, 487
Smith, N., Li, W., Silverman, J. M., Ganeshalingam, M., & Filippenko, A. V. 2011, MNRAS, 415, 773
Solontoi, M. 2010, PhD thesis, Univ. Washington
Song, Y.-S., & Knox, L. 2004, PhRvD, 70, 063510
Spergel, D., Gehrels, N., Baltay, C., et al. 2015, arXiv:1503.03757
Staniszewski, Z., Ade, P. A. R., Aird, K. A., et al. 2009, ApJ, 701, 32
Stassun, K., Paegert, M., De Lee, N. M., & Cargile, P. 2013, AAS Meeting, 221, 116.01
Strubbe, L. E., & Quataert, E. 2009, MNRAS, 400, 2070
Stubbs, C. W., High, F. W., George, M. R., et al. 2007, PASP, 119, 1163
Stubbs, C. W., & Tonry, J. L. 2006, ApJ, 646, 1436
Suwa, Y. 2018, MNRAS, 474, 2612
Suyu, S. H., Marshall, P. J., Auger, M. W., et al. 2010, ApJ, 711, 201
Szabó, G. M., Ivezić, Ž., Jurić, M., & Lupton, R. 2007, MNRAS, 377, 1393
Takada, M. 2006, PhRvD, 74, 043505
Takada, M., Ellis, R. S., Chiba, M., et al. 2014, PASJ, 66, R1
Takada, M., & Jain, B. 2004, MNRAS, 348, 897
Takada, M., & Spergel, D. N. 2014, MNRAS, 441, 2456
Taylor, M. B. 2005, in ASP Conf. Ser. 347, Astronomical Data Analysis Software and Systems XIV, ed. P. Shopbell, M. Britton, & R. Ebert (San Francisco, CA: ASP), 29
Thompson, T. A., Prieto, J. L., Stanek, K. Z., et al. 2009, ApJ, 705, 1364
Thornton, D., Stappers, B., Bailes, M., et al. 2013, Sci, 341, 53
Tisserand, P., Le Guillou, L., Afonso, C., et al. 2007, A&A, 469, 387
Tokovinin, A. 2002, PASP, 114, 1156
Treu, T., Koopmans, L. V., Bolton, A. S., Burles, S., & Moustakas, L. A. 2006, ApJ, 640, 662
Treu, T., & Marshall, P. J. 2016, A&ARv, 24, 11
Trilling, D. E., Robinson, T., Roegge, A., et al. 2017, ApJL, 850, L38
Trujillo, C. A., Jewitt, D. C., & Luu, J. X. 2001, AJ, 122, 457
Trujillo, C. A., & Sheppard, S. S. 2014, Natur, 507, 471
Turnbull, S. J., Hudson, M. J., Feldman, H. A., et al. 2012, MNRAS, 420, 447
Tyson, J. A., Kochanski, G. P., & Dell'Antonio, I. P. 1998, ApJL, 498, L107
Tyson, J. A., Roat, C., Bosch, J., & Wittman, D. 2008, in ASP Conf. Ser. 394, Astronomical Data Analysis Software and Systems XVII, ed. R. W. Argyle, P. S. Bunclark, & J. R. Lewis (San Francisco, CA: ASP), 107
Vagg, D., O'Callaghan, D., O'Hógáin, F., et al. 2016, Proc. SPIE, 9913, 99131V
Vanden Berk, D. E., Richards, G. T., Bauer, A., et al. 2001, AJ, 122, 549
Vanden Berk, D. E., Wilhite, B. C., Kron, R. G., et al. 2004, ApJ, 601, 692
Vegetti, S., Lagattuta, D. J., McKean, J. P., et al. 2012, Natur, 481, 341
Vereš, P., & Chesley, S. R. 2017a, AJ, 154, 12
Vereš, P., & Chesley, S. R. 2017b, AJ, 154, 13
von der Linden, A., Mantz, A., Allen, S. W., et al. 2014, MNRAS, 443, 1973
Walker, M. G., & Peñarrubia, J. 2011, ApJ, 742, 20
Walsh, S. M., Willman, B., & Jerjen, H. 2009, AJ, 137, 450
Wang, D. L., Monkewitz, S. M., Lim, K.-T., & Becla, J. 2011, State of the Practice Rep. (New York: ACM), 12, https://dl.acm.org/citation.cfm?doid=2063348.2063364
Wang, L., Goldhaber, G., Aldering, G., & Perlmutter, S. 2003, ApJ, 590, 944
Weinberg, D. H., Bullock, J. S., Governato, F., Kuzio de Naray, R., & Peter, A. H. G. 2015, PNAS, 112, 12249
Weinberg, D. H., Mortonson, M. J., Eisenstein, D. J., et al. 2013, PhR, 530, 87
West, A. A., Bochanski, J. J., Bowler, B. P., et al. 2011, in ASP Conf. Ser. 448, XVI Cambridge Workshop on Cool Stars, Stellar Systems, and the Sun, ed. C. Johns-Krull, M. K. Browning, & A. A. West (San Francisco, CA: ASP), 531
Wood-Vasey, W. M., Miknaitis, G., Stubbs, C. W., et al. 2007, ApJ, 666, 694

Wright, E. L., Mainzer, A., Masiero, J., Grav, T., & Bauer, J. 2016, AJ, 152, 79
Wright, J. T., Marcy, G. W., Howard, A. W., et al. 2012, ApJ, 753, 160
Xue, Y. Q., Brandt, W. N., Luo, B., et al. 2010, ApJ, 720, 368
Yoachim, P., Coughlin, M., Angeli, G. Z., et al. 2016, Proc. SPIE, 9910, 99101A
Yoo, J., Chanamé, J., & Gould, A. 2004, ApJ, 601, 311
York, D. G., Adelman, J., Anderson, J. E., Jr., et al. 2000, AJ, 120, 1579
Yoshida, F., & Nakamura, T. 2005, AJ, 130, 2900
Zaritsky, D., Harris, J., Thompson, I. B., & Grebel, E. K. 2004, AJ, 128, 1606
Zhan, H. 2006, JCAP, 8, 008
Zhan, H., Knox, L., & Tyson, J. A. 2009, ApJ, 690, 923
Zhan, H., & Tyson, J. A. 2018, RPPh, 81, 066901
Zhang, B., Fan, Y. Z., Dyks, J., et al. 2006, ApJ, 642, 354
Zhang, B., & Mészáros, P. 2004, IJMPA, 19, 2385